Multiscale Human-based Computer Modelling and Simulation for Investigations of Arrhythmic Risk in Acute Ischemia

Hector Martinez-Navarro



Computational Cardiovascular Science group

Department of Computer Science

Linacre College - University of Oxford

This dissertation is submitted for the degree of Doctor of Philosophy

January 2020

***

A Chordi, que se fue antes de que yo empezara la tesis.

A Roberto, que ya no puede entender a qué me dedico.

A My, que no sé qué hubiera hecho sin su apoyo.

A Claudia, que creo en ella.

***

ABSTRACT

Acute myocardial ischemia is a major cause of sudden arrhythmic death. Variability in ischemic extent and location hampers the understanding of arrhythmic mechanisms and challenges risk diagnosis, stratification and treatment. Moreover, co-existent alterations in ionic channels have been proven to affect ischemia-induced arrhythmogenesis. Ischemic patients with alterations in the sodium (Na^+) current availability due to SCN5A mutations, such as Brugada syndrome, are particularly prone to develop cardiac events. Low Na^+ current availability can also be acquired with the use of pharmacological treatments. For instance, flecainide is a Na^+ channel blocker commonly used for treating atrial fibrillation, but its effects have been proven to increase mortality among ischemic patients, as observed in the CAST trials.

Although electrophysiological abnormalities caused by ischemia have been extensively investigated, the mechanisms linking such changes to high arrhythmic risk remain poorly understood. The use of in silico trials provides an alternative and high-resolution method to investigate ischemia-induced arrhythmogenesis, which overcomes ethical and technological restrictions linked to experiments. Computer simulations also allow considering variability both in ionic conditions and ischemic regions, providing a comprehensive and controlled approach for the investigations on arrhythmogenesis in acute myocardial ischemia. Thereby, I aim to investigate variability in arrhythmic risk and ECG abnormalities using a modelling and simulation framework constructed using extensive clinical and experimental data. Firstly, I present the construction and validation process of the computational framework for simulating acute myocardial ischemia. Secondly, I analyse the effects of size, transmural extent and location of myocardial ischemia on arrhythmogenesis and ECG. Then, I investigate the effects of changes in Na^+ current variability on ischemia-induced arrhythmic risk.

In this thesis, I construct a computational framework for simulating acute myocardial ischemia. The simulation pipeline is used for providing mechanistic evidence on ischemia-induced arrhythmogenesis in the context of clinical findings reported in the literature. A thorough analysis of the pro-arrhythmic mechanisms induced by ischemia is expected to provide new insights for formulating effective new anti-arrhythmic therapies.

PUBLICATIONS

- **Martinez-Navarro H**, Mincholé A, Bueno-Orovio A, Rodriguez B.
  High arrhythmic risk in antero-septal acute myocardial ischemia is explained by increased transmural reentry occurrence.
  Sci Rep **9**, 16803 (2019) doi:10.1038/s41598-019-53221-2

- **Martinez-Navarro H**, Zhou X, Mincholé A, Bueno-Orovio A, Rodriguez B. *In silico investigations of ionic variability in ischemia-induced arrhythmogenesis.* Journal article under review.

INDEXED ABSTRACTS

- **Martinez-Navarro H**, Mincholé A, Bueno-Orovio A, Rodriguez B. *High arrhythmic risk and low ST segment elevation in subendocardial compared to transmural acute ischemia.* Heart Rhythm 2017;14(5):S419-S420.

CONFERENCE PRESENTATIONS

- **Martinez-Navarro H**, Zhou X, Mincholé A, Bueno-Orovio A, Rodriguez B. *Electrophysiological and anatomical factors determine arrhythmic risk in acute myocardial ischemia and its modulation by sodium current availability* (Talk). Cardiac Physiome Conference 2019, Maastricht (Netherlands) December 2019.

- **Martinez-Navarro H**, Zhou X, Mincholé A, Bueno-Orovio A, Rodriguez B. *HPC simulations for in-silico drug trials in humans: therapeutic strategies in acute myocardial ischemia* (Talk). CompBioMed Conference 2019, London (UK) September 2019.

- **Martinez-Navarro H**, Zhou X, Mincholé A, Bueno-Orovio A, Rodriguez B. *Human in-silico investigations into therapeutic strategies in acute myocardial ischemia* (Talk delivered by Dr Xin Zhou). BioMedEng 2019, London (UK) September 2019.

- **Martinez-Navarro H**, Zhou X, Mincholé A, Bueno-Orovio A, Rodriguez B. *HPC simulations of cardiac electrophysiology as basis for in-silico drug trials* (Talk). EuroHPC Summit Week 2019, Poznań (Poland) May 2019.

- **Martinez-Navarro H**, Zhou X, Mincholé A, Bueno-Orovio A, Rodriguez B. *Human in-silico investigations into therapeutic strategies in acute myocardial ischemia* (Poster). Gordon Research Conference in Cardiac Arrhythmogenic Mechanisms, Lucca (Italy) April 2019.

- **Martinez-Navarro H**, Zhou X, Mincholé A, Bueno-Orovio A, Rodriguez B. *Human in-silico investigations into therapeutic strategies in acute myocardial ischemia* (Talk). Gordon Research Seminar in Cardiac Arrhythmogenic Mechanisms, Lucca (Italy) April 2019.

- **Martinez-Navarro H**, Mincholé A, Bueno-Orovio A, Rodriguez B. *Arrhythmogenic mechanisms in silent acute myocardial ischemia* (Talk). VPH Conference 2018, Zaragoza (Spain) September 2018.

- **Martinez-Navarro H**, Mincholé A, Bueno-Orovio A, Rodriguez B. *Arrhythmogenic mechanisms in silent acute myocardial ischemia* (Talk). Frontiers of Simulation and Experimentation for Personalized Cardiovascular Management and Treatment, VPHCaSE, University College London (United Kingdom) July 2018.

- **Martinez-Navarro H**, Mincholé A, Bueno-Orovio A, Rodriguez B. *Arrhythmogenic mechanisms in silent acute myocardial ischemia* (Talk). CompBioMed & VHeart Joint Workshop, Amsterdam (Netherlands) May 2018.

- **Martinez-Navarro H**, Mincholé A, Bueno-Orovio A, Rodriguez B. *High arrhythmic risk and low ST segment elevation in subendocardial compared to transmural acute ischemia* (Poster). Oxford Computer Science Conference 2017, Oxford (United Kingdom) June 2017.

- **Martinez-Navarro H**, Mincholé A, Bueno-Orovio A, Rodriguez B. *HPC simulations of the human heart for arrhythmia risk stratification* (Talk). European HPC Summit Week 2017 and PRACEdays17: CompBioMed sessions, Barcelona (Spain) May 2017.

- **Martinez-Navarro H**, Mincholé A, Bueno-Orovio A, Rodriguez B. *High arrhythmic risk and low ST segment elevation in subendocardial compared to transmural acute ischemia* (Poster). Heart Rhythm 2017, Chicago (Illinois, USA) May 2017.

- **Martinez-Navarro H**, Mincholé A, Bueno-Orovio A, Rodriguez B. *Computer simulations of the human ischaemic ventricles for risk stratification and ECG biomarkers evaluation* (Talk). STAFF conference 2016, Bled (Slovenia) October 2016.

MERITS AND PRIZES

- **Best talk finalist**, VPH Conference 2018, Zaragoza (Spain).
- **Travel Award** (2019), British Heart Foundation Centre of Research Excellence, Oxford (UK).
- **Research results** displayed in ARCHER Calendar 2018, Edinburgh (UK).

ACKNOWLEDGEMENTS

First and foremost, I would like to thank my supervisors. Thanks to Prof. Blanca Rodriguez for all the opportunities I have been offered since I met her and for showing me how this business works. Thanks to Dr Ana Mincholé and Dr Alfonso Bueno-Orovio, for guiding me during this painful but rewarding process, with great patience and dedication. Thanks to Xin, for being the best co-author I could imagine. I would like to give credit and thank the organisations that funded or supported my research: the Wellcome Trust, through Prof. Rodriguez's fellowship, CompBioMed and the Department of Computer Science at the University of Oxford, especially the Computational Cardiovascular Science group. Special thanks to Dr Richard Klabunde for permitting the reproduction of his figures in this thesis.

***

Muchísimas gracias a mis supervisores por el apoyo que me han ofrecido durante este duro y largo proceso de aprendizaje. Gracias a Blanca, por la fe que has tenido en mí. Ha merecido mucho la pena. Gracias a Alfonso, por tu continua dedicación y preocupación. Gracias Ana, por ser mi amiga en los momentos más duros. Gracias a Xin, por estar siempre de buen humor y dispuesta a ayudar.

Gracias a My por todo. No he sido capaz de separar esta tarea de otros aspectos de mi vida, y lo ha pagado mucha gente, pero nadie tanto como tú. Tu contribución a este trabajo y a mi vida ha sido incalculable y sin ti, dudo que estuviera escribiendo estas líneas. Durante estos años has sido lo que me ha movido hacia adelante, y no sé ni cómo me has aguantado tanto tiempo en estas condiciones. Gracias papá y mamá por traerme hasta donde estoy, por haberme escuchado cuando las cosas iban mal. Sé que he compartido más lo malo que lo bueno, y eso agota. Gracias por haber estado ahí. Gracias Aurore, por haber sido mi ejemplo a seguir y la razón por la que llegaba a mi mesa por las mañanas. Gracias Iván, por haber estado ahí siempre, incluso en las situaciones más absurdas, incluyendo aquellas en las que necesitaba llamar desesperadamente a las 3 de la mañana. También quiero dar las gracias a Ignacio García-Fernández, Miguel Lozano, Paco Gil, Esther Durá y Rafael Sebastián por impulsarme a tomar este camino hace ya unos años. Por último, no me quiero olvidar de esas personas que he conocido a lo largo de estos años y he podido contar con ellas, haciéndome la vida más fácil y feliz.

CONTENTS

ABSTRACT V

PUBLICATIONS VII

INDEXED ABSTRACTS VII

CONFERENCE PRESENTATIONS IX

MERITS AND PRIZES XI

ACKNOWLEDGEMENTS XIII

CONTENTS XV

LIST OF TABLES XIX

LIST OF FIGURES XXI

LIST OF ABBREVIATIONS AND ACRONYMS XXIII

1 INTRODUCTION 25

1.1 MOTIVATION 25

1.2 THESIS GOALS 27

1.3 OUTLINE 29

2 LITERATURE REVIEW: CARDIAC ELECTROPHYSIOLOGY AND ACUTE MYOCARDIAL ISCHEMIA 33

2.1 CARDIAC FUNCTION AND ANATOMY 33

2.2 ELECTROPHYSIOLOGY OF CARDIOMYOCYTES 38

2.3 QUANTIFYING CARDIAC CELL ELECTROPHYSIOLOGY 41

2.4 ELECTROPHYSIOLOGICAL HETEROGENEITIES WITHIN THE MYOCARDIUM 42

2.5 ACUTE MYOCARDIAL ISCHEMIA 42

2.6 CARDIAC ARRHYTHMIA MECHANISMS 45

2.7 ELECTROCARDIOGRAM 46

2.8 ISCHEMIA-INDUCED ABNORMALITIES IN THE ECG 49

2.9 SAFETY AND EFFICACY OF ANTI-ARRHYTHMIC DRUGS 51

CONCLUSION 52

3 COMPUTATIONAL METHODS FOR MODELLING AND SIMULATION OF CARDIAC ELECTROPHYSIOLOGY 55

3.1 MODELLING THE ACTION POTENTIAL AND CELL ELECTROPHYSIOLOGY 55

3.2 THE HODGKIN-HUXLEY MODEL 56

3.3 VENTRICULAR ACTION POTENTIAL MODELS DURING THE LAST DECADES 58

3.4 THE O'HARA-RUDY MODEL 59

3.5 MODIFICATIONS ON THE O'HARA-RUDY FOR SIMULATING ISCHEMIA 61

3.6 MODELLING CARDIAC TISSUE COUPLING AND POTENTIAL PROPAGATION 61

3.6.1 Bidomain equations 61

3.6.2 Finite element method (FEM) 63

3.6.3 Simulation software: Chaste 64

3.6.4 Convergence analysis *66*
3.7 SIMULATING DRUG-INDUCED EFFECTS ON CARDIAC ELECTROPHYSIOLOGY 68
CONCLUSION 69

4 SIMULATION FRAMEWORK FOR HUMAN ACUTE MYOCARDIAL ISCHEMIA 71

4.1 THE HUMAN TORSO AND VENTRICULAR MODEL 71
4.2 MODELLING OF ELECTROPHYSIOLOGICAL HETEROGENEITIES 72
4.3 MODELLING ISCHEMIA-INDUCED ELECTROPHYSIOLOGICAL CHANGES 73
4.4 STIMULATION PROTOCOL 76
4.5 QUANTIFICATION OF ARRHYTHMOGENESIS 77
4.6 ECG SIMULATION 77
4.7 STRUCTURE OF THE SIMULATION FRAMEWORK 77
4.7.1 Software application for efficient execution of high-performance computing simulations of human cardiac electrophysiology *78*
4.7.2 Setup and execution of simulations *79*
4.7.3 Data analysis *79*
4.8 VALIDATION OF THE SIMULATION FRAMEWORK 80
4.8.1 Cellular electrophysiology *80*
4.8.2 Myocardial propagation *81*
4.8.3 Quantification of ECG biomarkers *82*
4.8.4 ECG in control conditions *83*
4.8.5 ECG in ischemic conditions *84*

5 HIGH ARRHYTHMIC RISK IN ANTERO-SEPTAL ACUTE MYOCARDIAL ISCHEMIA IS EXPLAINED BY INCREASED TRANSMURAL REENTRY OCCURRENCE 87

5.1 INTRODUCTION 87
5.2 METHODS 89
5.3 RESULTS 90
5.3.1 Impact of location, transmural extent and size of acute regional ischemia on ECG biomarkers *90*
5.3.2 Differences in wavelength for reentry explain the effect of ischemic region size and myocardial conduction velocity on arrhythmic risk *92*
5.3.3 Arrhythmia vulnerability in subendorcardial LAD occlusion is explained by septo-apical transmural microreentrant pathways *94*
5.4 DISCUSSION 98
5.5 LIMITATIONS OF THE STUDY 100
5.6 CONCLUSION 101

6 PRO-ARRHYTHMIC MECHANISMS INDUCED BY ACUTE MYOCARDIAL ISCHEMIA CO-EXISTING WITH SODIUM BLOCK ANALYSED THROUGH IN SILICO EXPERIMENTS 103

6.1 INTRODUCTION 103

6.2 METHODS 104
6.2.1 Calculation of electrophysiological biomarkers in 1D fibres under baseline and ischemic conditions 104
6.2.2 Alterations in Na^+ current availability for simulating channelopathies and drug-induced Na^+ channel block 105
6.2.3 Simulation of Na^+ current block using the computational framework 106
6.3 RESULTS 108
6.3.1 Na^+ current block reduces moderately myocardial conduction velocity but increases significantly refractoriness dispersion 108
6.3.2 The asymmetric biventricular anatomy explains differences in ischemia-induced reentrant mechanisms 109
6.3.3 Reduced Na^+ current availability promotes reentry inducibility particularly following ectopy in RV and septum/base 111
6.3.4 Reentry induced by ectopic stimuli at the ventricular base are insensitive to moderate reductions in Na^+ current availability 117
6.4 DISCUSSION 118
6.5 LIMITATIONS 120
6.6 CONCLUSION 121

7 CONCLUSIONS AND FUTURE WORK 123

7.1 SUMMARY 123
7.2 MAIN FINDINGS 127
7.3 FUTURE WORK 129
7.3.1 Ectopic stimuli 129
7.3.2 Purkinje system 129
7.3.3 Electromechanical model of the ventricles 130
7.4 CONCLUSIONS 130

8 REFERENCES 133

9 ANNEX: SOFTWARE CONTRIBUTIONS 151

9.1 SOFTWARE APPLICATION FOR MULTISCALE SIMULATIONS OF REGIONAL ACUTE MYOCARDIAL ISCHEMIA IN HUMAN 151
9.2 SUBMISSIONS OF JOBS IN ARCHER 155
9.3 POST-PROCESSING OF SIMULATION RESULTS 158
9.4 ELECTROCARDIOGRAM SIMULATION 163

LIST OF TABLES

TABLE 2.1. SUITABLE LEADS FOR DETECTING ISCHEMIA IN DIFFERENT REGIONS OF THE MYOCARDIUM AND THE CORONARY ARTERY MOST LIKELY CAUSING ISCHEMIA. 49
TABLE 3.1. I_{NA} STEADY STATE INACTIVATION AND RECOVERY GATES (*H* AND *J*) IN THE ORIGINAL ORD. 62
TABLE 3.2. I_{NA} STEADY STATE INACTIVATION AND RECOVERY GATES (*H* AND *J*) IN THE MODIFIED ORD VERSION. 62
TABLE 4.1. CHANGES IN APD, RESTING POTENTIAL AND ERP AFTER 10 MIN OF ACUTE MYOCARDIAL ISCHEMIA USING THE MODIFIED ORD MODEL VERSION AS DESCRIBED BY (DUTTA ET AL., 2017). 81
TABLE 4.2. CONDUCTION VELOCITIES MEASURED IN SIMULATIONS OF ELECTRICAL PROPAGATION IN MYOCARDIAL TISSUE FIBRES ALONG THE LONGITUDINAL AND TRANSVERSAL AXIS, UNDER ISCHEMIC AND HEALTHY CONDITIONS AND WITH NORMAL AND SLOW MYOCARDIAL PROPAGATION. 82
TABLE 6.1. IONIC CHANNEL BLOCK VALUES COMPUTED FOR SELECTED CHANNEL BLOCKERS AT DIFFERENT DOSES: 1, 3 AND 5 TIMES THE MAXIMUM EFFECTIVE FREE THERAPEUTIC PLASMA CONCENTRATION EFTPCMAX. 105
TABLE 6.2. SCENARIOS DESIGNED FOR EVALUATION OF THE ELECTROPHYSIOLOGICAL CONSEQUENCES OF IONIC ALTERATIONS IN ACUTE MYOCARDIAL ISCHEMIA CAUSED BY PHARMACOLOGICAL AND GENE THERAPY. 106
TABLE 6.3. MEASUREMENT OF ELECTROPHYSIOLOGICAL BIOMARKERS UNDER VARYING Na^+ CURRENT CONDITIONS, MEASURED IN 1D FIBRES BASED ON THE O'HARA-RUDY MODEL. 108

LIST OF FIGURES

FIGURE 2.1. LONGITUDINAL CROSS-SECTION OF THE HEART SHOWING THE MAIN BLOOD VESSELS AND CHAMBERS 34
FIGURE 2.2. SCHEMATIC REPRESENTATION OF THE FAST CONDUCTION SYSTEM IN THE HEART. 35
FIGURE 2.3. STRUCTURE OF THE MUSCLE FIBRES IN THE MYOCARDIAL TISSUE. 36
FIGURE 2.4. SCHEMATIC VIEW OF THE CORONARY ARTERIES AND THE AREAS PERFUSED BY THEM. 37
FIGURE 2.5. SCHEMATIC ILLUSTRATION OF THE CORONARY ARTERY CIRCULATION WITH AND WITHOUT ARTERIAL ANASTOMOSIS BETWEEN THE RIGHT CORONARY ARTERY AND THE OCCLUDED LAD ARTERY. 37
FIGURE 2.6. AP PHASES IN VENTRICULAR CARDIOMYOCYTES. 38
FIGURE 2.7. RESTITUTION CURVES CONSTRUCTED ON THE HUMAN ENDOCARDIUM AT VARYING DIASTOLIC INTERVALS. 40
FIGURE 2.8. AP DIFFERENCES IN OVINE CARDIOMYOCYTES FROM THE EPICARDIUM AND ENDOCARDIUM (BLACK). 42
FIGURE 2.9. SCHEMATIC OF FIGURE-OF-EIGHT REENTRANT PATTERN TRIGGERED BY ISCHEMIA. 46
FIGURE 2.10. SCHEMATIC DIAGRAM OF NORMAL SINUS RHYTHM FOR A HUMAN HEART AS SEEN ON THE ECG. 47
FIGURE 2.11. ELECTRODE PLACEMENT IN THE 12-LEAD ECG. 48
FIGURE 2.12. MECHANISM UNDERLYING ST SEGMENT DEVIATION INDUCED BY SUBENDOCARDIAL AND TRANSMURAL ISCHEMIA. 50
FIGURE 3.1. SCHEMATIC DIAGRAM OF THE ORD MODEL. 60
FIGURE 3.2. DEPENDENCIES OF THE CARDIAC ELECTROPHYSIOLOGY SIMULATION MODULE WITH OTHER CODE COMPONENTS. 65
FIGURE 3.3. CHASTE'S SCALABILITY ANALYSIS FOR A BIDOMAIN SIMULATION OF CARDIAC ELECTROPHYSIOLOGY. 66
FIGURE 3.4. CONVERGENCE ANALYSIS FOR DIFFERENT TIME AND SPACE DISCRETISATIONS USING CVODE IN CHASTE. 67
FIGURE 4.1. TORSO/BIVENTRICULAR MODEL USED FOR CONSTRUCTING THE SIMULATION FRAMEWORK. 72
FIGURE 4.2. SIMULATED APS IN EPICARDIAL, MID-MYOCARDIAL AND ENDOCARDIAL CELLS USING THE ORD MODEL. 73
FIGURE 4.3. MODELLING VARIABILITY IN THE ISCHEMIC REGION. 74
FIGURE 4.4. MODELLING OF THE ISCHEMIC REGION. 75
FIGURE 4.5. QUANTIFICATION OF ARRHYTHMOGENESIS. 76
FIGURE 4.6. MODELLING OF ECTOPIC STIMULI IN THE ISCHEMIC BZ. 77
FIGURE 4.7. VISUALISATION OF THE COMBINED HEART-TORSO MESH. 78
FIGURE 4.8. COMPARISON OF SIMULATED ECG UNDER CONTROL HEALTHY CONDITIONS, WITH THE 12-LEAD ECG RECORDING FROM SUBJECT 173 IN THE PTB DATABASE. 83
FIGURE 4.9. A: COMPARISON BETWEEN SIMULATED ECG SIGNAL IN THE PRECORDIAL LEADS IN TRANSMURAL ISCHEMIA AND CLINICAL RECORDING FROM A STAFF III DATABASE PATIENT UNDERGOING A LAD CORONARY BALLOON OCCLUSION. B: COMPARISON BETWEEN SIMULATED ECG

SIGNAL IN THE PRECORDIAL LEADS IN SUBENDOCARDIAL ISCHEMIA AND CLINICAL ECG FROM THE LONG-TERM ST DATABASE DURING TRANSIENT ISCHEMIA EPISODE. 85
FIGURE 4.10. ANALYSIS OF THE MECHANISMS PRODUCING THE ST SEGMENT DEVIATION 86
FIGURE 5.1. ECG ALTERATIONS CAUSED BY ACUTELY-ISCHEMIC REGIONS. 91
FIGURE 5.2. ISCHEMIA-INDUCED ALTERATIONS IN ECG BIOMARKERS VERSUS PERCENTAGE OF ISCHEMIC MYOCARDIUM. 92
FIGURE 5.3. VULNERABILITY WINDOWS FOR REENTRY IN ACUTE REGIONAL ISCHEMIA. 93
FIGURE 5.4. EFFECTS OF SLOW MYOCARDIAL PROPAGATION AND ISCHEMIC REGION SIZE ON MACRO-REENTRY FORMATION. 94
FIGURE 5.5. VULNERABILITY WINDOWS FOR REENTRY FOR THE MOST PRO-ARRHYTHMIC CONDITIONS, IN LAD VERSUS LCX OCCLUSION AND TRANSMURAL VERSUS SUBENDOCARDIAL ISCHEMIC REGION FOR 6 EQUALLY-SPACED PREMATURE STIMULUS LOCATIONS AROUND THE ISCHEMIC REGION. 95
FIGURE 5.6. TWO DISTINCT MECHANISMS OF REENTRY IN ACUTE REGIONAL ISCHEMIA. 97
FIGURE 5.7. REENTRANT MECHANISMS IN LCX OCCLUSION. 98
FIGURE 6.1. COMPARISON OF SIMULATED ECG UNDER Na^+ BLOCK CONDITIONS WITH ECG RECORDINGS FROM HEALTHY PATIENTS ADMINISTRATED OF AJMALINE (Na^+ BLOCKER). 107
FIGURE 6.2. VULNERABILITY WINDOWS FOR REENTRY FOR DIFFERENT LOCATIONS OF ECTOPIC STIMULI IN ACUTE REGIONAL TRANSMURAL ISCHEMIA FOR LAD OCCLUSION IN BASELINE CONDITIONS. 109
FIGURE 6.3. MAIN REENTRANT MECHANISMS OBSERVED IN THE ISCHEMIA-INDUCED REENTRY SIMULATIONS. 110
FIGURE 6.4. VULNERABILITY WINDOWS FOR REENTRY FOR DIFFERENT LOCATIONS OF ECTOPIC STIMULI IN ACUTE REGIONAL TRANSMURAL ISCHEMIA FOR LAD OCCLUSION UNDER 50% Na^+ CHANNEL BLOCK CONDITIONS. 112
FIGURE 6.5. COMPARISON OF ACTIVATION SEQUENCES PRODUCED BY ECTOPICS SET IN LV AND RV UNDER 50% Na^+ BLOCK CONDITIONS. 114
FIGURE 6.6. MEASUREMENT OF MYOCARDIAL WIDTH AT THE TIME OF THE REENTRY OBSERVED IN FIGURE 6.5 115
FIGURE 6.7. VULNERABILITY WINDOWS FOR REENTRY (GREY BOXES) FOR DIFFERENT LOCATIONS OF ECTOPIC STIMULUS IN ACUTE REGIONAL TRANSMURAL ISCHEMIA FOR LAD OCCLUSION WITH DIVERSE Na^+ CHANNEL ALTERATIONS. 117

LIST OF ABBREVIATIONS AND ACRONYMS

AP	Action potential
BZ	Border zone
CAD	Coronary artery disease
CAST	Cardiac Arrhythmia Suppression Trial
DAD	Delayed afterdepolarisation
EAD	Early afterdepolarisation
ECG	Electrocardiogram
ERP	Effective refractory period
ICZ	Ischemic core zone
LAD	Left anterior descending artery
LCX	Left circumflex artery
LV	Left ventricle
Na^+	Sodium
ODE	Ordinary differential equation
ORd model	O'Hara-Rudy model
S1	Simulated sinus rhythm
S2	Ectopic stimulus
PDE	Partial differential equation
PRR	Post-repolarisation refractoriness
RV	Right ventricle
SCD	Sudden cardiac death
SCN5A	Sodium voltage-gated channel alpha subunit 5
VF	Ventricular fibrillation
VT	Ventricular tachycardia
VW	Vulnerability window

vW	Wilson’s central terminal
ΔERP	Refractoriness dispersion

1 INTRODUCTION

1.1 Motivation

Cardiovascular disease is a major cause of death in the world, accounting for 37% of mortality in the European Union (European Heart Network, 2017). In the United Kingdom alone, 460 people die of cardiovascular diseases every day, of which 180 patients would lose their life to coronary artery disease (CAD) (British Heart Foundation, 2019a).

The total or partial obstruction of a coronary artery prevents the myocardium from receiving enough blood irrigation. CAD is often produced by atherosclerosis which is promoted by various factors, such as smoking, cholesterol, hypertension or diabetes. When blood irrigation in the myocardial tissue is interrupted, the affected tissue suffers from ischemia in a few minutes. Ischemic tissue yields slower conduction and longer refractoriness than healthy myocardial regions. The resulting electrophysiological heterogeneities between healthy and ischemic tissue in the myocardium establish a pro-arrhythmic substrate by creating electrical propagation abnormalities. Thus, the occlusion of a coronary artery could result in life-threatening ventricular arrhythmias, potentially leading to sudden cardiac death (SCD).

The symptoms associated with ischemic episodes vary broadly among patients due to the variability in ischemic conditions, including ischemia-induced abnormalities in the electrocardiogram (ECG). For instance, women with acute coronary syndromes or myocardial ischemia frequently undergo treatment later than males (Regitz-Zagrosek,

2011), due to the divergence in symptoms between sexes and, most importantly, raising the need of investigating its significance in patients' prognosis (Park and Richard Conti, 2016). The analysis of the ECG is extensively used for diagnosis of acute myocardial infarction or ischemia (Herring and Paterson, 2006), but the occlusion of a coronary artery can also lead to negligible or even no changes at all in the ECG (Ahmed et al., 2007; Kawano et al., 2016).

Patient treatment is also a challenging aspect in myocardial ischemia: anti-arrhythmic drugs are recommended as non-invasive options for patients suffering from certain cardiovascular diseases. However, some of these drugs can interplay with the ischemic substrate, potentially inducing lethal side-effects. For instance, flecainide –a sodium (Na^+) blocker– is extensively prescribed for atrial fibrillation patients. In an attempt to extend its clinical use, the CAST trials (Cardiac Arrhythmia Suppression Trial II Investigators, 1992; Echt et al., 1991) was designed to prove the hypothesis that flecainide could be an effective therapy against the formation of ventricular ectopies. The trial had to be prematurely interrupted due to excessive mortality among participating patients with a myocardial infarction history. Cardiac events and death were more likely among patients using flecainide, especially in those cases with recurrent ischemia episodes produced by a reduced and uninterrupted coronary blood irrigation (Anderson et al., 1994; Greenberg et al., 1995).

The coronary artery occluded, the severity of the occlusion and its location, and the existence of comorbidities and treatments in the patient affect ischemia-induced arrhythmic risk, but their role has not been elucidated. Ethical and technical limitations are significant obstacles in the study of myocardial ischemia. Most patients experiencing ventricular arrhythmias during phase 1A acute myocardial ischemia suffer an out-of-the-hospital cardiac arrest, which complicates the study of the underlying electrophysiological mechanisms in human subjects and causes very high mortality rates (Kalarus et al., 2019). In these cases, a prompt recognition of symptoms and urgent reperfusion are required for the patients' survival. Additionally, several methodological challenges remain unsolved: experimentally, the spatiotemporal dynamics of acute regional ischemia continuously change the substrate, whereas computationally the investigations are very costly and require high-performance computing.

Computer simulations are able to reproduce the action potential (AP) of a cardiomyocyte based on formulations of the ionic currents recorded experimentally (O'Hara et al., 2011; ten Tusscher et al., 2004). Furthermore, the AP model can be incorporated into spatially extended frameworks able to simulate whole organ electrophysiology by coupling thousands or millions of instances of the AP model (Cardone-Noott et al., 2016; Trayanova, 2011). These multiscale computer simulations of cardiac electrophysiology have been able to reproduce existing knowledge on ischemia-induced electrophysiological alterations and the establishment of reentrant dynamics around ischemic regions (Dutta et al., 2016; Ferrero et al., 2003). Electrophysiological properties of the myocardial tissue in phase 1A ischemia (first 10-15 minutes post-occlusion) are different from those observed in other stages post-occlusion (Carmeliet, 1999; Janse and Wit, 1989; Penny and Sheridan, 1983). Phase 1B ischemia (10-30 min after occlusion) and infarction have been the focus of previous computational studies (Arevalo et al., 2016; Pollard et al., 2002). This thesis aims to provide mechanistic evidence on the high arrhythmic risk associated with phase 1A ischemia, whilst explaining the variability observed among ischemic patients.

1.2 Thesis goals

The aim of this thesis is to provide mechanistic evidence of the differences in arrhythmic risk produced by varying size, location and transmural extent of the ischemic region, and also changes in Na^+ current availability. For this, multiple *in silico* experiments were performed using a computational framework for simulating human acute myocardial ischemia, which has been constructed and evaluated with extensive clinical and experimental data at the cellular, tissue and organ levels. The research in this thesis could be divided into the following goals:

1. Development of a simulation pipeline for electrophysiological modelling of acute regional myocardial ischemia in human ventricles on high-performance computing.
2. Assessment of ischemia-induced arrhythmic risk considering variability in ischemic conditions, such as transmural extent, location and size of the ischemic region.

3. Evaluation of the effects of Na^+ channel availability on ischemia-induced arrhythmogenic mechanisms.

For the first aim, a human ventricular biophysically-detailed model with acute regional ischemia was constructed and evaluated using experimental and clinical data. One of the purposes of the investigations conducted is to quantify arrhythmic risk in multiple scenarios. For this, each of the ischemia scenarios requires many simulations under varying conditions. The level of detail in the model and the number of simulations expected to be run increases drastically the computational complexity of the experiments in this thesis, demanding the use of high-performance computing resources. Based on this need, the simulation platform would benefit from implementing a semi-automatic computational pipeline, thus reducing the misuse of resources and the occurrence of errors.

The second aim of this thesis comprehends a simulation study on human acute myocardial ischemia using the above-mentioned computational framework. The aim of this study is to unravel the mechanisms behind the variability in arrhythmic risk and ECG abnormalities among ischemic patients. For this purpose, a set of 16 scenarios representing variability in the ischemic region was developed, which includes two sizes of ischemic region, transmural and subendocardial ischemia, two locations (anterior myocardial and free LV walls) and normal versus slow propagation conditions in the remote myocardium. Besides providing a quantification for inducibility of arrhythmia, differences in arrhythmogenic mechanisms are investigated based on the characteristics of the ischemic region. For clinical translation, the ECG is simulated with the purpose of linking pro-arrhythmic mechanisms with electrocardiographic features.

The third aim of this thesis is to investigate how ionic alterations modulate ischemia-induced arrhythmogenesis in human. For this, a series of *in silico* drug trials was conducted simulating drug effects in the acute myocardial ischemia human model, allowing to analyse how Na^+ channel availability affects ischemia-induced arrhythmic risk. Limited Na^+ channel availability is caused by the sodium voltage-gated channel alpha subunit 5 (SCN5A) mutations or the use of Na^+ blockers, which are commonly used to treat certain cardiac arrhythmias, such as atrial fibrillation. For instance, the use of flecanide is associated with high mortality among ischemic patients, but the

underlying mechanisms remain not completely understood. This thesis provides mechanistic evidence of the role of Na^+ channel availability in the formation of ventricular arrhythmias, which can lead to a better understanding of arrhythmic risk in patients with Na^+ related channelopathies, such as Brugada syndrome.

1.3 Outline

I provide a short outline of this document based on a short overview for each chapter.

Chapter 2 introduces the physiological background relevant to the research presented in this thesis. It provides a brief description of cardiac anatomy and function. The electrophysiology of cardiomyocytes is presented, covering the AP, its phases and the underlying ionic mechanisms. A brief description of the most popular markers used for quantification of cardiac electrophysiology is also given. I present an overview of electrophysiological heterogeneities naturally found in human myocardium under control conditions, but also the alterations induced by ischemia, and their role in arrhythmogenesis. I illustrate the importance of the ECG in diagnosis, with a special interest in the ECG biomarkers linked to myocardial ischemia. The potential cardiotoxic effects of certain pharmacological compounds are presented in the last section of this chapter.

Chapter 3 presents relevant tools and technologies in cardiac modelling and simulation. A brief history of the existing cardiac models is presented, including the Hodgkin-Huxley model to describe electrical activity in the squid giant axon, as it represents a precursor for posteriorly built cardiac cell models. I describe the O'Hara-Rudy model of the human ventricular cardiomyocyte, the most up-to-date and extensively validated human cardiac AP model, and the choice for this thesis. The solver used for simulating cardiac electrophysiology is described, including diverse intrinsic computational and numerical aspects.

Chapter 4 provides a detailed description of the computational pipeline for simulating human acute regional myocardial ischemia developed for this research. Information is provided for every relevant aspect of the framework, including the cardiac model and implementation details of crucial features of the human cardiac function. The chapter also covers the proposed infrastructure for semiautomatic execution and analysis of *in silico* human whole-organ trials, from the scripts used for creating the jobs used for the

simulations to the post-processing of the results. To conclude, I present the evaluation of the modelling and simulation framework at tissue and organ levels including control and ischemic conditions, and varying Na^+ channel availability.

Chapter 5 consists of a study that investigates how variability in acute myocardial ischemia affects ischemia-induced pro-arrhythmic risk and ECG abnormalities. Using the described computational framework, I created a set of acute myocardial ischemia scenarios with diverse features for representing variability in the ischemic region. The cases simulated included different sizes and transmural extents of the ischemic region. Two different locations were represented: ischemia in the anterior myocardial wall and in the left ventricular free wall, modelling occlusions in the left anterior descending and left circumflex arteries, respectively. Additionally, all scenarios were simulated under normal and reduced coupling conditions in the distant myocardium. The latter is likely in patients suffering from additional cardiac comorbidities, such as diabetes or fibrosis. I aim to reproduce, identify and quantify ischemia-induced arrhythmogenic mechanisms. Characteristics of the ischemic region could be potentially associated with specific biomarkers extracted from the simulated ECG signal and different levels of arrhythmic risk.

Chapter 6 consists on a study in which I investigate the interplay between variable Na^+ availability co-existing with acute myocardial ischemia, and the subsequent effects on arrhythmic risk. I seek to unravel the mechanisms underlying the high occurrence of cardiac events and high mortality among ischemic patients with low Na^+ availability. Thereby, I quantified arrhythmic risk and provided mechanistic evidence explaining the increased arrhythmic risk associated with reduced Na^+ channel availability, as observed in patients with SCN5A mutations (such as Brugada syndrome) and patients treated with Na^+ blockers, such as flecainide (CAST trials).

Chapter 7 is the last chapter of this thesis. Conclusions from the main results obtained in this research are presented and discussed. Finally, the limitations of this thesis are described, and possible future research lines are suggested.

2 LITERATURE REVIEW: CARDIAC ELECTROPHYSIOLOGY AND ACUTE MYOCARDIAL ISCHEMIA

This chapter presents the fundamental principles of human cardiac function, anatomy and electrophysiology of relevance for this thesis, from the ionic level to whole organ scale. The main electrophysiological features of human ventricular tissue are discussed, and the measures used for their quantification are provided. Additionally, ischemia-induced electrophysiological changes in the cardiomyocytes and their relation to arrhythmogenesis are discussed due to their central role in this thesis.

The crucial role of the ECG in clinical diagnosis is explained, including the main ECG abnormalities associated with ischemia. In the last section of this chapter, I provide a brief overview of the arrhythmogenic conditions linked to alterations in the ionic currents, potentially induced by mutations or pharmacological treatments, since acquired or genetic channelopathies may increase substantially the risk of adverse cardiac events by altering the electrophysiological substrate.

2.1 Cardiac function and anatomy

The heart is the main organ of the circulatory system and provides continuous blood supply to the whole body. Thus, the main function of the heart is to provide nutrients and oxygen to the body, but also to facilitate the removal of metabolic waste. It consists

of four chambers: the left and right atria (LA, RA) and the left and right ventricles (LV, RV).

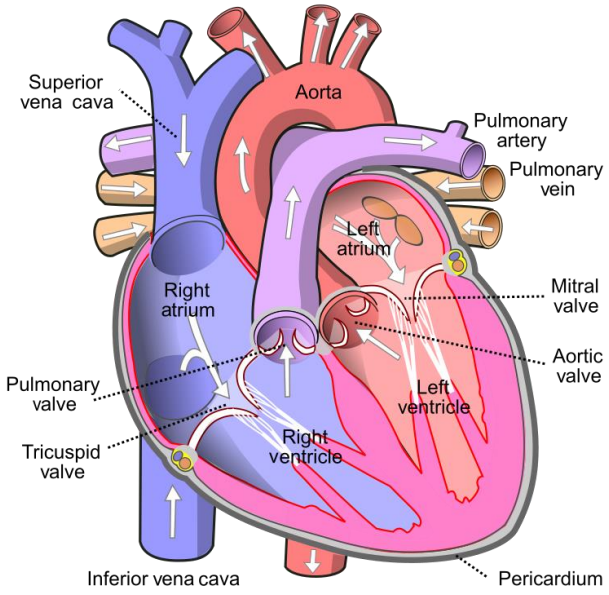


Figure 2.1. Longitudinal cross-section of the heart showing the main blood vessels and chambers. Arrows represent the blood flow in pumping action. Blue shaded regions correspond to chambers and vessels pumping de-oxygenated blood into the lungs to be re-oxygenated. Red shaded areas represent chambers and vessels pumping oxygenated blood into the body. Reproduced from Wikimedia Commons under open access license.

The anatomical portion separating both ventricles is known as the septum, the top part of the ventricles as the base and their bottom part as the apex. Figure 2.1 displays a schematic view of the heart in which the main blood vessels and chambers are annotated. The ventricles push the blood to the lungs and the rest of the organs. The left ventricular (LV) wall is thicker than the right ventricular (RV) due to higher systemic pressures compared to the pulmonary circulation. Blue areas in the figure correspond to the de-oxygenated blood pathway, whereas the red-coloured ones represent re-oxygenated blood flow.

Blood with low levels of oxygen and high levels of carbon dioxide enters the RA via the superior and inferior vena cava and blood enters the RV through the tricuspid valve. With the heart contraction, blood in the RV is pushed into the pulmonary arteries through the pulmonary valve. In the lungs, blood releases carbon dioxide and takes oxygen. Blood is pumped back to the heart, specifically the LA, through the pulmonary

veins. Finally, the blood goes through the mitral valve into the LV, where it is pumped back to the rest of the body by cardiac contraction to remove metabolic waste and provide oxygen and nutrients.

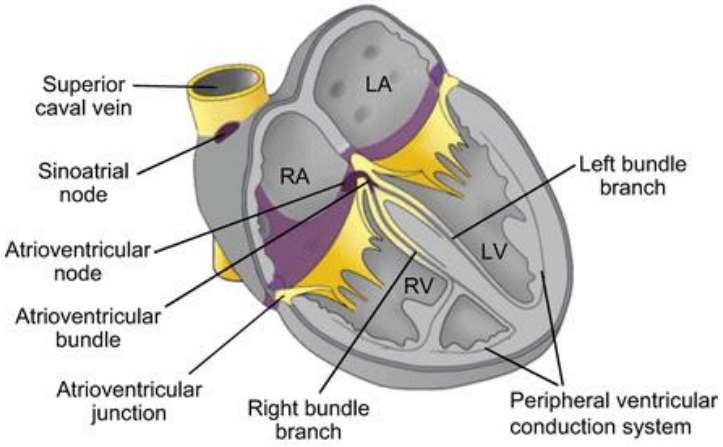


Figure 2.2. Schematic representation of the fast conduction system in the heart. Reproduced from (Weerd and Christoffels, 2016) under open access license.

An organised activation sequence is required for an efficient blood pumping. The electrical impulse is transmitted through the atria and ventricles via the fast endocardial conduction system, represented in Figure 2.2. The initial electrical signal is produced in the sinoatrial node (SAN), located on the RA wall. The normal and regular rhythm of this electric signal is typically referred to as the sinus rhythm. The electrical signal generated at the SAN propagates across the atria until the atrioventricular node (AV), which connects the atria with the ventricles electrically and delays conduction. The time difference between excitation in the atria and ventricles (about 0.09 s) is crucial for the placement of blood in the ventricular cavities, so it can be pumped when the ventricles are excited (Campbell et al., 2003).

Electrical activity propagates quickly through the rest of the system: the bundle of His, two bundle branches and the Purkinje fibres, distributed along the ventricular wall. This ensures coordination of ventricular contraction for optimising the blood pumping action.

The muscle tissue in the heart is known as the myocardium, which consists of the following layers: endocardium (inner layer), mid-myocardium and epicardium (outer layer). Myocardial tissue is formed by cardiac cells, or cardiomyocytes, which are long and tubular in shape, organised into sheets, as shown in Figure 2.3 (left). Cardiomyocytes in these sheets are arranged into fibres, whose orientation vary from

the endocardium (+60 degrees) to the epicardium (-60 degrees), as displayed in Figure 2.3, right panel. The orientation of cardiac muscle fibres establishes the preferential direction of electrical propagation and contraction, defining the electrical activation sequence along the myocardium and hence the contraction mechanics (Caldwell et al., 2009).

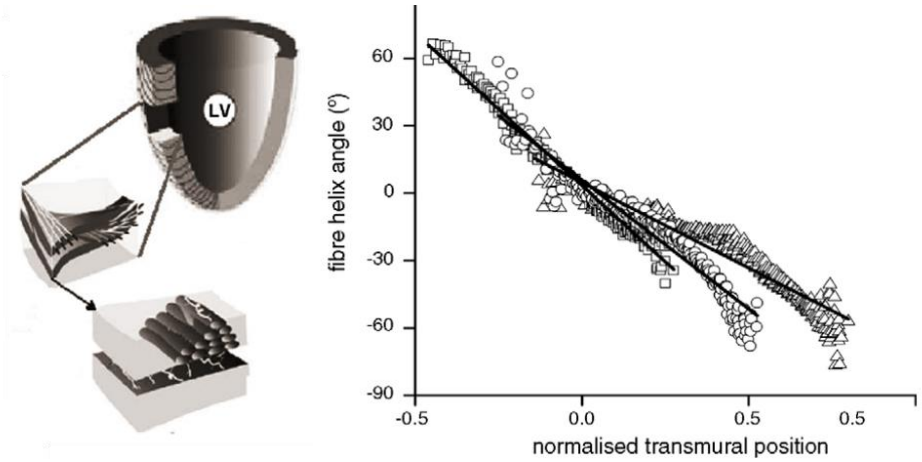


Figure 2.3. Structure of the muscle fibres in the myocardial tissue. Left: Schematic representation of cardiac microstructure. Right: combined transmural fibre helix angle measured in interpapillary muscle region of the equatorial slice of three canine hearts. Reproduced from (Gilbert et al., 2007) under permission of Oxford University Press.

Cardiomyocytes are electrically coupled with each other by gap junctions and are therefore able to propagate electrical signals very fast. As a result, the contraction of the myocardial tissue is produced in an organised pattern, maximising the efficiency of blood pumping. Anatomical or functional obstacles in the electrical propagation caused by pathological conditions in the myocardium, such as ischemia, infarction or fibrosis, can have negative effects, not only on the blood pumping action but also in the formation of lethal arrhythmias.

Blood irrigation in the myocardial tissue is supplied via the coronary arteries. The two main coronary arteries exit from the aorta: the left and the right coronary arteries (LCA and RCA, respectively), which branch in the arteries connected to the myocardium. In individuals with a right-dominant circulation, the RCA supplies the posterior region of the septum, whereas in individuals with left-dominant circulation (only 8% of the population), the left circumflex artery (LCX; originating from the LCA), supplies that area (Parikh Nisha I. et al., 2012).

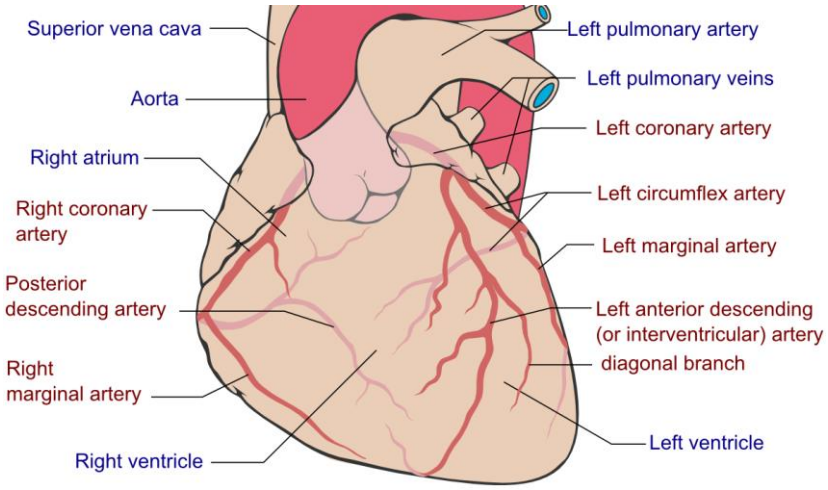


Figure 2.4. Schematic view of the coronary arteries (red) and the areas perfused by them. Reproduced from Wikimedia Commons under open access license.

In addition, collateral circulation between coronary arteries has a protective role in the heart. Collateral arteries are anastomotic vessels connecting epicardial coronary arteries, which provide an alternative blood supply in case the primary vessel is occluded (see Figure 2.5). Nevertheless, collateral circulation is more predominant in certain animal species, such as guinea pig or dog, compared to human (Chorro et al., 2009; Clauss et al., 2019).

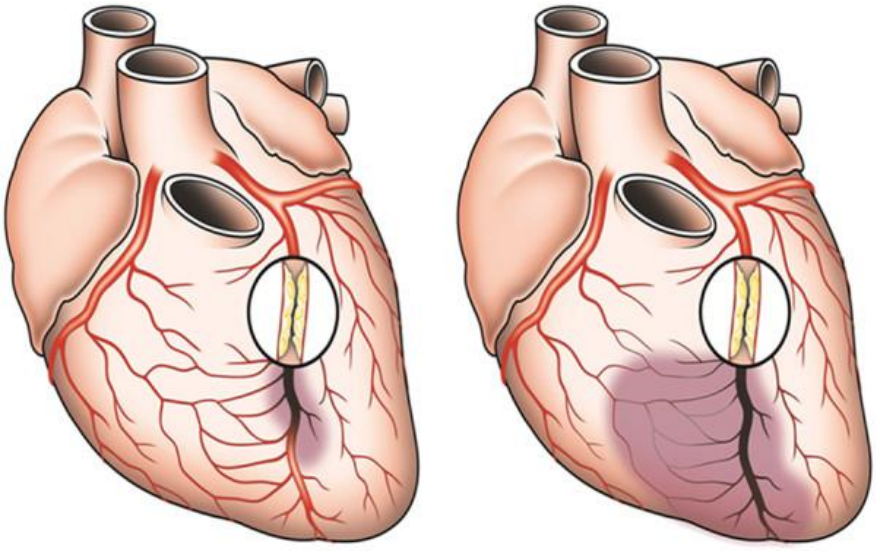


Figure 2.5. Schematic illustration of the coronary artery circulation with (left) and without (right) arterial anastomosis between the right coronary artery and the occluded LAD artery. The grey area indicates the area at risk for myocardial ischemia in case of the LAD occlusion for each of the cases. Reproduced from (Meier et al., 2013) under open access license.

2.2 Electrophysiology of cardiomyocytes

The cardiac action potential (AP) represents the change over time of transmembrane potential in a cardiomyocyte. The process starts when an electrical impulse is applied to the cell. The transmembrane potential in the cell changes drastically, and then gradually recovers its resting state.

Different proteins participate in the AP: ion channels, exchangers and ion pumps, changing their activity during the AP course and promoting the influx or outflux of ions through the cell membrane (primarily sodium, calcium and potassium).

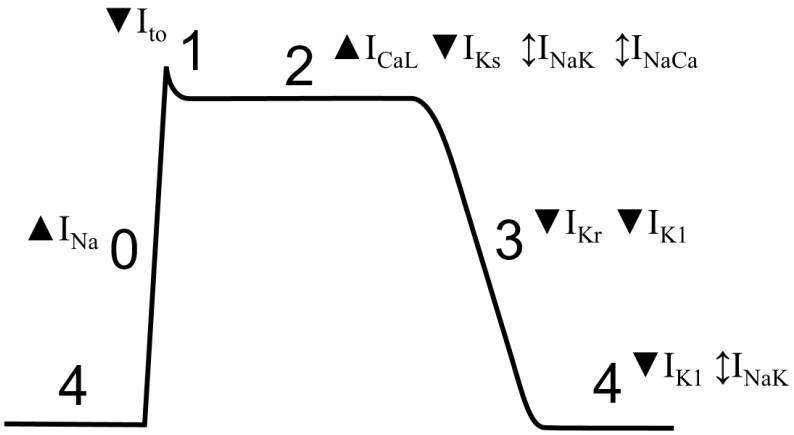


Figure 2.6. AP phases in ventricular cardiomyocytes. The main ion pumps, exchangers and ion channels for each phase are annotated. Ion flux direction in relation to the cardiomyocyte is specified: outward (down), inward (up) and exchange (double arrow).

The intracellular space of cardiomyocytes contains a higher concentration of potassium ions (K^+) and a lower concentration of sodium ions (Na^+) than the extracellular space. In the absence of an external stimulation, the inward and outward ion exchange in the cell membrane is kept constant, ensuring that the membrane potential remains balanced (around -90 mV) in resting state. The AP is triggered by an electrical impulse in the neighbouring cell. Although the AP varies for different species and different types of cardiomyocytes, it can be divided in general into the 5 distinct phases displayed in Figure 2.6:

Phase 0, rapid upstroke phase. The depolarisation is mainly produced by the activation of the fast inward sodium channel (I_{Na}), and the transmembrane potential rises drastically in a short time.

Phase 1, transient repolarisation phase. Whilst I_{Na} is inactivated, a K^+ flow is carried by the transient outward current (I_{to}).

Phase 2, plateau. The membrane potential is maintained by a balance of an inward current carried mostly through the L-type calcium channels (I_{CaL}) and a sum of currents containing the slow component of the slow-delayed rectifier potassium channels (I_{Ks}), the sodium-calcium exchanger (I_{NaCa}) and the sodium-potassium pump (I_{NaK}). This results in the movement of Ca^{2+} into the cell and K^+ out of the cell.

Phase 3, repolarisation. Whilst I_{CaL} is inactivated, I_{Ks} remains open in addition to the rapid delayed rectifier channels (I_{Kr}) and the inward rectifier K^+ channel (I_{K1}). As a result, the transmembrane potential is decreased to the resting potential.

Phase 4, resting membrane potential. The sodium-potassium pump (I_{NaK}) and I_{K1} are responsible for keeping the ionic flow steady in the cell at resting state.

Under healthy conditions, intracellular potassium concentration ($[K^+]_i$) is about 100mM, much higher than in the extracellular domain (normal levels of $[K^+]_o$ are within the range of 3.5 to 5.5mM) (Carmeliet, 1999; Lee and Fozzard, 1975). The I_{NaK} pump modulates the activity of K^+ and Na^+ ions: for every 3 Na^+ ions moved out of the cell 2 K^+ ions are moved into the intracellular domain. This mechanism increases positive charge and Na^+ concentration in the extracellular domain (~140mM), and reduces intracellular Na^+ concentration (4-16mM) (Carmeliet, 1999). Changes in transmembrane potential activates the I_{Na} channel, allowing Na^+ ions to flow into the cell during the depolarisation phase. K^+ ions are moved out of the cell during repolarisation and the membrane potential decreases to the resting potential. In addition to Na^+ and K^+, Ca^{2+} ion fluxes play a relevant role in the cell AP. Ca^{2+} concentration is significantly higher in the extracellular domain than inside the cell (2mM vs. 100-400uM) (Carmeliet, 1999), but during the plateau phase the I_{CaL} current introduces Ca^{2+} ions into the cell. The presence of Ca^{2+} ions produces the release of further Ca^{2+} ions (referred to as *calcium-induced calcium release*) present in the subcellular organelle known as sarcoplasmic reticulum. The Ca^{2+} ions bind to troponin-C proteins on actin filaments, which facilitates the binding of myosin, leading to muscle contraction. Afterwards, Ca^{2+} ions are restored to the sarcoplasmic reticulum, and their excess moved out of the cell by the I_{NaCa} exchanger.

As described above, cardiomyocytes respond to electrical stimuli by generating an AP. However, when an AP is triggered, the cell cannot fire a second AP during a certain time interval, known as the effective refractory period (ERP). Under healthy conditions, the ERP is similar to the AP duration and prevents the cardiac cell from second depolarisations, potentially pro-arrhythmic. Impaired refractoriness of ion channels might therefore result in AP abnormalities. For instance, I_{Na} unavailability or block increases cell refractoriness by delaying the recovery of the current, postponing the recovery of excitability (Osadchii, 2017; Roden, 1996).

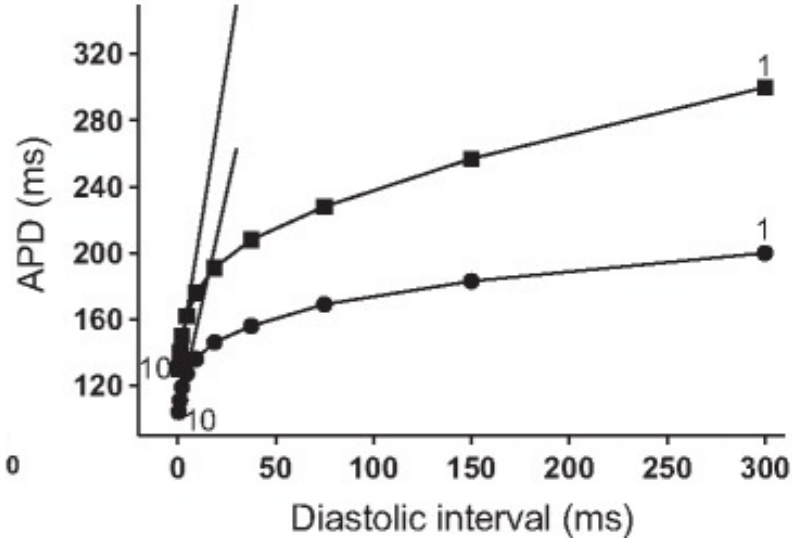


Figure 2.7. Restitution curves constructed on the human endocardium at varying diastolic intervals. Reproduced from (Shattock et al., 2017) under open access license.

The rate-adaptation of the AP duration is crucial for normal cardiac function. AP shortening is required at fast pacing frequencies, since ion channel availability needs to recover quickly for the firing of the next AP. The duration of a complete cardiac pumping cycle -systole and diastole- changes according

Due to the variable metabolic needs in the organism, the cardiac frequency can be modulated. Electrophysiology of cardiomyocytes adapts to the time interval established from one stimulus to the next. This period is commonly known as *cycle length* (CL). This adaptation is observable in the *AP restitution* curves (see Figure 2.7): the action potential duration (APD) of a cardiomyocyte is reduced when the cell is stimulated at shorter diastolic intervals.

2.3 Quantifying cardiac cell electrophysiology

The quantification of electrophysiological properties in myocardial tissue is crucial to understand the arrhythmic risk produced by myocardial ischemia. The most relevant ones are described as follows:

Action potential duration (APD). APD is determined by the time difference between the point of maximum upstroke velocity in the AP and the point when the AP signal drops below a specific percentage of AP amplitude in the repolarisation (e.g. APD measurements include APD30, APD50 or APD70 or APD90, representing the time window from depolarisation to 30%, 50%, 70% or 90% of the repolarisation). Ischemia or drug effects are often associated with APD changes in cardiomyocytes.

Effective refractory period (ERP). ERP is defined as the time interval during which a cell cannot be stimulated following cell depolarisation. Under healthy well-perfused and well-oxygenated conditions, APD and ERP are similar. However, diverse pathologies prolong refractoriness in cardiomyocytes, such as ischemia, due to an abnormally high extracellular potassium concentration and reduced I_{Na} availability (Carmeliet, 1999).

Post-repolarisation refractoriness (PRR). This biomarker is calculated as the difference between ERP and APD. Under control conditions, it should be close to zero but can increase in ischemia.

Resting potential (V_{rest}). In human ventricular cardiomyocytes, V_{rest} is around -85 mV under healthy conditions (O'Hara et al., 2011). Abnormal V_{rest} values are associated with an unbalanced ionic distribution between the intracellular and extracellular domains, which may affect cell function. Hyperkalemia increases V_{rest} due to an accumulation of K^+ ions in the extracellular space ($[K^+]_0 > 5.5$mM).

Maximum upstroke velocity (dV/dt_{max}). The maximum velocity in the depolarisation upstroke of the AP (phase 0) reflects cell excitability and is mostly determined by the fast sodium channel availability (Berecki et al., 2010).

Conduction velocity (CV). CV in myocardial tissue is computed as the distance between two points A and B, divided by the time taken by the activation wave to propagate between both points. It depends strongly on I_{Na} availability and cell coupling, both typically reduced under ischemic and fibrotic conditions.

2.4 Electrophysiological heterogeneities within the myocardium

Ventricular tissue is highly heterogeneous. As mentioned previously, ventricular cardiomyocytes are arranged into sheets, which are organised in fibres. The orientation of cardiomyocytes depends on the relative position within the heart to contribute to an organised electrical activation sequence, and hence to produce an effective contraction mechanism. In addition to structural heterogeneities, ventricular cardiomyocytes show electrophysiological variability, not only between different individuals of the same species but also within the very same heart.

The myocardial wall can be divided into epicardium, mid-myocardium and endocardium, and ventricular cardiomyocytes within each layer differ slightly in their electrophysiological features. Figure 2.8 shows the difference in AP for ovine cardiomyocytes from the endocardial and epicardial layers. For instance, APD tends to be shorter in epicardial cells. These electrophysiological heterogeneities are produced by differences in mRNA and protein expression across the myocardial wall.

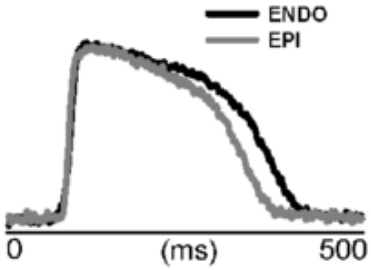


Figure 2.8. AP differences in ovine cardiomyocytes from the epicardium (grey) and endocardium (black). Reproduced from (Martinez et al., 2018) under open access license.

Apicobasal heterogeneities have been extensively reported in experimental studies. It has been shown that these are largely based on differences in potassium currents I_{to} and I_{Ks} (Szentadrassy et al., 2005). Consequently, APD in cardiomyocytes located in the apex is about 40ms shorter than those located in the basal region (Cheng et al., 1999; Salama et al., 1987).

2.5 Acute myocardial ischemia

Under certain conditions, a mismatch between the amount of blood flow required and that supplied may occur, commonly known as *ischemia*. In the myocardium, blood is perfused through the coronary arteries, as shown in Figure 2.4. In case of ischemia, the

poorly irrigated myocardial region suffers electrophysiological changes in a few minutes. Thickening of the arterial walls, the formation of blood clots, atherosclerosis or vasospasms are possible causes of myocardial ischemia.

Myocardial ischemia is a major cause of death in the world. Arrhythmic risk derived from ischemia is not fully understood and many questions remain open. Even though myocardial ischemia has been extensively studied, how ionic changes in tissue result in high pro-arrhythmic risk in patients is not completely understood. Moreover, the diversity in ECG abnormalities and clinical outcome of myocardial ischemia complicates the diagnose and management of patients (Herring and Paterson, 2006), especially in cases with incomplete and reversible coronary occlusions leading to silent ischemia (Park and Richard Conti, 2016; Regitz-Zagrosek, 2011).

Arrhythmogenesis induced by coronary occlusion has been extensively studied (Downar et al., 1977; Janse and Kléber, 1981; Janse et al., 1980). However, the dynamic electrophysiological changes occurring in the myocardium (Carmeliet, 1999; Sutton et al., 2000; Taggart et al., 2000) increase the complexity of studying ischemia-induced arrhythmic risk.

Ischemia-induced arrhythmic risk is highest during the first 15 minutes of post-occlusion (Carmeliet, 1999), a period called *acute ischemia*. The risk of arrhythmias decreases as ischemia turns more severe towards necrosis (Penny and Sheridan, 1983). Three post-occlusion stages can be differentiated: a) phase I, the first 30 minutes; b) phase II, up to 72 hours and c) phase 3, or infarction. Two periods of arrhythmic risk are differentiated within phase I, and classified depending on when they occur: 1a (first 10-15 minutes) and 1b (10-30 min after occlusion) (Ghuran and Camm, 2001; Janse and Wit, 1989).

If blood perfusion is interrupted and ischemia persists for longer periods (>2 h), ischemic cells suffer severe changes, resulting in cellular death and myocardial infarction. If tissue turns necrotic, it can no longer contract and the remodelling of the ventricles affects electrical activation and strain distribution (Richardson et al., 2015). On the other hand, transient ischemia periods are caused by temporal coronary occlusion, followed by blood reperfusion. Coronary reperfusion reverts the formation of infarcted tissue if the damage is reversible, but could cause arrhythmic risk due to

increased instability in cell electrophysiology (Kalarus et al., 2019). The extent of the ischemic region depends on the remaining blood flow allowed in the affected region, co-existing conditions of the myocardial tissue and cell variability.

In this thesis, I simulated the electrophysiological conditions reproduced by acute ischemia 10-15min post-occlusion, during the last period of phase 1A, when the occurrence of arrhythmias is highest.

The main effects of phase 1A acute ischemia on myocardial tissue are hyperkalaemia, acidosis and hypoxia (Kodama et al., 1984; Moréna et al., 1980). Ischemic cells show abnormally high levels of extracellular potassium $[K^+]_0$ as a result of hyperkalemia (Coronel et al., 1988; Weiss and Shine, 1982), decreased I_{Na} and I_{CaL} conductances as a result of acidosis (Irisawa and Sato, 1986; Kagiyama et al., 1982) and the activation of an *ATP*-dependant potassium current $I_{K(ATP)}$ as a result of hypoxia (Noma, 1983).

Cell excitability and conduction velocity are reduced due to decreased conductance in the fast sodium channel. Upstroke velocity in the AP is slower and sodium activation gates take a longer time to recover, increasing the cell ERP. Reduced conductance of I_{CaL}, increase of I_{K1} caused by hyperkalemia and activation of $I_{K(ATP)}$ are responsible for APD shortening in ischemia. Hyperkalemia also contributes to the prolongation of the ERP and increases V_{rest}, reducing the cell's excitability. The severity of electrophysiological changes induced by ischemia is heterogeneous across the tissue, depending on several factors, such as proximity to the occluded vessel, proximity to the ventricular cavity, severity of the coronary occlusion or comorbidities. The central region of the ischemic area is typically referred to as the ischemic core zone (ICZ). The surrounding tissue, or border zone (BZ), has been identified as crucial in the formation of reentrant pathways leading to arrhythmias. The BZ exhibits steep electrophysiological gradients between the healthy tissue and the ICZ, contributing to the formation of abnormal electrical activities (Janse et al., 1980).

The endocardial region of the myocardial wall remains perfused even under ischemic conditions due to its proximity to the ventricular cavity (Wilensky et al., 1986). This promotes transmural electrophysiological heterogeneities (Valderrábano et al., 2001; Wu and Zipes, 2001).

2.6 Cardiac arrhythmia mechanisms

Conditions in which the heartbeat is irregular, too fast or too slow, are known as *arrhythmias*. They are caused by abnormalities in the generation of the electrical impulse or its propagation across the electrical conduction system or myocardial tissue. Ventricular arrhythmias are associated with a higher risk of mortality than atrial ones, due to the critical role of the ventricles in blood supply, requiring immediate action (John et al., 2012; Kalarus et al., 2019; Odutayo et al., 2016). Some arrhythmias can be asymptomatic, such as atrial fibrillation. Contrarily, ventricular fibrillation causes death within minutes (Pionkowski et al., 1983). Arrhythmias are often triggered by one or more of the following mechanisms:

- Delayed afterdepolarisations (DAD). Spontaneous release of Ca^{2+} inducing a I_{NCX} current after the repolarisation phase, depolarising the cell over the AP threshold. It is caused by Ca^{2+} ions overload in the sarcoplasmic reticulum. Ionic remodelling in the ischemic BZ may promote its formation.
- Early afterdepolarisations (EAD). Spontaneous depolarisations during the plateau and repolarisation phase of the AP, promoted by reactivation of the L-type calcium current. They are common in patients with prolonged QT interval.
- Refractoriness dispersion (ΔERP). As described in Section 2.5, ischemic tissue shows shorter APD values and prolonged ERP. These leads to electrophysiological heterogeneities playing a crucial role in ischemia-induced arrhythmogenesis.
- Alternans. It is a periodic beat-to-beat oscillation in cardiac function due to changes in the APD (APD alternans), contraction amplitude (mechanical alternans) or and Ca^{2+} transient alternans. Well-known factors causing alternans are cell uncoupling and spatial heterogeneities in Ca^{2+} cycling.

Specifically, myocardial ischemia is strongly associated with the occurrence of ventricular tachycardia and fibrillation (Buza et al., 2017; Luqman et al., 2007). Ventricular tachycardia (VT) is defined as an abnormally fast cardiac stimulation, overriding the function of the sinoatrial node in sinus rhythm. VT can turn into ventricular fibrillation (VF) as a consequence of wave breakup (Samie and Jalife, 2001). During VF, the heart is depolarised by disorganised electrical activation waves, preventing effective blood pumping and potentially leading to cardiac arrest.

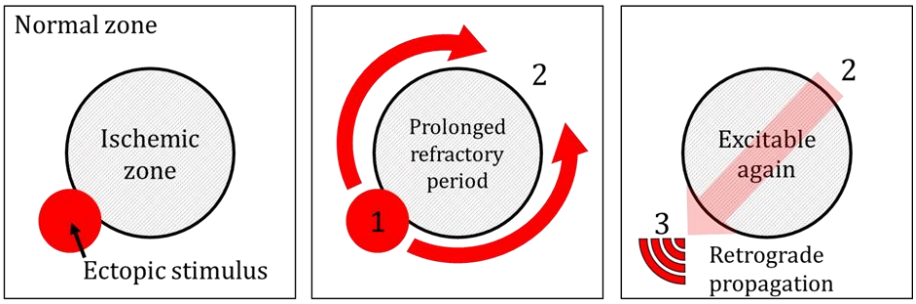


Figure 2.9. Schematic of figure-of-eight reentrant pattern triggered by ischemia.

The steep electrophysiological gradients observed in the ischemic BZ establish an injury current between ischemic and healthy cells, tending to depolarise electrotonically the latter (Coronel et al., 1991). This could promote the formation of ectopic beats capable to propagate across the myocardium and, potentially, form irregular electrical activation patterns. Then, slow conduction velocity and prolonged refractoriness in the ischemic region could promote the formation of reentries: as the activation wave reaches the still refractory ICZ and finds a conduction block, it propagates through the BZ. The wavefront enters the ICZ when refractoriness in the region expires, and potentially reenters the healthy tissue where the original conduction block took place. This is referred to as *figure-of-eight* reentry, described in (Janse et al., 1980) and displayed in Figure 2.9. The vulnerability window (VW) is a quantification method used to estimate the set of a premature or ectopic stimulus leading to a unidirectional conduction block, which is an important precursor of ischemia-induced arrhythmias and hence estimates arrhythmogenesis (Shaw and Rudy, 1995). When a reentry is formed, the scroll wave established could develop additional wavebreaks, degenerating to fibrillation (Weiss et al., 2005).

2.7 Electrocardiogram

An ECG is a non-invasive recording of the electrical activity produced in the heart, represented as a graph of potential versus time. A set of electrodes are attached to the body surface to detect the small electrical changes produced by the depolarisation and repolarisation of the heart, allowing the identification of abnormal cardiac function in the clinical practice.

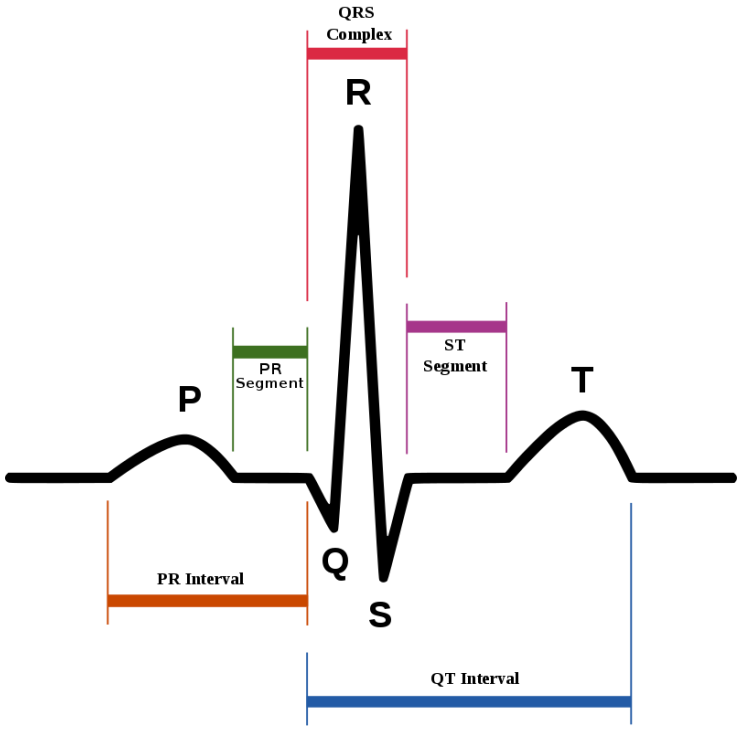


Figure 2.10. Schematic diagram of normal sinus rhythm for a human heart as seen on the ECG. Reproduced from Wikimedia Commons under open access license.

The electrical engineer Alexander Muirhead is credited with the recording of the first ECG in humans, dated in 1872 (Birse, 2004). Willem Einthoven is responsible for a series of developments on measurement and understanding of the electrographic signal, for which he was awarded the Nobel Prize in Medicine in 1924 (Cooper, 1986). Among his achievements, Einthoven developed the first practical system of electrocardiography used for clinical purposes. He gave the name to the ECG deflections, still used nowadays. He correlated certain diseases and disorders to specific ECG features.

The electrocardiographic signal represents the different phases of the cardiac cycle (Figure 2.10):

- P wave represents the depolarisation of the atria.
- QRS complex represents the depolarisation of the ventricles, overlapping with atrial repolarisation.
- T wave represents the repolarisation of the ventricles.

The conventional 12-lead ECG measures the electrical potential from 12 different perspectives based on the 10 electrodes set in the body surface (4 of them on the limbs, 6 on the chest). The 12 leads are classified as follows:

- Bipolar limb leads (I, II, III). They are computed using signals measured from the limb electrodes right arm (RA), left arm (LA), left leg (LL) and right leg (RL). The potential difference between the electrode measurements constitutes the lead signal, as shown in Figure 2.11 (left). For example, lead I represents the electrical potential measured between the LA and RA.
- Unipolar augmented limb leads (aVR, aVL, aVF). They are also computed using the limb electrodes. However, they provide an alternative insight into the electrical activity in the heart, where aVL lead is at -30 degrees relative to the lead I axis; aVR is at -150 degrees and aVF is at +90 degrees. They are termed unipolar as they use the Wilson's terminal (vW) as the negative electrode that averages the measurements from RA, LA and LL electrodes. They have the positive electrodes on the RA (aVR), on the LA (aVL), and on the LL (aVF).
- Precordial leads (V1-V6). A set of 6 electrodes over the heart region on the torso provide 6 different leads reporting the cardiac electrical activity from a plane perpendicular to the frontal one, as seen in Figure 2.11 (right). The vW is used as the ground.
-

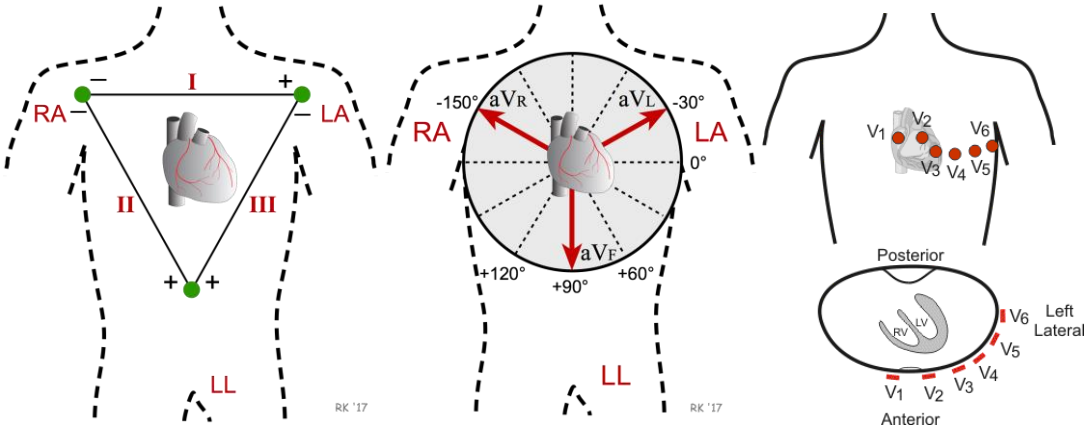


Figure 2.11. Electrode placement in the 12-lead ECG. Left: bipolar limb leads (I, II and III); centre: unipolar limb leads (aVR, aVL and aVF); right: precordial leads (V1-V6) from a frontal and overhead perspective. RA: right arm; LA: left arm; LL: left leg. Reproduced from (Klabunde, 2011) with permission.

Each ECG lead provides especially accurate information of certain areas, which is useful for detecting regionally-located cardiac pathologies, such as myocardial ischemia. In Table 2.1 each coronary artery is associated with their irrigated myocardial

region (Laguna and Sörnmo, 2014; Menting and van Mechelen, 2012; Tsuka et al., 2001). For example, the occlusion of the left anterior descending (LAD) coronary artery would lead to ischemia in the anterior region of the myocardium and therefore leads V3 and V4 are usually the most adequate for detecting ischemia caused by LAD occlusion.

Myocardial region affected	Coronary artery occluded	Suitable leads to reflect ischemia
Inferior region	RCA	II, III, aVF
Lateral region	LCX	I, aVL, V5, V6
Septal region	LAD	V1, V2
Anterior region	LAD	V2, V3, V4

Table 2.1. Suitable leads for detecting ischemia in different regions of the myocardium and the coronary artery most likely causing ischemia.

2.8 Ischemia-induced abnormalities in the ECG

Cardiac diseases affect the electrocardiogram in different ways, allowing the correlation of certain ECG abnormalities with specific pathologies. Quantification of ECG biomarkers is a widely used assessment tool for ischemia, despite its lack of specificity. The most used biomarker for ischemia detection is ST segment deviation. ST elevation results from the electrophysiological heterogeneities induced by regional myocardial ischemia (Samson and Scher, 1960) based on shorter APs and higher resting membrane potential in the ischemic cells.

The literature has reported extensively on the correlation between the transmural extent of the ischemic region and the deviation of the ST segment: ST elevation myocardial infarction (STEMI) is typically associated with severe coronary occlusions producing fully transmural ischemic regions, whereas ST depression is linked with the occlusion of smaller vessels or uncomplete coronary occlusions, promoting subendocardial ischemic regions (Birnbaum and Drew, 2003; Potse et al., 2006; Wilhelms et al., 2011).

Figure 2.12, extracted from (Klabunde, 2011), describes the mechanism causing ST deviation in myocardial ischemia. Panel A links subendocardial ischemia with ST depression. A higher resting potential in the subendocardial ischemic region establishes a positive current towards the ECG electrode (Panel A, left and right), causing higher electrical potential measurements than 0mV. This potential dispersion caused by

regional ischemia (Figure 2.12, panel A, left and right) requires the isoelectric line (0 mV) to be corrected.

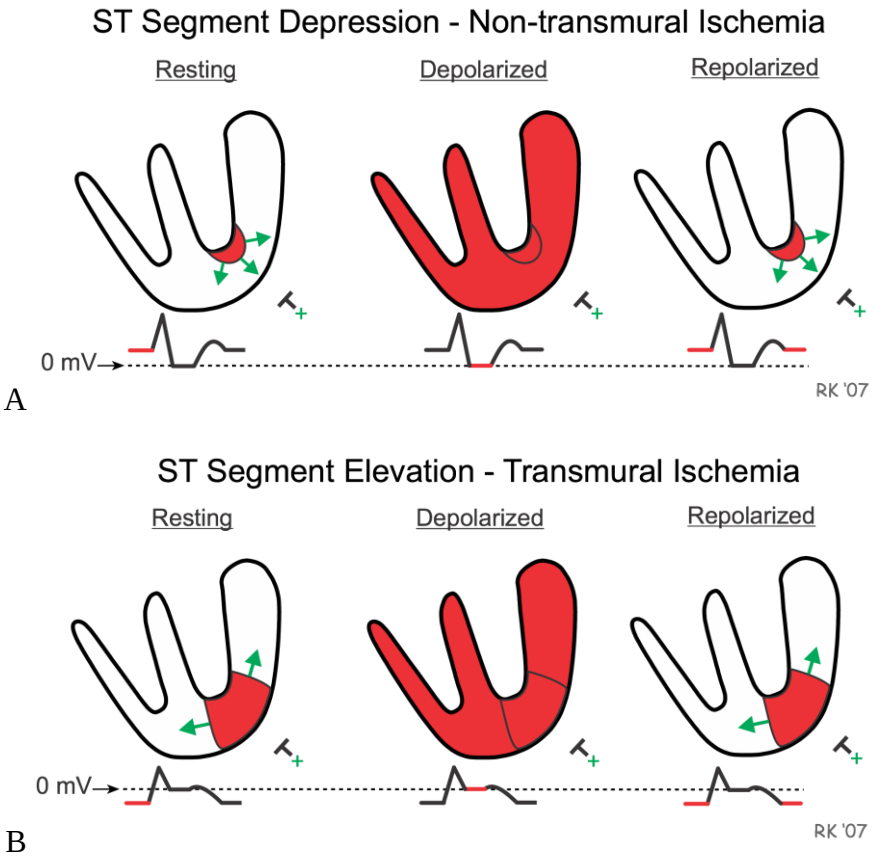


Figure 2.12. Mechanism underlying ST segment deviation induced by subendocardial (A) and transmural ischemia (B). Reproduced from (Klabunde, 2011) with permission.

When the myocardium is depolarised at its full extent, no gradients in electrical potential are present and this would be considered the baseline (Figure 2.12, panel A, centre). The correction of the isoelectric baseline leads to ST depression, which is characteristic of myocardial ischemia. Under transmural ischemia conditions, the mechanism is similar, but the main differences are raised by the spatial distribution of the ischemic region. Panel B (left and right) shows that the injury current induced by the ischemic region has an opposite direction than in Panel A, leading to ST elevation, characteristic of transmural myocardial ischemia.

Some authors have used ST segment deviation to estimate the location and size of the ischemic region (Andersen et al., 2010; Sarafoff et al., 2013). But most importantly, ST deviation has been considered a suitable biomarker for arrhythmic risk assessment. Symptomatic myocardial ischemia (inducing chest pain and ST elevation) is generally

linked with higher mortality among ischemic patients (Zellweger et al., 2003). However, patients suffering from silent ischemia or transient ischemia episodes are still associated with a great occurrence of adverse cardiac events (Ahmed et al., 2007; Gottlieb et al., 1986, 1988). Arrhythmic risk stratification in asymptomatic ischemia is substantially worsened by the difficulties that arise due to its diagnosis or management (Chan et al., 2009; Shea et al., 1985). Some authors have reported remarkable differences in ischemic symptoms between men and women (Regitz-Zagrosek, 2011; Wake and Yoshiyama, 2009), urging the need to improve diagnosis and treatment especially in female patients (British Heart Foundation, 2019b). Furthermore, ischemia-induced arrhythmic risk is accentuated by existing comorbidities, such as hypertrophic cardiomyopathy (Raphael et al., 2016), diabetes mellitus (Park and Richard Conti, 2016) or Brugada syndrome (Benito et al., 2008).

2.9 Safety and efficacy of anti-arrhythmic drugs

Due to their non-invasive nature, pharmacological treatments are commonly used as a prophylactic measure against the formation of arrhythmias. Anti-arrhythmic agents can be divided into the following categories, according to the classification proposed by (Lei Ming et al., 2018):

a) Class 0. Drugs acting on sino-atrial automaticity, such as ivabradine.
b) Class I. Sodium channel blockers, such as flecainide or quinidine.
c) Class II. Beta-blockers, such as propranolol or timolol.
d) Class III. Potassium channel blockers, such as dofetilide or ibutilide.
e) Class IV. Ca^{2+} blockers and CaMKII modulators, such as verapamil and diltiazem.
f) Class V. Drugs acting on mechanosensitive channels.
g) Class VI. Drugs acting on connexin-associated channels.
h) Class VII. Drugs acting on upstream modulatory targets, such as renin-angiotensin-aldosterone inhibitors.

It is important to mention that anti-arrhythmic agents usually affect more than one ionic channel. For example, quinidine's main action mechanism is the block of the fast inward sodium current (I_{Na}), and therefore it is identified as a class I anti-arrhythmic drug. However, the drug affects other ionic channels, such as I_{Ca}, I_{Kr}, I_{Ks}, I_{to} and $I_{K(ATP)}$.

Like most pharmacological compounds, certain anti-arrhythmic drugs can be associated with severe side-effects, some of them lethal, including the occurrence of cardiac events.

For instance, flecainide is considered an effective treatment for atrial fibrillation (Aliot et al., 2011), but it has been associated with high mortality amongst patients suffering from CAD, inducing an increased arrhythmic risk and an elevated occurrence of lethal arrhythmias, as reported in the CAST trials (Anderson et al., 1994; Cardiac Arrhythmia Suppression Trial II Investigators, 1992; Echt et al., 1991). In this trial, ischemic episodes were not more frequent in patients using the drug, but cardiac events and death were more likely among patients using flecainide than in placebo patients. The mechanism of action of flecainide interferes with the sodium channel (Hondeghem and Katzung, 1984), which plays a key role in the excitability and refractoriness of cardiomyocytes. Thereby, flecainide is strongly contraindicated for patients under ischemic risk or suffering any structural heart disease (Aliot et al., 2011), especially those suffering recurrent ischemia episodes caused by a restricted coronary blood flow (Anderson et al., 1994; Greenberg et al., 1995).

Not only anti-arrhythmic drugs are associated with pro-arrhythmic side-effects, but pharmacological compounds used for other pathologies may also promote arrhythmias. Tyrosine-kinase inhibitors (TKIs), such as imatinib, sunitinib or nilotinib, are commonly used as first-line cancer treatments (Pasvolsky et al., 2015). The use of TKI agents has transformed cancer from a fatal disease into a manageable chronic condition, although they have been extensively associated with the occurrence of adverse cardiac events. For example, nilotinib has been linked with coronary vasospasms leading to CAD in treated patients (Kim et al., 2012). Other common cardiotoxic effect in many TKIs is the induction of long QT syndrome based on potassium blockage, and the concomitant increased risk of SCD (Kloth et al., 2015).

Conclusion

Ischemia-induced arrhythmic risk is highest a few minutes post-coronary occlusion. The arrhythmogenic mechanisms caused by ischemia have not been completely elucidated due to the rapidly changing electrophysiological conditions of ischemia and the immediacy required in patient management. Analysis of the electrocardiographic signal

is useful to detect certain cases of myocardial ischemia, but some of the patients remain asymptomatic, complicating the diagnosis. Management of patients in ischemic risk contemplates severe complications, such as potentially lethal side effects derived from drug treatments. Variability in ischemia-derived ECG changes and prognosis remains not completely understood. This could be addressed by unravelling the underlying arrhythmogenic mechanisms. Additionally, this could promote the identification of new effective therapies and shed light on previously published clinical studies. In the next chapter I present the methods and tools used to construct a computational framework for modelling and simulating acute myocardial ischemia.

3 COMPUTATIONAL METHODS FOR MODELLING AND SIMULATION OF CARDIAC ELECTROPHYSIOLOGY

As in many other disciplines, computational modelling has transformed traditional research strategies in the field of cardiac electrophysiology, proposing an alternative and complementary framework for investigation. Within the scope of this thesis, a computational pipeline was constructed for modelling and simulating human cardiac electrophysiology under healthy and ischemic conditions using high-performance computing resources. In this chapter, I present the methods and tools used to construct the computational framework, including the electrophysiological model from cell to organ scales, in addition to relevant aspects of the methods employed in its numerical solution.

3.1 Modelling the action potential and cell electrophysiology

During the last 50 years, multiple computational cardiac cell models have been published. These models are based on experimental data, frequently obtained from a combination of human and animal measurements to circumvent the scarcity of available human data. Current cellular models have experimented many iterations during their construction and refinement since experimental and clinical data have been used for both the construction of the simulation and modelling framework and its posterior

verification and validation, as exemplified in (Carusi et al., 2012; Noble and Rudy, 2001). These extensively evaluated models are suitable for investigating existing mechanisms that remain still unclear in cardiac electrophysiology.

Another crucial aspect of a cardiac cell model is the level of complexity used for representing the underlying ionic mechanisms. The level of detail in ion channel formulation depends not only on data availability but also on the expected use for the model. As George Box said, “all models are wrong, but some are useful”. Thereby, the suitability of a certain cardiac cell model is strongly determined by its application.

Although cardiac cell models have been used extensively for academic research, the use of biophysically-detailed models for regulatory and industrial purposes has increased significantly in recent years after the launch of the CiPA initiative, sponsored by the US Food and Drug Administration (Sager et al., 2014). In this regard, Passini et al. have shown a higher accuracy in predicting clinical arrhythmic risk using human cardiac models compared to experimental animal models (Passini et al., 2017).

The first cardiac cell model was published in 1962 by Denis Noble (Noble, 1962), as an adaptation of the Hodgkin-Huxley model of the AP in the squid giant axon. Since then, dozens of cardiac cells models have been published (Noble, 2011; Trayanova, 2011). Common to most of these models, the biophysical activity of ionic currents and concentrations in cardiomyocytes is described by a system of ordinary differential equations (ODEs).

In the next section, I will describe the seminal model by Hodgkin-Huxley for the AP of the isolated squid giant axon, in which most of the models developed over the last 50 years are based on. I will also provide an overview of the most relevant ones, including the state-of-the-art O’Hara-Rudy model, the one used in this thesis.

3.2 The Hodgkin-Huxley model

Sir Alan Lloyd Hodgkin and Sir Andrew Fielding Huxley received the 1963 Nobel prize in physiology or medicine for their work on the electrical impulse propagation in the squid giant axon, concluding with their seminal quantitative model describing its underlying ionic mechanisms (Hodgkin and Huxley, 1952a, 1952b, 1952c, 1952d; Hodgkin et al., 1952). This model represents the basis for many other AP models.

The electrical activity in this model is modulated by 3 main ionic currents: the sodium channel (I_{Na}), the potassium channel (I_K) and an unspecific leakage channel (I_l). Each current is defined by the following equations:

$$I_{Na} = g_{Na}(V - E_{Na}),$$
$$I_K = g_K(V - E_K),$$
$$I_l = g_l(V - E_l),$$

where g_{Na}, g_K, g_l and E_{Na}, E_K, E_l represent the conductances and reverse (or equilibrium) potentials for each of the ionic channels in the model, respectively. V represents the membrane potential of the cell. Whereas g_l is constant, g_{Na} and g_K are described by the equations:

$$g_{Na} = \bar{g}_{Na}\, m^3 h,$$
$$g_K = \bar{g}_K\, n^4,$$

where $\bar{g}_K$ and $\bar{g}_{Na}$ are constants representing maximal conductance per cm^2, and m, h and n are the so-called gating variables, varying in the range [0, 1] in order to describe the opening and closing of the ion channels. Each of the gating variables is calculated by an equation of the form:

$$\frac{dx}{dt} = \alpha_x(V) \cdot (1 - x) - \beta_x(V) \cdot x,$$

where x represents gating variables (m, h or n). The variables α_x and β_x, which depend on the transmembrane potential V, determine the opening and closing rates of the gate, respectively, and the equations defining them were fitted to reproduce experimental findings:

$$\alpha_m = 0.1\frac{25 - V}{e^{\frac{25-V}{10}} - 1}, \qquad \beta_x = 4e^{-\frac{V}{18}},$$

$$\alpha_h = 0.07e^{-\frac{V}{20}}, \qquad \beta_h = \frac{1}{e^{\frac{30-V}{10}} + 1},$$

$$\alpha_n = 0.01\frac{10 - V}{e^{\frac{10-V}{10}} - 1}, \qquad \beta_n = 0.125e^{-\frac{V}{80}}$$

3.3 Ventricular action potential models during the last decades

Cardiac cell models published since the Hodgkin-Huxley model show wide variability in different aspects. Models have been proposed for simulating the electrophysiology of cardiomyocytes in different species, such as dog (Hund and Rudy, 2004), rabbit (Shannon et al., 2004), rat (Niederer and Smith, 2007) or human (Grandi et al., 2011; O'Hara et al., 2011; ten Tusscher et al., 2004). Some models simulate the AP either in atrial (Grandi et al., 2011; Maleckar et al., 2009) or ventricular cardiomyocytes (O'Hara et al., 2011). Additionally, ion channel dynamics can be simulated with either the Hodgkin-Huxley or Markov-chain formulations (Carbonell-Pascual et al., 2016). Another difference between models is the degree of complexity implemented. Depending on their planned use, the model needs to provide a balance between feasibility and accuracy with respect to experimental data. The set of ionic currents or the number of state variables included in a model could be considered as a surrogate of its complexity. For example, the O'Hara-Rudy model has 41 state variables, whereas the Noble model only 4.

Initially, it was suggested that cardiac electrophysiology could be studied with modest extensions of the Hodgkin-Huxley equations, described in the previous section. Noble's model satisfied that premise, but incorporated additional currents I_K and I_{K1}, both identified with experimental measurements (Noble, 1962). Some decades later, the Luo-Rudy cardiac cell model was published (Luo and Rudy, 1991), which has been extensively used in research, including ischemia (Ferrero et al., 1996; Rodríguez et al., 2006; Shaw and Rudy, 1997; Trénor et al., 2005). It was built based on recordings in single cell and channel recordings obtained from different mammalian species. Finally, one of the first models widely used of the human ventricular AP was developed by ten Tusscher and Panfilov (TP06) (Ten Tusscher and Panfilov, 2006). This is an updated version of a model by the same group (ten Tusscher et al., 2004), with the purpose of producing a human cardiac model suitable for multiscale modelling, and a better representation of intracellular calcium handling. It has also been commonly used for studying ischemia (Dutta et al., 2016; Moreno et al., 2011; Wilhelms et al., 2010).

In the present thesis, the O'Hara-Rudy model (ORd) for human ventricular myocytes represents a fundamental part for investigating arrhythmogenic mechanisms facilitated

by acute myocardial ischemia and drug-induced cardiotoxicity. Due to its relevance within this thesis, it will be thoroughly described in the next section.

3.4 The O'Hara-Rudy model

The ORd model is based on experimental recordings obtained from more than 100 undiseased human hearts. These experimental measurements were conducted to collect data used for constructing various currents (I_{CaL}, I_{NaCa}, I_{to}, I_{K1} and I_{Kr}). Here I provide a detailed description of the main ionic channels and the origin of the data used for their formulation, followed by a schematic diagram of the ORd model (Figure 3.1). Further information regarding the formulation of each ion channel is provided in the Supplementary Materials of the original article (O'Hara et al., 2011).

The fast sodium current (I_{Na}) was constructed using data from (Nagatomo et al., 1998; Sakakibara et al., 1993) to adjust for temperature differences. Ca^{2+}/calmodulin-dependent protein kinase II effects in the sodium channel were implemented based on data from (Wagner et al., 2006). A late sodium current (I_{NaL}) was incorporated into the model and constructed using data from (Maltsev et al., 1998). This slow current takes place in the repolarisation phase and was not included in the TP06 model.

One of the strongest aspects of the ORd model is the inclusion of a detailed formulation of calcium dynamics. Compared to other human cardiac AP models, the ORd model incorporates a detailed description of the Ca^{2+}/calmodulin-dependent protein kinase (CaMK) signalling pathway, which is crucial for determining frequency dependence of Ca^{2+} cycling (Hund and Rudy, 2004; Livshitz and Rudy, 2007). Despite the minor effects of CaMK on other ionic channels, it is key to reproduce alternans in human cardiomyocytes, a well-known mechanism of arrhythmogenesis. Although the L-type calcium current (I_{CaL}) in the ORd model is similar to those in other models of non-human cardiomyocytes (Decker et al., 2009; Mahajan et al., 2008), the authors conducted new measurements on human cardiomyocytes to provide a more accurate formulation. The more detailed Ca^{2+} dynamics in the ORd model show more accurate rate dependence than its predecessors, which leads to more realistic APD70, APD50 and APD30 values.

The transient outward potassium current (I_{to}), the rapid delayed rectifier potassium current (I_{Kr}) and the inward rectifier potassium current (I_{K1}) were also based on new data collected by O'Hara et al. due to limitations in previous human data. The slow delayed rectifier potassium current (I_{Ks}) was formulated based on experimental data from humans (Virág et al., 2001), whereas its dependence with calcium ionic concentration was defined using experimental data from guinea pigs (Tohse, 1990).

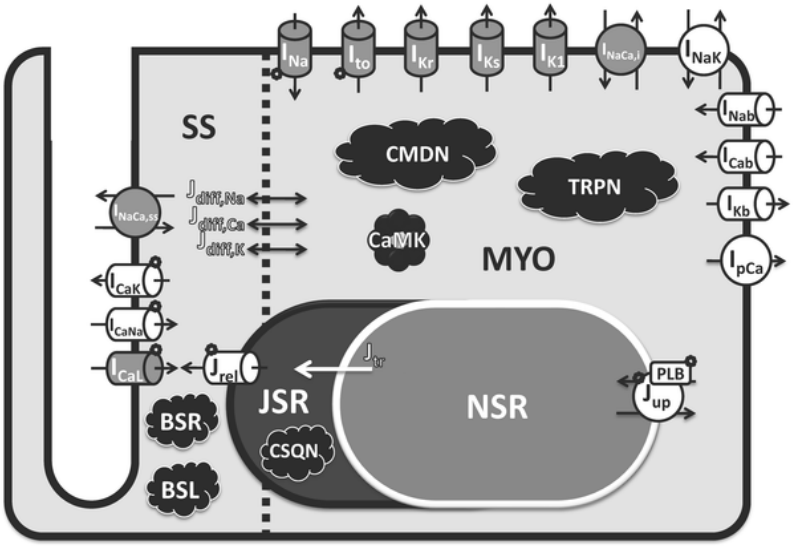


Figure 3.1. Schematic diagram of the ORd model. Reproduced from (O'Hara et al., 2011) under open access license.

Moreover, although the TP06 reproduce early afterdepolarisations (EADs), the occurrence of these electrophysiological abnormalities was validated in the ORd model with human undiseased experimental data from (Guo et al., 2011), using identical stimulation protocols. The model includes transmural heterogeneities by incorporating mRNA and protein expression variation in endocardial, mid-myocardial and epicardial cardiomyocytes.

In conclusion, the ORd model brings together in a human cardiac AP model a full set of features, many of them based and improved on aspects from previously published models and using extensive experimental data for validation. Thereby, the ORd is considered the most up-to-date and extensively validated human cardiac AP model. In the next section, I describe the modifications incorporated into the ORd model for this thesis.

3.5 Modifications on the O'Hara-Rudy for simulating ischemia

The $I_{K(ATP)}$ current is activated under hypoxic conditions, which leads to adenosine triphosphate (*ATP*) reduction and adenosine diphosphate (*ADP*) increase. Under normal conditions, $I_{K(ATP)}$ remains inactive and is therefore not commonly incorporated in the baseline formulation of most cardiac models. For simulation studies of ischemia, an $I_{K(ATP)}$ current formulation was included in the ORd model (Dutta et al., 2017), as this current plays a major role in ischemia-induced APD shortening. A model for this current was developed by (Michailova et al., 2005), including dependencies on Mg^{2+}, *MgADP* and *MgATP* concentrations. In this thesis, I simplify Michailova's model by representing the dependency of the $I_{K(ATP)}$ current on the *ATP* concentration with the scaling factor $f_{K(ATP)}$:

$$I_{K(ATP)} = G_{K(ATP)} f_{K(ATP)} \left(\frac{[K^+]_0}{[K^+]_{0,normal}}\right)^{0.24} (V - E_K),$$

where $[K^+]_0$ is the extracellular potassium concentration, and $[K^+]_{0,normal}$ its value under control conditions; V is the membrane potential of the cell, E_K is the reversal potassium potential, $G_{K(ATP)}$ is the channel conductance described by Michailova with a value of 0.05 $mS.\mu F^{-1}$ and $f_{K(ATP)}$ represents a scaling value to define peak $I_{K(ATP)}$ conductance.

The original ORd model was additionally modified by changing the I_{Na} steady-state inactivation and recovery gates (h and j) to match the inactivation response from (ten Tusscher et al., 2004), as described in (Passini et al., 2016). This change was incorporated to overcome limitations from the original ORd model, namely increased PRR under ischemic conditions, as well as to allow electrical propagation with elevated $[K^+]_0$ (Dutta et al., 2017). Table 3.1 (original ORd) and Table 3.2 (modified ORd) show the changes included for the I_{Na} steady state inactivation and recovery gates.

3.6 Modelling cardiac tissue coupling and potential propagation

3.6.1 Bidomain equations

Computational modelling and simulation in cardiac electrophysiology is not limited to the reproduction of the ionic activity in cardiomyocytes. Thanks to the enormous technological advances during the last decades, it has been possible to couple many instances of cardiac models to reproduce whole organ function.

Original ORd formulation
$h_{\infty} = \frac{1}{1+\exp\left(\frac{V+82.9}{6.086}\right)}$
$h_{CaMK,\infty} = \frac{1}{1+\exp\left(\frac{V+89.1}{6.086}\right)}$
$\tau_{h,fast} = \frac{1}{1.432\cdot 10^{-5}\cdot\exp\left(\frac{-(V+1.196)}{6.285}\right)+6.149\cdot\exp\left(\frac{V+0.5096}{20.27}\right)}$
$\tau_{j} = 2.038+\frac{1}{0.02136\cdot\exp\left(\frac{-(V+100.6)}{8.281}\right)+0.3052\cdot\exp\left(\frac{V+0.9941}{38.45}\right)}$

Table 3.1. I_{Na} steady state inactivation and recovery gates (*h* and *j*) in the original ORd.

Baseline Model formulation
$h_{\infty} = \frac{1}{1+\exp\left(\frac{V+78.5}{6.22}\right)}$
$h_{CaMK,\infty} = \frac{1}{1+\exp\left(\frac{V+84.7}{6.22}\right)}$
$\tau_{h,fast} = \frac{1}{3.6860\cdot 10^{-6}\cdot\exp\left(\frac{-(V+3.8875)}{7.8579}\right)+16\cdot\exp\left(\frac{V-0.4963}{9.1843}\right)}$
$\tau_{j} = 4.8590+\frac{1}{0.8628\cdot\exp\left(\frac{-(V+116.7258)}{7.6005}\right)+1.1096\cdot\exp\left(\frac{V+6.2719}{9.0358}\right)}$

Table 3.2. I_{Na} steady state inactivation and recovery gates (*h* and *j*) in the modified ORd version.

The bidomain equations are used in the multiscale model to simulate electrical propagation in tissue. These consist of a set of partial differential equations (PDEs), describing the electrical potential in the intracellular and extracellular domains. Both domains are connected at each point in space through the cell membrane, represented by the cardiac AP model. The potential in both domains is assumed to be continuous in space and cells are connected to each other via gap junctions, allowing conduction between cells.

In the absence of an externally applied electric field, the bidomain equations used to describe electrical conduction in the ventricular and torso domains are given by

$$\nabla \cdot (\sigma_i \nabla \phi_i) = \beta \left(C_m \frac{\partial V}{\partial t} + I_{ion} \right) - I_{stim}, \quad in\ \Omega_h,$$
$$\nabla \cdot (\sigma_e \nabla \phi_e) = -\beta \left(C_m \frac{\partial V}{\partial t} + I_{ion} \right), \quad in\ \Omega_h,$$
$$\nabla \cdot (\sigma_t \nabla \phi_e) = 0, \quad in\ \Omega_t,$$

where Ω_h and Ω_t are the heart and torso domains; ϕ_i and ϕ_e (in mV) represent the intracellular and extracellular potentials, respectively; σ_i and σ_e (in mS·cm^{-1}) are the conductivity tensors associated to the ventricular intracellular and extracellular domains, and σ_{torso}, σ_{lungs}, σ_{bones} (in mS·cm^{-1}) the different tissue conductivities; β (set to 1400cm^{-1}) is the cellular membrane surface to volume ratio; and C_m (set to 1μF·cm^{-2}) is the cell membrane capacitance. In these equations, $V = \phi_i - \phi_e$ is the transmembrane potential. I_{ion} (in Am^{-2}) is the current resulting from ionic channels, pumps and exchangers, as obtained from the modified version of the ORd model (Dutta et al., 2017), and the stimulus current I_{stim} is imposed at each point of the endocardial surface by the activation sequence (Cardone-Noott et al., 2016), at physiological cycle length. The bidomain system of PDEs is closed with appropriate non-flux Neumann boundary conditions, representing conservation of current: $\vec{n} \cdot (\sigma_i \nabla \phi_i) = 0$ on $\partial\Omega_{\mathrm{h}}$, and $\vec{n} \cdot (\sigma_t \nabla \phi_e) = 0$ on $\partial\Omega_t \backslash \partial\Omega_h$, where $\partial\Omega_h$ is the ventricular surface, $\partial\Omega_{\mathrm{t}} \backslash \partial\Omega_{\mathrm{h}}$ is the external torso surface, and $\vec{n}$ is the normal vector to the domains. Given the algebraic relation between the transmembrane and intracellular and extracellular potentials, $V = \phi_i - \phi_e$, solving the bidomain equations reduces to solving two of these fields, namely V and ϕ_e. However, analytical solutions are in general not possible to obtain, unless very simplified geometries and ionic terms are considered. This motivates their numerical approximation by appropriate numerical techniques, such as the finite element method (FEM).

3.6.2 Finite element method (FEM)

Finite element method (FEM) and *Finite difference method* (FDM) are two extensively used numerical techniques for solving complex PDEs. FEM is used in industry based on its successful application in engineering domains, such as hydraulics, aerospatial, thermics or acoustics, despite requiring a higher computational cost. The use of FEM is extensively adopted in the field of simulation of cardiac electrophysiology (Niederer et al., 2011; Smith and Cohen, 1984).

In the simulations, the spatial domain is defined by an unstructured mesh discretised in nodes, typically by using tetrahedral elements. If V and ϕ_e are computed simultaneously, then at time $t_n = n \cdot dt$ it is possible to define a vector of unknown nodal values $\mathcal{V}^n = \{V^n;\ {\phi_e}^n\}$, where $n = \{1, 2, \dots\}$ and dt is the PDE discretisation time.

In general terms, the FEM then allows the resolution of the problem posed by the bidomain equations by formulating it as a system of linear equations $A\mathcal{V}^n = b$, to be solved at each timestep. Matrix A is calculated at the beginning and does not change if the domain is static and the PDE discretisation time remains constant. Vector b must be reassembled for each iteration using $\mathcal{V}^{n-1}$ and the ionic currents from the cardiomyocyte model. Therefore, ODEs in cell models must be resolved prior to the assembly of vector b.

Since the matrix A is positive and symmetric, conjugate gradients are a recommended option for solving the system of equations. Detailed information about the discretisation and resolution of the bidomain equations using FEM techniques can be found in the review published by (Pathmanathan et al., 2010).

3.6.3 Simulation software: Chaste

Chaste (Cancer, Heart and Soft Tissue Environment) was the software used for the simulations included in this thesis since cardiac modelling is one of its most extended applications. Chaste is a software package developed in the Computational Biology group at the Department of Computer Science, University of Oxford. Its aim is to solve complex, computationally-expensive and multi-scale problems in physiology and biology. It was programmed mainly on C++ using agile-programming techniques (Pitt-Francis et al., 2008). Chaste offers support for MPI and openMP and can be compiled either with Scons or CMake. It is supported by Linux and MacOS.

In Chaste, cellular AP models are incorporated into the tissue in CellML format (Lloyd et al., 2004), and posteriorly converted into C++ with PyCml during compilation (Cooper et al., 2011). The cardiac cell model (and the ODEs defining it) are integrated into the multiscale model by associating an instance of the ORd cell model with each heart mesh node. The ODEs are solved with CVODE, a variable-order, variable-step multi-step algorithm. In order to reduce the massive costs associated with solving such a large system of equations, Chaste incorporates the possibility of using preconditioners.

Output formats available in Chaste are HDF5, Meshalyzer, Cmgui and VTK. The latter option was the choice for this thesis due to its compatibility with the visualisation software Paraview. Time resolution of simulation output was defined as 1000 samples per second.

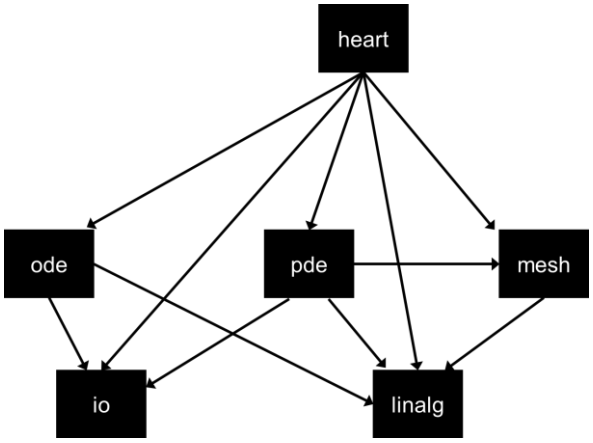


Figure 3.2. Dependencies of the cardiac electrophysiology simulation module with other code components.

Figure 3.2 describes the dependency of the cardiac simulation module with other components of the code:

- mesh: generates meshes from the data loaded. ParMETIS allows the partition of the mesh in distributed systems such as supercomputing facilities.
- io: reads mesh files, saves simulation results in different formats, and handles loading and saving checkpoints in the simulations.
- ode: computes the solution of ODEs using Sundials CVODE.
- pde: uses FEM to compute the PDEs defining the problem.
- linalg: iterative solutions of large sparse linear systems using PETSc.

Simulations were run in ARCHER (UK National Supercomputing facility) and MareNostrum4 (Barcelona Supercomputing Centre). A previous scalability study of Chaste showed almost optimal scalability of the software up to parallelisation in 1024 cores (Bernabeu et al., 2014). The performance analysis conducted for this thesis (see Figure 3.3) identified a remarkable speedup only up to 720/960 cores. The discrepancy observed in Chaste's scalability is likely due to the inclusion of the torso in the model. When the mesh is divided and assigned to the nodes, each partition might include torso

and heart nodes, leading to a significant load imbalance within the processes in a node and hence a negative effect on scalability. This optimisation of load imbalance is out of the scope of this thesis. Based on these results, most of the simulations were run on 720 or 960 cores. As a reference, 3 regular stimuli (CL = 600ms) simulated in a bidomain problem with a torso required approximately 6 hours on 720 cores.

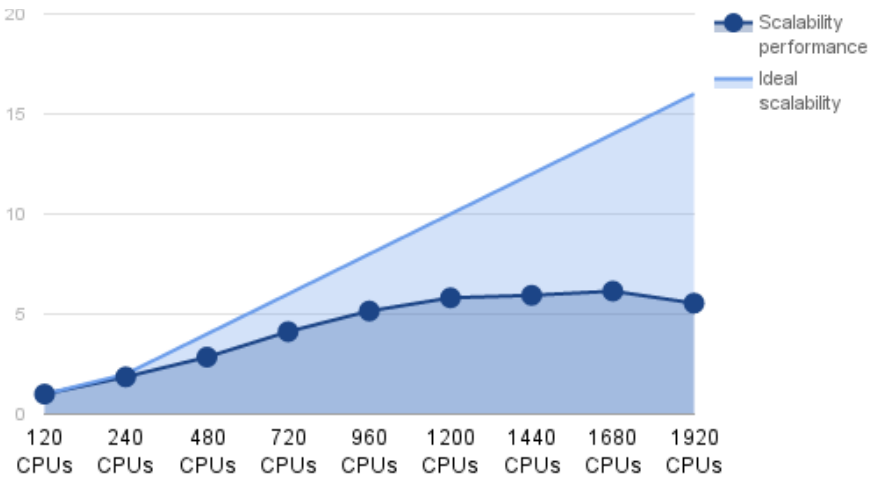


Figure 3.3. Chaste's scalability analysis for a bidomain simulation of cardiac electrophysiology. The simulation used as benchmark satisfies the spatial discretisation required by the convergence analysis described in the next section.

3.6.4 Convergence analysis

I created a computational benchmark, based on Chaste and inspired by (Niederer et al., 2011), to conduct a convergence analysis of the electrophysiology model. Different integration timesteps and mesh element sizes were tested on this benchmark to find the best compromise between computational cost and accuracy. The conductivity tensors in the intra- and extracellular domains are based on the values set by (Cardone-Noott et al., 2016), who used the tenTusscher-Panfilov cell model. These conductivity tensors using the ORd model were scaled by 1.8 to yield conduction velocity (CV) of 65 cm/s longitudinally, in agreement with experimental data reported by (Taggart et al., 2000).

A slab of myocardial tissue was defined as a regular mesh with dimensions 20×6×6mm with fibres aligned with its long axis. The stimulus region was shaped like a cube sized 1.5×1.5×1.5mm and located in a corner. CV was measured in the diagonal defined from the corner in which the stimulus was applied to the opposite corner. CVs were

calculated with different timesteps and size elements and posteriorly compared. As mentioned before, I used CVODE for numerical integration, for which Chaste documentation recommends using the same timestep for both ODE and PDE, since CVODE will take as many adaptive internal steps as required. I ran the benchmark with timesteps *dt* = 0.02 and 0.001ms for both ODE and PDE, and different mesh element sizes of *dx* = 0.5, 0.4, 0.3, 0.2 and 0.1mm. The results, displayed in Figure 3.4, identifies 0.04cm as a suitable mesh element size, with a discrepancy in CV lower than 5%. In addition, both timesteps of *dt* = 0.02 and 0.001ms produced very similar results when using CVODE.

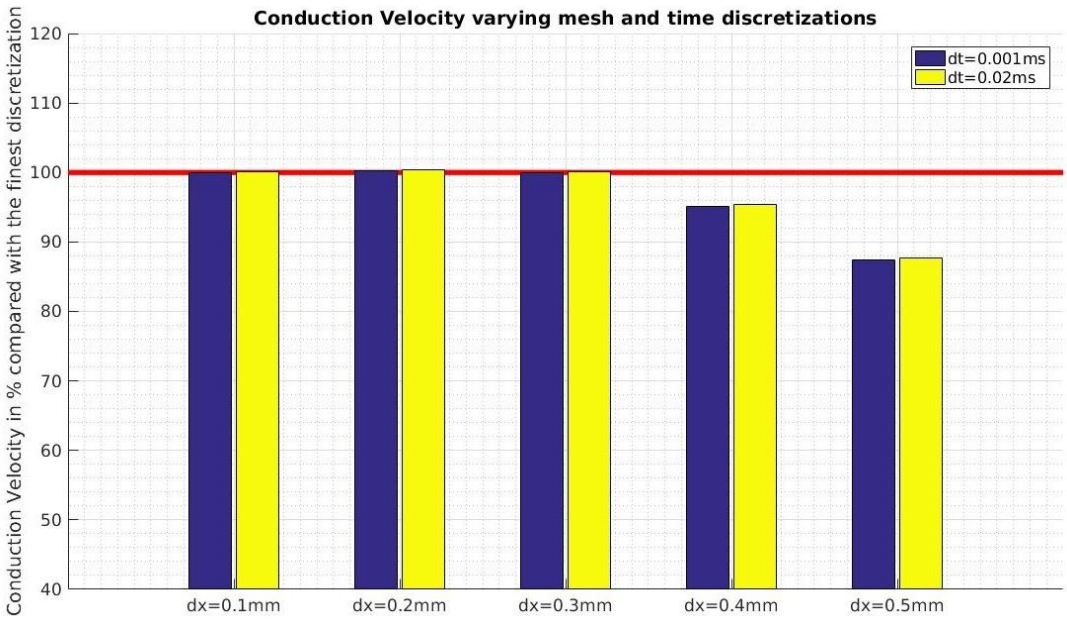


Figure 3.4. Convergence analysis for different time and space discretisations using CVODE in Chaste.

The time-adaptivity algorithm defined in class *PostUpstrokeTimeAdaptivityController*, included in Cardone-Noott's work, switches dynamically between a small and a large timesteps for solving ODEs and PDEs, with the purpose of decreasing computational costs. During cardiac tissue depolarisation, the class sets the small timestep for integration (*dt* = 0.02ms), which is replaced by the larger one (*dt* = 0.5ms) during the smoother repolarisation phase, preserving accuracy. This time-adaptivity controller was extended in this thesis to also activate a finer time discretisation when ectopic stimuli

and their subsequent wavefronts are established. Further details are provided in the Annex.

3.7 Simulating drug-induced effects on cardiac electrophysiology

Certain pharmacological agents, such as anti-arrhythmic and cancer drugs, are associated with changes in the ionic channels, which might affect arrhythmic risk. Experimental studies have investigated the effect of several drugs at varying doses on the different ionic channels in humans, see for example (Crumb et al., 2016; Kramer et al., 2013). For each drug-ion channel interaction, IC_{50} and Hill coefficient values were obtained. The IC_{50} value determines the drug dose required to produce a 50% block in a specific ion channel. The Hill coefficient (n_H) describes the steepness of the dose-response curve of the drug in the referred ion channel.

Based on the existing human experimental data, it is possible to calculate the changes produced by a certain drug on the ion channels at different doses. By incorporating into the simulations the resulting ion channel block, I was able to simulate the drug response at specific doses. In this thesis, drug effects have been incorporated into the simulations through the simple pore block model (Brennan et al., 2009), using the following equation:

$$\frac{I_i([D])}{I_i([0])} = \frac{1}{1 + ([D]/IC_{50})^{n_H}}$$

where $[D]$ represents the drug concentration modelled, $I_i([0])$ is the ion channel in control conditions, and $I_i([D])$ is the ion channel under the drug effects.

The single pore block model has been previously used to evaluate arrhythmic risk induced by potentially pro-arrhythmic drugs (Passini et al., 2017). The results showed a higher accuracy than animal experimental models in predicting drug-induced arrhythmic risk. However, a possible alternative to the simple pore block is the implementation of Markov models of drug action. This technique would allow representing in the model voltage and state-dependent binding to the ion channel proteins. Such complexity can be incorporated into each ion channel susceptible to be affected by drug effects, for all mesh nodes. Subsequently, the complexity of the model would increase substantially, further increasing the computational cost.

Conclusion

The starting point to build a simulation pipeline of cardiac electrophysiology covers the analysis of the computational methods used. In the convergency analysis, I consider different time and space discretisation configurations to find a balance between computational costs and accuracy. Even though simulations were run on national supercomputers, the large size of the problem requires a detailed study minimising computational costs due to the many simulations required. The next chapter provides a detailed description of the simulation framework constructed based on the techniques and technologies above-mentioned, and its evaluation with clinical and experimental data.

4 SIMULATION FRAMEWORK FOR HUMAN ACUTE MYOCARDIAL ISCHEMIA

In this chapter, I introduce the computational framework for modelling and simulation of human cardiac electrophysiology. It has been constructed, evaluated and posteriorly used for the studies comprehended in the present thesis. In the first section, I discuss the implementation of specific electrophysiological aspects in the model and its basis on experimental or clinical data. The second part of this chapter describes the computational pipeline used for running the computationally expensive simulations and the methods used for analysing the results obtained. Finally, the last section presents the evaluation of the model under healthy and ischemic conditions by comparing the results provided by the simulations with experimental and clinical data.

4.1 The human torso and ventricular model

To build a model that provides trustworthy and realistic results, it must reproduce structural and electrophysiological features observed clinically or experimentally. In this section, I present how these aspects have been implemented in the model and their basis on the literature. The simulation framework is based on a biventricular mesh embedded in a torso volume that takes into account different tissue types (Figure 4.1). Both meshes were obtained from computed tomography images and they consist of 3.25 million nodes and 19.4 million tetrahedral elements in total (Cardone-Noott et al., 2016). The average size of each element in the biventricular mesh is 0.4mm, as required

for convergence of the numerical algorithms (Bernabeu et al., 2010) and discussed in Section 3.6.4. The torso mesh has a coarser resolution than the ventricular mesh, as larger element sizes reduce computational time although the simulated ECG remains practically unchanged.

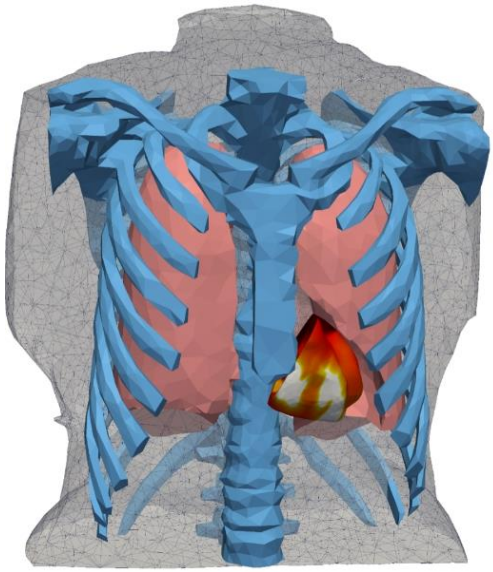


Figure 4.1. Torso/biventricular model used for constructing the simulation framework. Heterogeneities in tissue are represented by different regions defined for lungs, bones and heart, with distinct conductivity values.

4.2 Modelling of electrophysiological heterogeneities

Cardiac tissue is heterogeneous both in structure and electrophysiological features, as described in Section 2.4. Transmural heterogeneities in the electrophysiology of cardiomyocytes are caused by changes in mRNA and protein expression, affecting most of the ionic currents in the cell. Several studies have investigated those differences in human cardiomyocytes (Gaborit et al., 2007; Näbauer et al., 1996; Soltysinska et al., 2009; Szabó et al., 2005) and the data they reported on transmural differences in cardiomyocytes were used to construct the ORd human ventricle cardiomyocyte model (O'Hara et al., 2011) used in the simulations of this thesis (see Sections 3.4 and 3.5). Cardiomyocytes located near the epicardial surface have been shown to have different properties and behaviour compared to those located closer to the endocardium. AP duration, AP amplitude and maximum depolarisation velocity are significantly shorter in epicardial cells than in subendocardial (Näbauer et al., 1996; Szabó et al., 2005).

Figure 4.2 shows the differences in AP in epicardial, mid-myocardial and endocardial cardiomyocytes using the ORd model.

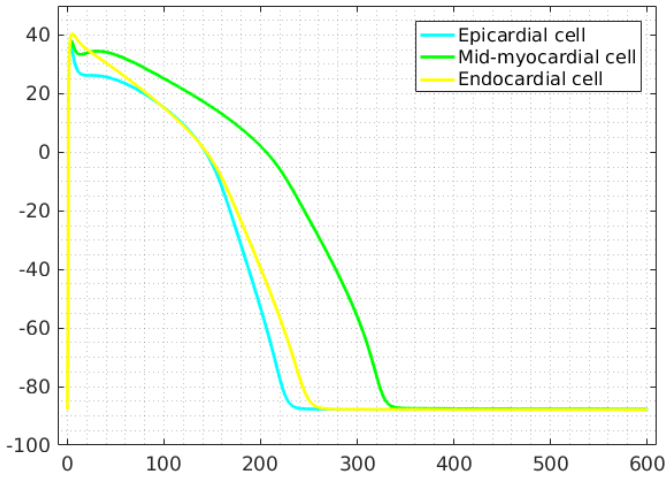


Figure 4.2. Simulated APs in epicardial, mid-myocardial and endocardial cells using the ORd model.

Additionally, apicobasal heterogeneities have been proven experimentally to be based primarily on changes in the delayed rectifier (I_{Ks}) and transient outward (I_{to}) potassium currents (Szentadrassy et al., 2005). Consequently, APD is shorter in human cardiomyocytes located in the apex than those located in the base. These heterogeneities were implemented in the model producing an APD 40ms shorter for cells in the apical versus the basal region (Brahmajothi et al., 1997; Burton and Cobbe, 2001), which plays a key role in the formation of T waves in the ECG (Weiss et al., 2007).

4.3 Modelling ischemia-induced electrophysiological changes

Arrhythmogenesis induced by acute regional myocardial ischemia is caused by electrophysiological changes in the affected tissue, constantly changing in time and location, as discussed in Section 2.5. Ischemia is tightly related to the formation of lethal reentrant patterns (Janse et al., 1980). The conditions reproduced in the simulations correspond to the first 10-15 minutes post-occlusion, considered particularly pro-arrhythmic (Carmeliet, 1999). The main electrophysiological changes induced by ischemia are triggered by the effects of hyperkalemia, acidosis and hypoxia. These abnormalities are included in the model at the ionic level and reproduce the most significant AP changes associated with ischemia, more extensively discussed in Section 2.5: a decrease of I_{Na} and I_{CaL} conductances, usually by 25% (Irisawa and Sato, 1986;

Kagiyama et al., 1982), an increase of extracellular potassium $[K^+]_0$ to 8-12 mM (Weiss and Shine, 1982, 1986) and the activation of $I_{K(ATP)}$ (Ferrero et al., 1996; Shaw and Rudy, 1997).

The set of parameters used for modelling ischemic cardiomyocytes (decrease of I_{Na} and I_{CaL} conductances by 25%, $[K^+]_0$ = 9.5mM; an increase of $I_{K(ATP)}$ conductance by 7%) were chosen based on the study conducted by (Dutta et al., 2017).

Variability in size, transmural extent and location of the ischemic region was included in the simulations. The location of the ischemic region is established by the occluded coronary artery, which causes poor blood irrigation in the affected tissue. I included in the simulations two ischemic locations: LCX occlusion, which causes damage in the LV free wall, and LAD occlusion, affecting mostly the anterior myocardial wall and the septum (Figure 4.3). Patients with LCX and LAD occlusion are linked to worse prognosis than RCA occlusion patients (Chen et al., 2011; Masci et al., 2011).

(Lee et al., 1981) reported infarct region sizes between 13 and 72% of the human LV. Transmural ischemic regions modelled in the experiments are inside that size range. Taking LCX occlusion as a reference, the large ischemic region represented ~40% of the LV as in (Dutta et al., 2016) (diameter of 6cm), whereas the smaller sized only ~14% (diameter of 3cm). The diameters of the large and small ischemic regions were maintained for LAD occlusion, although volumes changed since the septum was partially affected.

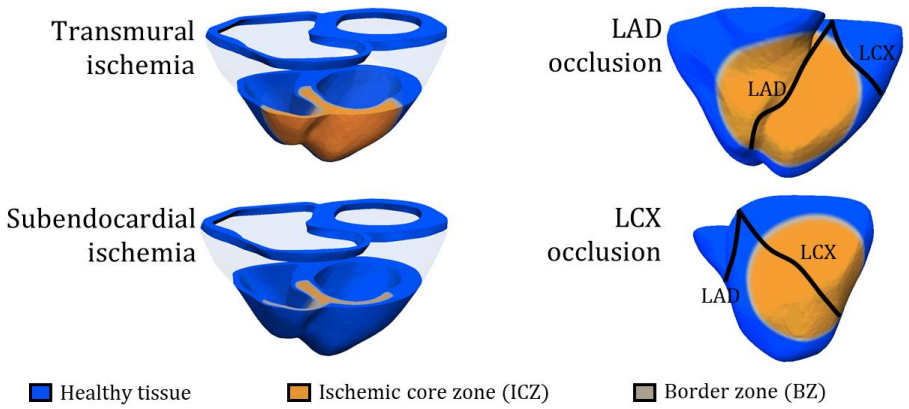


Figure 4.3. Modelling variability in the ischemic region. Left: transmural and subendocardial ischemia. Right: LAD and LCX occlusion.

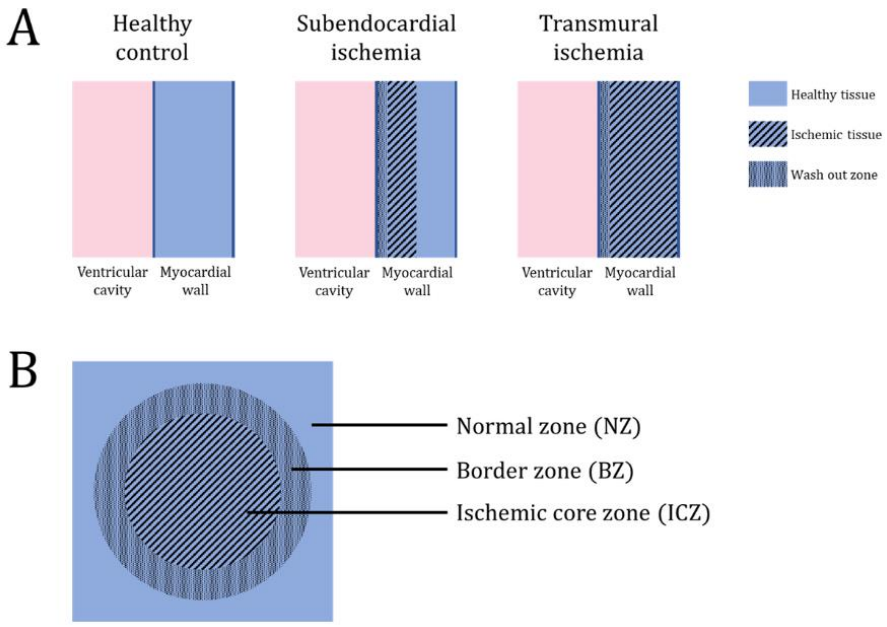


Figure 4.4. Modelling of the ischemic region. A: Modelling of transmural extent in ischemia, including a washout zone, also called subendocardial BZ. B: Modelling of the ischemic region (perspective parallel to epicardial plane). The ICZ is surrounded by an ischemic BZ, representing an electrophysiological gradient between healthy and ischemic tissue.

The transmural extent of ischemia is defined by the coronary stenosis degree. The tissue layer most affected by poor blood irrigation is the subendocardium (Colonna et al., 2000). In the simulations, I included transmural (full width of the myocardial wall) and subendocardial ischemia (only in the subendocardial region, 50% of the total extent of the myocardial width) (Figure 4.4, Panel A). The ischemic region was modelled as in (Dutta et al., 2016) (see Figure 4.4, Panel B) represented by the following regions:

- Ischemic core zone (ICZ). The ICZ is modelled with a spheroid defined in 3D space with Chaste. Tissue located within the spheroid is defined as ICZ. Electrophysiological abnormalities observed experimentally in ischemic cardiomyocytes are incorporated into them.
- Lateral border zone (BZ). The BZ surrounds the ICZ and is modelled as a 4mm wide region that represents the electrophysiological gradient between ischemic tissue and healthy myocardium, as reported in (Janse and Wit, 1989). The BZ is known to be a critical factor in ischemia-induced arrhythmogenesis due to electrotonic currents arisen in ischemia (Janse et al., 1980).

- Endocardial BZ (washout region). As described experimentally in (Coronel et al., 1991; Janse et al., 1980; Wilensky et al., 1986), a small rim of subendocardial tissue remains healthy between the ventricular cavity and the ischemic tissue. Nutrients and oxygen diffusion from the blood in the ventricles towards the subendocardial tissue facilitates the formation of the endocardial BZ. It has been incorporated into the model as a healthy tissue layer occupying 10% of the total myocardial width.

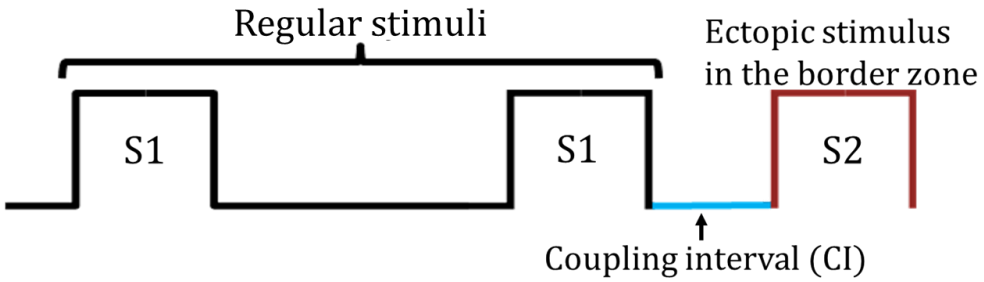


Figure 4.5. Quantification of arrhythmogenesis. Top: stimulation protocol for quantification of arrhythmogenesis. Bottom: representation of the results as a vulnerability window for reentry. Grey boxes represent coupling intervals in which the ectopic stimulus led to a reentry.

4.4 Stimulation protocol

Sinus rhythm was simulated by establishing a periodical activation sequence in the myocardium (S1). The activation sequence mimicking the trifascicular conduction system, initially presented in (Cardone-Noott et al., 2016), is started by seven initial activation points located on the endocardial tissue (4 in the LV, 3 in the RV). Then, the distance between every node located in the endocardium and its closest root activation node was computed using the Dijkstra algorithm (Dijkstra, 1959). The fast activation system was modelled by setting a stimulus in the subendocardium defined by a duration of 1ms and a magnitude of 120,000mA/cm^3. The activation time at each point of the subendocardium was computed as the result of the distance to the closest root activation node multiplied by the propagation speed measured in the left and right bundle branches connecting the atrioventricular node to the Purkinje fibres (1.4m/s). Mid-myocardium and epicardium were depolarised by the activation wavefront originated in the endocardium. The biventricular mesh was depolarised to its full extent in approximately 60 milliseconds, as indicated in experimental measurements (Durrer et al., 1970).

4.5 Quantification of arrhythmogenesis

A primary aim of this thesis is the quantification of arrhythmogenesis under the different acute myocardial ischemia scenarios. The protocol for arrhythmogenesis quantification is described as follows (see Figure 4.5, top panel).

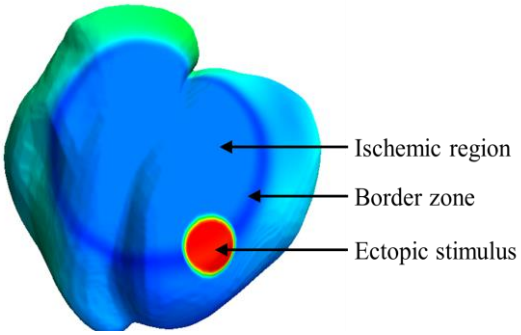


Figure 4.6. Modelling of ectopic stimuli in the ischemic BZ.

Initially, S1 activation was set in the model for 3 cycles, as described in the previous section. Then, an ectopic stimulus (S2) was established in the ischemic BZ (see Figure 4.6), in agreement with experiments (Coronel et al., 1995). The radius of the S2 focus was 1cm and covered partially the NZ and ICZ. The vulnerability window (VW) was defined as the set of coupling intervals in which an S2 stimulus triggers a reentry (Figure 4.5, bottom panel), and was computed for each ischemia scenario and S2 location. As the relative location of the ectopic stimulation in the ischemic BZ with respect to ventricular anatomy and ischemic region may influence the VW, I considered six S2 locations equally spaced around the BZ.

4.6 ECG simulation

To simulate the ECG signal, 10 nodes located on the torso surface were considered virtual electrodes (Figure 4.7) as presented in (Cardone-Noott et al., 2016). The 12-lead ECG was computed based on the extracellular potential values measured at these virtual leads. ECG calculation is described in the Annex, Section 0.

4.7 Structure of the simulation framework

The simulation framework is constructed primarily on the software Chaste, deployed in ARCHER (UK) and MareNostrum4 (Spain). The use of supercomputing resources was required for running the set of computationally expensive simulations comprehended in

this thesis and analysing the large volume of data obtained as results. Section 3.6 provides a detailed overview of the computational methods used in Chaste for calculate the simulations.

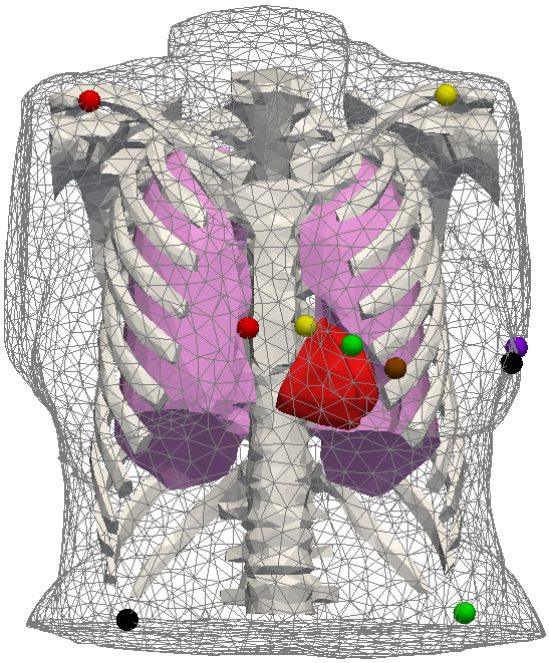


Figure 4.7. Visualisation of the combined heart-torso mesh. The coloured spheres indicate the location of the virtual electrodes, using standard (European) colour-coding. Reproduced from (Cardone-Noott et al., 2016) under open access license.

4.7.1 Software application for efficient execution of high-performance computing simulations of human cardiac electrophysiology

A flexible software application based on Chaste was required to run the multiple simulations required for this thesis. Its main features are described below:

1. Externalization of simulation parameters from the software application. In this way, code would not require to be recompiled before use.
2. Automatic output file system, assigning descriptive names to the directories containing simulation results.
3. Adaptation of certain classes created by other developers.

The structure of *GenericTest.hpp*, the main simulation code file, is the following:

a) Reading simulation parameters.
b) Definition of an input mesh and output format.
c) Definition of conductivities.

d) Additional output maps: upstroke velocity, APD...
e) Definition of apicobasal heterogeneities (*GenericVarier*).
f) Tissue generation (*GenericCvodeCellfactory*), defining:
    a. ionic blocks,
    b. apicobasal and transmural heterogeneities,
    c. Purkinje-like activation,
    d. Ischemia,
    e. cardiomyocyte model.
g) Loading simulation or starting a new one.
h) Definition of extracellular potential traces: location of the ECG leads.
i) Checkpoint for loading and saving the simulation status.

4.7.2 Setup and execution of simulations

A python script was created (*jobgen.py*) containing the set of options to be considered in the simulations plan. For example, the script written for the study on ischemia variability created the batch of files required for running multiple ischemia scenarios reproducing variability in:

a) Location of the ischemic region.
b) Size of the ischemic region.
c) Transmural extent of the ischemic region.
d) Location of the ectopic stimulus.
e) Normal or slow myocardial propagation.
f) Coupling interval (S1S2) in which the ectopic stimulus is set.

Each simulation requires a file describing its characteristics. Any of these files must be submitted into the supercomputer as a *job* for its computation. Each of the jobs requires to execute the program described in the previous section with specific parameters defined in the job file. An example of the source code of a job generator can be found in the Annex.

4.7.3 Data analysis

More than 800 multiscale simulations were run for the studies presented in this thesis. Each of them produced averagely 80GB of data as outputs, i.e. more than 64TB as

output data. Due to the large data volume, each of the simulation results was automatically processed for analysis, reducing significantly data transfers and post-processing in local machines. Post-processing of the simulations was based on the following procedures:

a) Extraction of extracellular potentials at the 12-lead ECG locations used to compute the ECG signal.
b) Graphical rendering of the voltage results using a Paraview script, a scientific visualization software. Typically, four different views considering 4 different camera perspectives were plotted for each time instant representing the cell membrane potentials *V* locally at each node by colours. The main purpose of this visualization is the creation of images and videos displaying the electrical activity of the human ventricles. This is crucial for the identification of arrhythmogenic patterns. The source code (test_paraview.py) can be found in the Annex.
c) For specific simulations, a reduced subset of consecutive frames including the voltage information at all mesh nodes was used to analyse membrane potential traces and posteriorly postprocessed in local machines for optimal intramural visualization. This technique was used to analyse reentrant patterns.

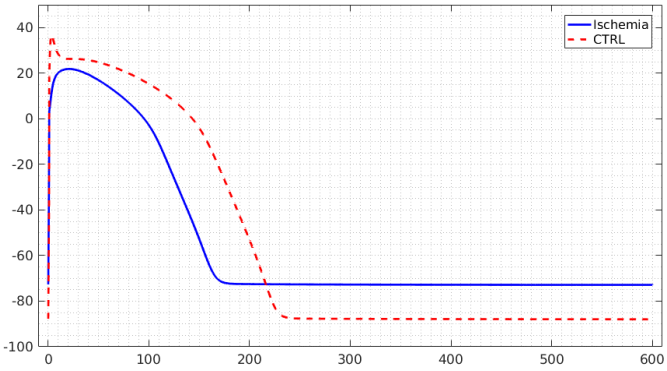
4.8 Validation of the simulation framework

4.8.1 Cellular electrophysiology

The ventricular cellular electrophysiology model is based on the human ventricular cardiomyocyte model by (O'Hara et al., 2011), which is extensively evaluated against experimental recordings (Carmeliet, 1999; Coronel et al., 1988; Sutton et al., 2000; Taggart et al., 2000). AP biomarkers were in agreement with the literature under both normal and ischemic conditions (Sutton et al., 2000; Taggart et al., 2000), as illustrated in Table 4.1 and previously discussed by (Dutta et al., 2017).

However, the integration of ORd model in the simulation framework required adjustments, since previous studies using the software Chaste were based on other human cardiomyocyte models (Luo and Rudy, 1994; Ten Tusscher and Panfilov, 2006). The computational simulation framework was validated using experimental and clinical

data at tissue and organ level, both under healthy and pathological conditions, in order to provide credibility to the simulations.



Cell model ORd modified as in Dutta et al. 2017, CL=600ms	APD90	Resting potential	ERP
Healthy	240 ms	-88 mV	231 ms
10 min post occlusion ($[K^+]_o$=9.5mM, $f_{K(ATP)}$=0.07, I_{Na} and I_{CaL} conductances 25% reduced)	169 ms	-73 mV	252 ms

Table 4.1. Changes in APD, resting potential and ERP after 10 min of acute myocardial ischemia using the modified ORd model version as described by (Dutta et al., 2017).

4.8.2 Myocardial propagation

Fibre orientation plays a key role in cardiac function and thereby must be introduced in the model. Electrical activity propagates preferentially along the fibre direction (longitudinal). Propagation along sheet direction (transversal) and along the sheet-normal dimension (transmural) is slower. In the computational model, conductivity tensors define electrical propagation across the longitudinal, transversal and transmural direction of every cardiomyocyte.

The conductivity tensors in the intra- and extracellular domains are based on the values set by (Cardone-Noott et al., 2016), who used the tenTusscher-Panfilov cell model. Conductance tensors using the ORd model were adjusted to yield a conduction velocity of 65 cm/s longitudinally, by default, in agreement with experimental data reported by (Taggart et al., 2000) for ischemic and healthy tissue, through scaling Cardone-Noott's values by 1.8.

Fibrosis (Coronel et al., 2005), diabetes (Nygren et al., 2007) or hypertrophy (McIntyre and Fry, 1997) are main risk factors potentially affecting cell coupling and consequently decreasing myocardial conduction. I modelled slow myocardial propagation scaling these conductivities by 0.83, subsequently reducing conduction velocities by approximately 25%. Table 4.2 displays conduction velocities measured under control and ischemic conditions for both normal and reduced myocardial propagation.

	Longitudinal	Transversal	Propagation
Healthy	64.5	30.5	Normal
	47.7	22.7	Slow
Ischemia	40	20.5	Normal
	32.4	15.8	Slow

Table 4.2. Conduction velocities measured in simulations of electrical propagation in myocardial tissue fibres along the longitudinal and transversal axis, under ischemic and healthy conditions and with normal and slow myocardial propagation. Units expressed in cm/s.

4.8.3 Quantification of ECG biomarkers

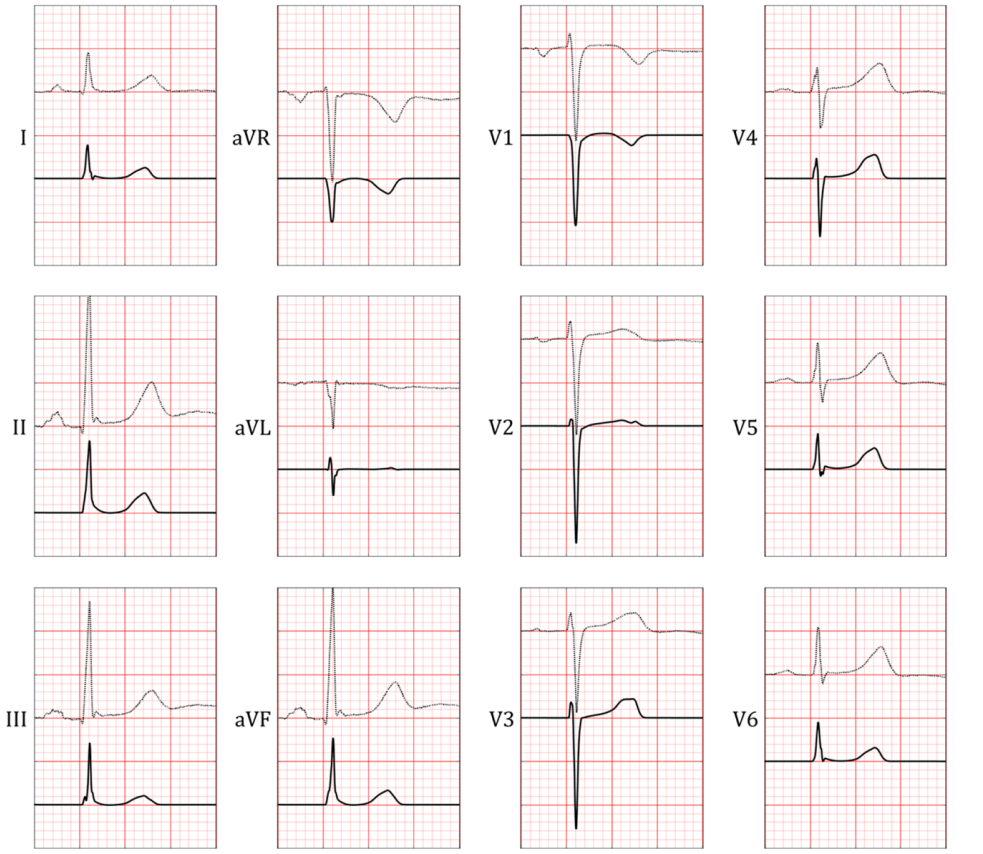
The relevant ECG biomarkers associated to ischemia were quantified in the simulated ECG signal.

ST deviation was computed as the voltage deviation from baseline 60ms after the J point as in other studies (Hasche et al., 1995; Mather (Editor), 2010). The J point was determined manually as the end of the QRS complex, where the high-frequency components of the QRS complex transition to the low-frequency ST segment. QRS width was measured on leads V1 and V2 as in other studies (Blackburn and Simonson, 1957).

For QT calculations, the end of the T wave was defined as the intersection of the descending slope of its terminal part with the isoelectric potential. The resulting QT intervals were then corrected for heart rate using the Bazett's formula.

Maximum QRS downslope (QRS_{DS}) was computed as by (Pueyo et al., 2008): after the point with the maximum slope is determined, a line is fitted in the ECG signal in windows of 15ms centred around the point. Special consideration was taken to exclude any notch in the R wave from the 15ms window used for the fitted line. Subsequently, certain cases were computed with smaller windows. The slope of the obtained line

would be the maximum QRS_{DS}. I define the change in the maximum QRS downslope (ΔQRS_{DS}) as the difference between the maximum QRS_{DS} value measured under ischemic conditions and the maximum value obtained in control conditions. I established that positive values in ΔQRS_{DS} indicate flatter QRS downslopes in comparison to the control scenario.



QRS width	QT interval	QTc interval	ST elevation
80 ms	325 ms	420 ms	0.032 mV

Figure 4.8. Comparison of simulated ECG (black solid line) under control healthy conditions, with the 12-lead ECG recording from subject 173 in the PTB database (light grey line). Table displays the main ECG biomarkers measured in the simulation under healthy conditions and normal myocardial propagation.

4.8.4 ECG in control conditions

As described in a previous study (Cardone-Noott et al., 2016), the endocardial activation model imposed to simulate sinus rhythm yields an activation sequence and a QRS complex in the 12-lead ECG, consistent with experimental and clinical recordings (Durrer et al., 1970; Ramanathan et al., 2006; Taccardi, 1963). In this thesis, I

demonstrate the agreement of simulated ECG with clinical ECGs recordings both under healthy (Bousseljot et al., 2009) and importantly under subendocardial and transmural ischemic conditions. I consider ST deviation (Jager et al., 2003; Laguna and Sörnmo, 2014) and variations in QRS downslopes (Pueyo et al., 2008; Ringborn et al., 2011) as main clinical markers of acute ischemia severity. Figure 4.8 represents the simulated ECG under healthy conditions compared with a representative healthy volunteer ECG recording (https://physionet.org PTB database, subject 173) (Goldberger et al., 2000). The adjacent table contains the main ECG biomarkers computed under control healthy conditions.

The resulting QRS width (80ms) falls within the clinical range of QRS duration for healthy male and female populations as reported by (Rijnbeek et al., 2014). Simulated electrophysiological dynamics are in agreement with reported activation sequences in human using microelectrode recordings, electromechanic wave imaging and electrocardiographic imaging (Cardone-Noott et al., 2016). The corrected QT interval (QTc = 420ms) showed agreement with the clinical ranges observed in healthy populations (Rijnbeek et al., 2014).

4.8.5 ECG in ischemic conditions

Introduction of acute regional ischemia in the human torso/biventricular model causes QRS alterations and ST deviations in agreement with clinical recordings for both transmural and subendocardial ischemia (Figure 4.9, panels A and B, respectively). ST elevation values obtained in simulated transmural ischemia (274 to 319µV, leads V2, V3 and V4; Figure 4.9, panel A) are within the range obtained clinically during coronary balloon LAD occlusion (200 to 500µV in leads V2, V3 and V4, Panel A, right) (Pettersson et al., 2000). Panel B confirms agreement between simulated and clinical ECGs under subendocardial ischemia, displaying mild ST depression (simulations: 28µV in lead V2; -6.3µV in lead V3; -25µV in lead V4) in range with maximal depression of up to -85µV in clinical transient ischemic ECGs (Jager et al., 2003). Thus, the consistency of simulation results with experimental and clinical recordings for ionic, cellular, tissue, whole-ventricular and ECG properties yields credibility to further findings.

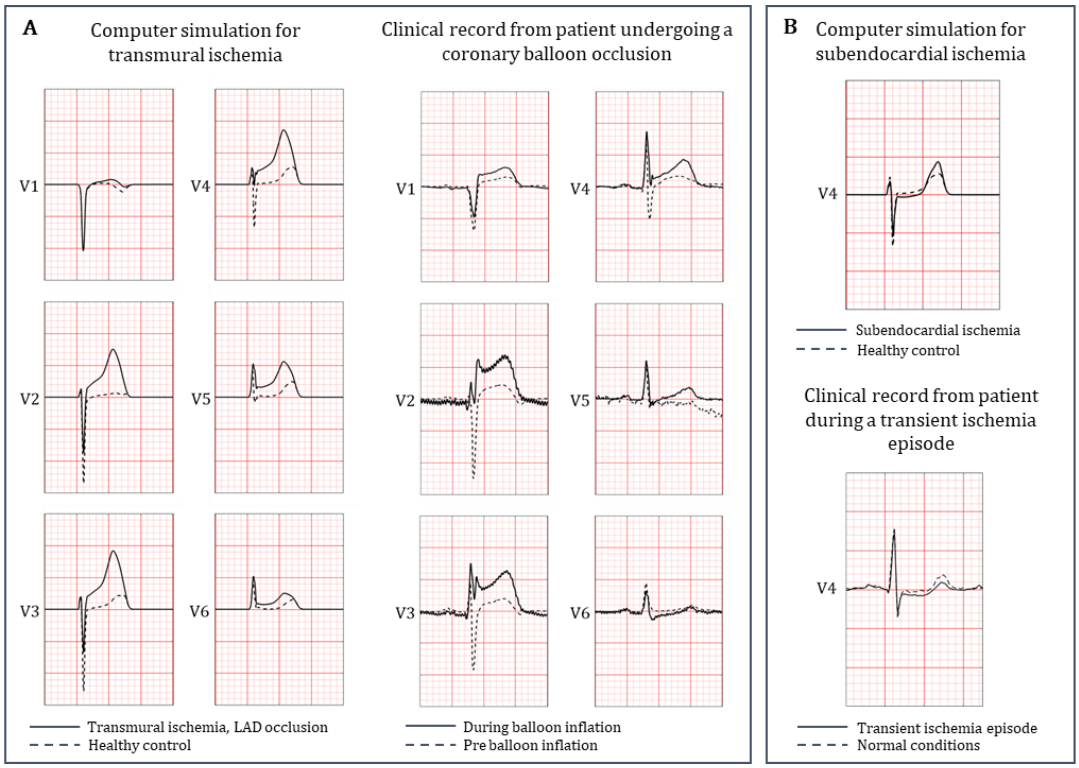


Figure 4.9. A: Comparison between simulated ECG signal in the precordial leads in transmural ischemia (left column, solid line) and clinical recording from a STAFF III database patient undergoing a LAD coronary balloon occlusion (right column, solid line). B: Comparison between simulated ECG signal in the precordial leads in subendocardial ischemia (top, solid line) and clinical ECG from the Long-Term ST Database during transient ischemia episode (bottom, solid line). Dashed lines for ECG in control/pre-ischemia.

Figure 4.10 analyses the mechanisms underlying ST abnormalities in acute regional ischemia for subendocardial ischemia (mild ST depression -9μV) and transmural ischemia (ST elevation of 319μV) compared to healthy ventricles. ST changes are due to resting potential elevation and AP shortening in the ischemic region compared to the remote region. The injury current, depicted with arrows, produces a deviation of the isoelectric level (above 0mV in subendocardial ischemia and below 0mV in transmural) and ST segment morphology abnormalities, as explained in Chapter 3 (Klabunde, 2011; Vincent et al., 1977).

The validation of the computational framework for modelling and simulating acute myocardial ischemia provides confidence to the results obtained. The next chapter unravels the mechanisms underlying how size, transmural extent and location of acute ischemia determine arrhythmia vulnerability and ECG abnormalities.

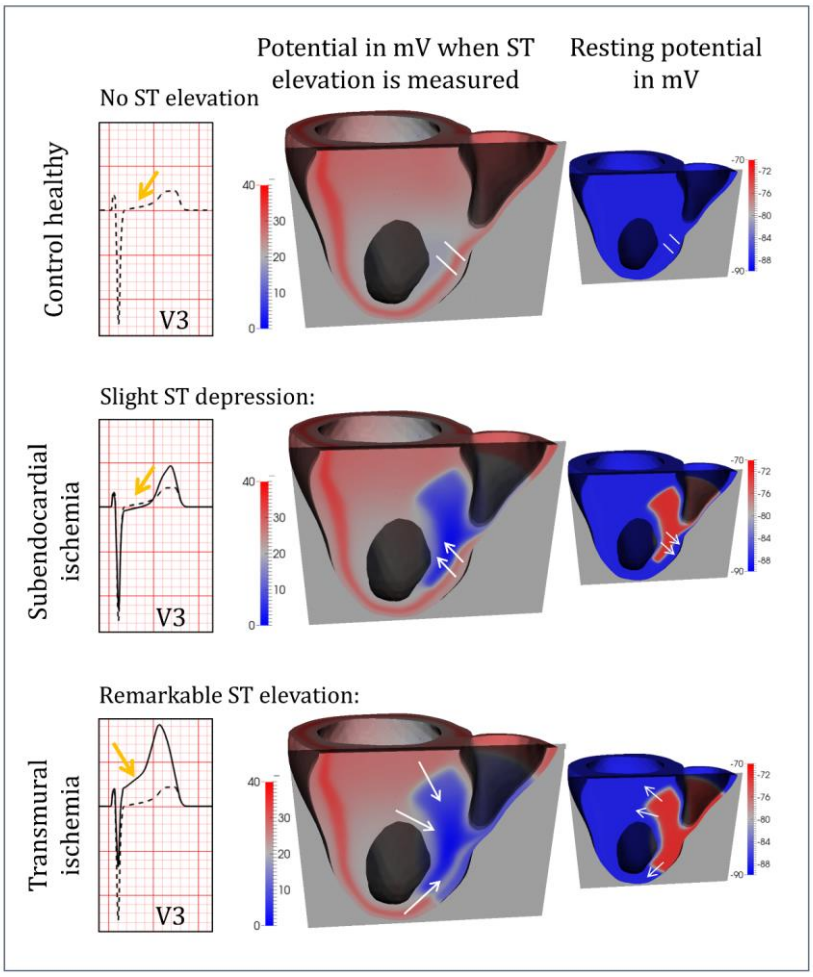


Figure 4.10. Analysis of the mechanisms producing the ST segment deviation displayed in the left column; centre column shows the heterogeneities in tissue during repolarisation due to ischemia; right column shows the heterogeneities in the resting potential leading to an ECG baseline shift.

5 HIGH ARRHYTHMIC RISK IN ANTERO-SEPTAL ACUTE MYOCARDIAL ISCHEMIA IS EXPLAINED BY INCREASED TRANSMURAL REENTRY OCCURRENCE

Acute myocardial ischemia is a precursor of SCD, as discussed in Section 2.6, but variability in its manifestation hampers the understanding of arrhythmia mechanisms and challenges risk stratification. The aim of this chapter is to unravel the mechanisms underlying how size, transmural extent and location of phase 1A acute myocardial ischemia determine arrhythmia vulnerability and ECG alterations.

5.1 Introduction

Acute myocardial ischemia is still one of the leading causes of SCD worldwide (Dagres and Hindricks, 2017). It arises from a mismatch between supply and consumption of oxygen and nutrients, and poor waste removal, often due to narrowing of a coronary artery.

One of the clinical challenges in the management of patients suffering from acute myocardial ischemia is its highly variable manifestation, as shown in Section 2.8, due to differences in location, extent and severity of affected myocardium. Some patients exhibit marked ECG abnormalities, and specifically ST elevation, whereas others suffer almost unnoticeable changes on their ECG (Herring and Paterson, 2006). It is also

unclear how ischemia-induced ECG abnormalities can be used effectively for arrhythmia risk stratification.

The first 10-15 minutes, or phase 1A, of acute myocardial ischemia are particularly pro-arrhythmic (Carmeliet, 1999) due to increased heterogeneity of repolarisation and conduction around the ischemic region in the human ventricles (Taggart et al., 2000). These electrophysiological heterogeneities, extensively studied in Section 2.5, establish the pro-arrhythmic substrate for reentrant waves (Janse et al., 1980), potentially breaking into ventricular fibrillation (Kannel et al., 1987; Madsen, 1985). As described in Chapter 3, computer simulations using human ventricular models have been able to reproduce existing knowledge on acute ischemia-induced electrophysiological alterations and the establishment of figure-of-eight reentrant dynamics around ischemic regions (Janse et al., 1980).

This study aims to investigate how the size, transmural extent and location of the ischemic region modulate pro-arrhythmic mechanisms of reentrant dynamics in the human ventricles. I hypothesize that macro-reentrant patterns (such as figure-of-eight) are more likely to occur around large and fully transmural ischemic regions, whereas subendocardial ischemia sustains transmural reentrant patterns, especially in the anatomically-complex septal region following LAD occlusion. This research question has not been addressed so far (Hundley et al., 2003; Kühl et al., 2015; Spach and Dolber, 1986; Wang et al., 2004), due to severe methodological challenges. Firstly, experiments in human whole-ventricles are challenging due to ethical and practical limitations, and the spatiotemporal dynamics of acute regional ischemia continuously change the substrate. Secondly, computationally, the investigations require multiscale anatomically-based human torso/ventricular models, which are very costly and require high-performance computing.

In this study, I exploit high resolution datasets obtained from high-performance computing simulations using a human torso/biventricular electrophysiology model, constructed and evaluated using extensive experimental and clinical data from ionic dynamics to the ECG. Electrophysiological changes in phase 1A acute myocardial ischemia are different from those observed in other stages post-occlusion, such as phase

1B ischemia or infarction, which have been the focus of previous investigations (Arevalo et al., 2013; Jie and Trayanova, 2010).

5.2 Methods

The computational framework described in Chapter 4 was exploited to systematically simulate electrophysiological activity from ionic dynamics to body surface potentials in human acute myocardial ischemia. Electrophysiological alterations in the ischemic region were modelled as specified in Section 4.3, including an ischemic core zone (ICZ), a lateral BZ and an endocardial BZ. Membrane dynamics were represented by the modified O'Hara-Rudy model, presented in Sections 3.4 and 3.5.

Electrophysiological effects of phase 1A acute ischemia, caused by hyperkalemia, hypoxia and acidosis were introduced to reproduce the heterogeneous changes in refractoriness and conduction velocity in human ischemic tissue (see Sections 2.5 and 4.3). In total, 18 scenarios were simulated, including 16 cases of acute regional ischemia corresponding to combinations of two different sizes, two transmural extents (subendocardial and transmural ischemia), and two locations (representing LCX and LAD occlusion, respectively), as shown in Figure 4.3. In addition, as acute ischemia often occurs in patients with a diseased cardiac substrate, we investigated the impact of slowed electrical propagation (by 25%) throughout the ventricles for all the aforementioned combinations.

The 12-lead ECG was calculated at standard clinical electrode positions on the torso, as discussed in Section 4.6. Measured biomarkers were obtained from simulated ECGs to validate the results with clinical records under healthy and ischemic conditions, as shown in Section a).

The stimulation protocol is discussed in Section 4.4. Sinus rhythm was simulated using a realistic activation sequence by applying endocardial stimulation for 3 beats (S1) with a cycle length of 600ms. To evaluate reentry vulnerability, ectopic stimulation (S2) was applied transmurally at the BZ. S2 was applied at varying coupling intervals (CI). For each CI, simulated electrical activity was analysed to identify reentry occurrence. The vulnerability window (VW) was quantified as the range of CIs for which S2 resulted in at least two reentrant cycles (see Section 4.5). As the relative location of the ectopic

stimulation in the ischemic BZ with respect to ventricular anatomy and ischemic region may influence the VW, I considered six S2 locations equally spaced around the BZ, providing sufficient coverage of its perimeter. By combining multiple scenarios, CIs and ectopic locations, I conducted a computationally-expensive study of more than 400 simulations of 3-11 hours each on 720 CPUs. Meshes, models, and example scripts to replicate simulation outputs can be found at:

[https://doi.org/10.5287/bodleian:9RxJPo9po].

5.3 Results

5.3.1 Impact of location, transmural extent and size of acute regional ischemia on ECG biomarkers

Figure 5.1 shows simulated ECGs for the 16 ischemic scenarios for leads V6 (LCX occlusion, cases A-H) and V3 (LAD occlusion, cases I-P), chosen due to the spatial proximity of those leads to the lateral and anterior myocardial walls, respectively. Values of ST deviation and variation in maximum QRS downslope (ΔQRS_{DS}) are provided. Overall, ECG alterations were more severe for LAD (Figure 5.1, right) than for LCX occlusion (Figure 5.1, left). Transmural ischemia caused marked ST elevation (Figure 5.1, A-D, I-L), whereas subendocardial ischemia primarily resulted in mild ST depression (Figure 5.1, E-H, M-P). Slow myocardial propagation (Figure 5.1, grey shade scenarios) mildly prolonged the QRS interval with negligible effects on the ST segment.

Figure 5.2 provides further quantification of ΔQRS_{DS} and ST deviation as a function of percentage of ischemic myocardium (top and bottom, respectively), for transmural (circles) and subendocardial (squares) ischemia. ΔQRS_{DS} positively correlates with the volume of ischemic myocardium for LAD occlusion (Figure 5.2, top right panel), but not for LCX occlusion (Figure 5.2, top left panel). For both LAD and LCX occlusion, ST elevation positively correlates with the size of the transmural ischemic region (circles, solid lines). However, subendocardial ischemia (squares) results in low or negligible ST depression in all cases regardless of location or size (dashed lines).

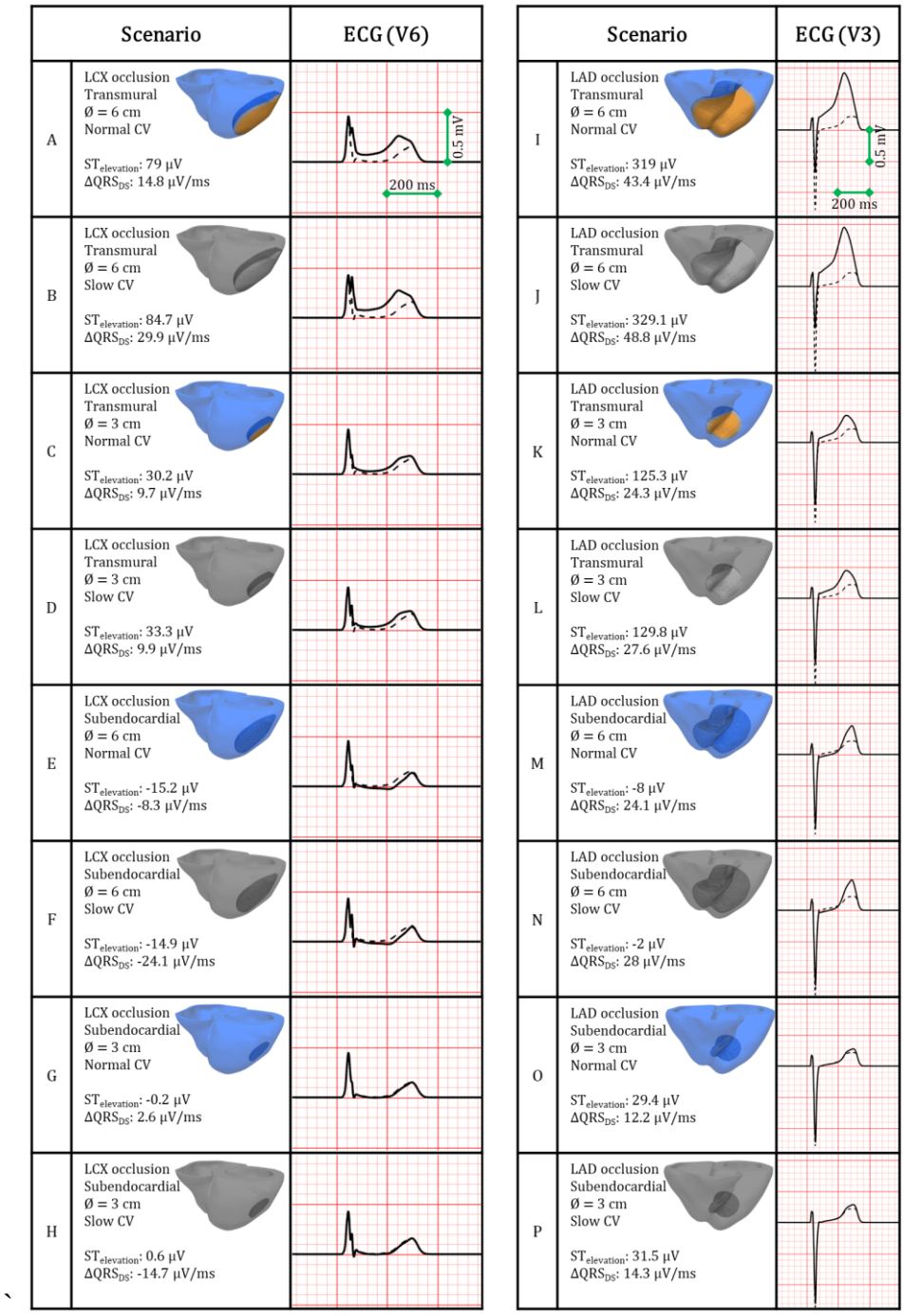


Figure 5.1. ECG alterations caused by acutely-ischemic regions, for LCX versus LAD occlusion (A-H and I-P, respectively), transmural (A-D and I-L) versus subendocardial (E-H and M-P) ischemia, small versus large ischemic region diameters (Ø=3 and 6cm, respectively), and normal versus reduced propagation in remote myocardium (full colour and grayscale, respectively). Dashed line indicates the ECG under control/pre-ischemia. Leads V6 for LCX and V3 for LAD occlusions are shown with ST deviation and change in maximum QRS downslope.

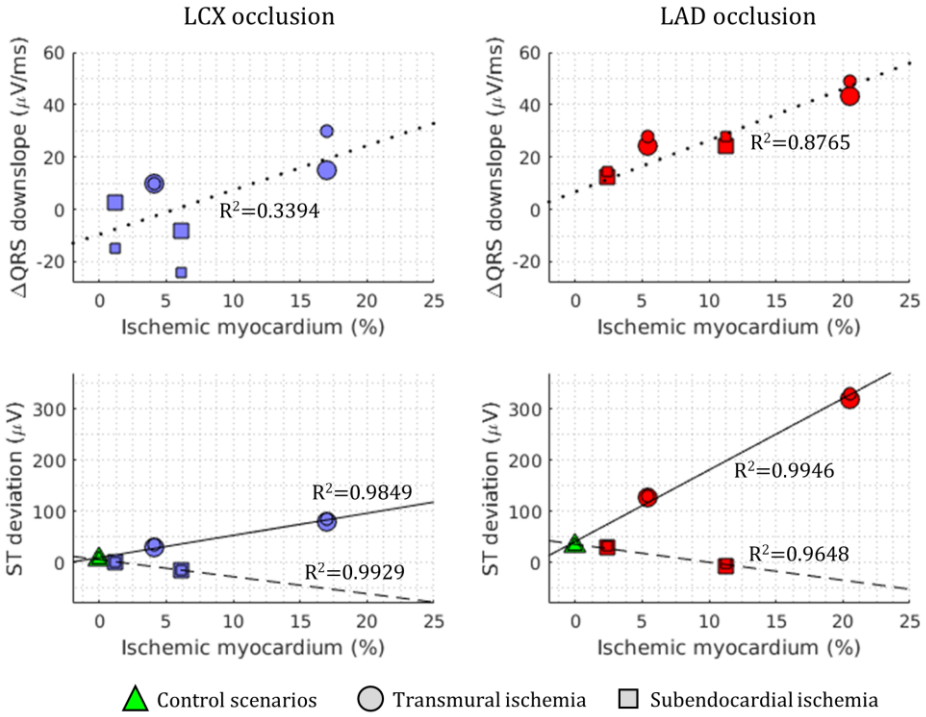


Figure 5.2. Ischemia-induced alterations in ECG biomarkers versus percentage of ischemic myocardium (top: change in maximum QRS downslope; bottom: ST segment deviation), for LCX occlusion (left column, blue scatter points) and LAD occlusion (right column, red scatter points). Coefficients of determination (R^2) are annotated for each biomarker. Smaller symbols correspond to slow propagation conditions.

5.3.2 Differences in wavelength for reentry explain the effect of ischemic region size and myocardial conduction velocity on arrhythmic risk

Figure 5.3 displays the results of the VWs obtained for the 16 different ischemia scenarios with premature stimulus S2 in the ischemic BZ in the LV mid-cavity for both LAD and LCX occlusion. No reentry was induced without ischemia with the same protocol. Consistent with the theory on reentrant circuits, slow myocardial propagation (as imposed in the grey-coloured cases in Figure 5.1 and Figure 5.3) facilitates reentry by reducing the wavelength of cardiac impulse (i.e. conduction velocity multiplied by refractory period). This is demonstrated in Figure 5.3 by the wider VWs reported in each grey-coloured scenario with slow conduction velocity versus their correspondent case with normal conduction velocity in the remote myocardium. Additionally, larger ICZ were always more arrhythmogenic than smaller ones (Figure 5.3).

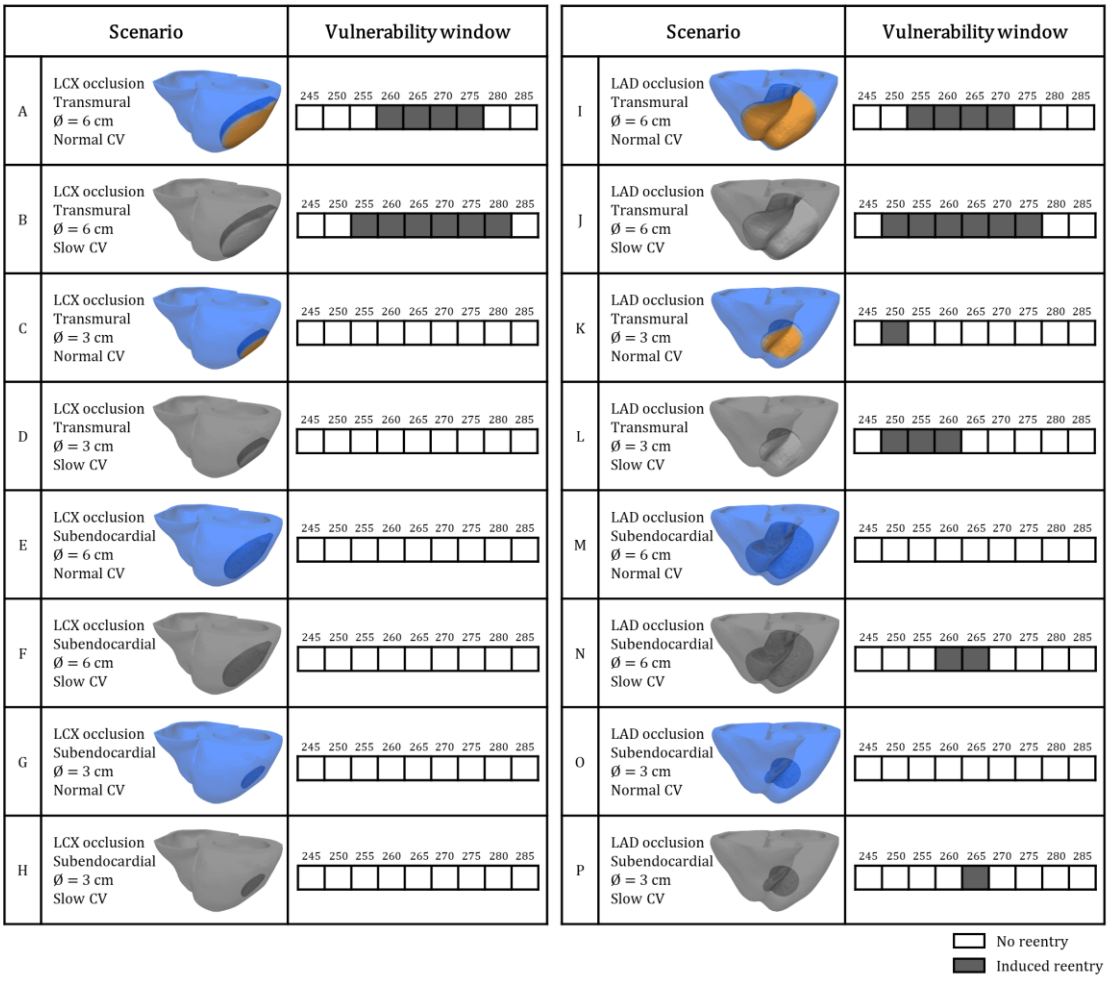


Figure 5.3. Vulnerability windows for reentry (dark grey boxes) in acute regional ischemia for LCX versus LAD occlusion (A-H and I-P, respectively), transmural (A-D and I-L) versus subendocardial (E-H and M-P) ischemia, small versus large ischemic region diameters, and normal versus reduced propagation in remote myocardium (full colour and grayscale, respectively). Ectopic stimulus applied at CI=245 to 285ms in ischemic BZ in LV mid-cavity (S2.b in Figure 5.5).

The mechanisms are illustrated in Figure 5.4, for large versus small ischemic regions (Figure 5.4A and B, respectively), and normal versus slow myocardial propagation for small ischemic regions (Figure 5.4B and C, respectively). In agreement with previous studies (Dutta et al., 2016; Janse et al., 1980), propagation following the ectopic stimulus is blocked in the still refractory ischemic region (red cross, 382ms), but circles around it towards the RV through base and apex (white arrows, 382ms). The larger pathway through the large ischemic region (Figure 5.4A) allows enough time, firstly, for ischemic tissue to recover and to allow retrograde propagation through the large

ischemic region (Figure 5.4A, 424ms), and secondly, for the normal tissue to recover once propagation has traversed the ischemic region, ensuring the continuation of the reentry (Figure 5.4A, 544ms).

In contrast, the small ischemic region (Figure 5.4B) does not allow enough time for the recovery of ischemic tissue, preventing retrograde propagation and leading to bidirectional conduction block (Figure 5.4B, 424ms), and no reentry is established (Figure 5.4B, 544ms). Reducing conduction velocity promotes the formation of reentrant circuits by delaying propagation around the ischemic region (Figure 5.4C, 382ms), allowing the recovery of the ischemic tissue and ensuring retrograde propagation and reentry (Figure 5.4C, 424, 544ms), even with small ischemic region.

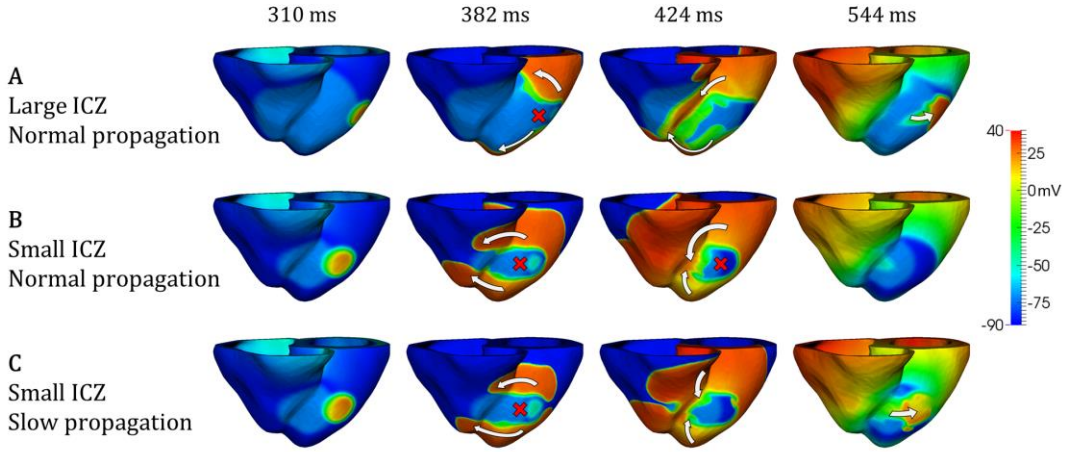


Figure 5.4. Effects of slow myocardial propagation and ischemic region size on macro-reentry formation. A: Figure-of-eight macro-reentry pattern induced around large transmural ischemic region in LAD occlusion. B: No reentry for small transmural ischemic region in LAD occlusion. C: Similar case as in B, but macro-reentry is enabled due to slow myocardial propagation. CI=260ms in all cases.

5.3.3 Arrhythmia vulnerability in subendorcardial LAD occlusion is explained by septo-apical transmural microreentrant pathways

I then investigated the mechanisms explaining how the effect of location and transmural extent of the ischemic region may modulate arrhythmic risk. I hypothesised that the intersection of the ischemic BZ with the septum, as in LAD occlusion, promotes the establishment of transmural micro-reentrant pathways. In the investigation of differences between LAD and LCX occlusion, the location of the ectopic stimulus with respect to the LV anatomy is likely to modulate arrhythmic risk. I therefore computed

the VWs for six different S2 locations around the BZ, for large transmural and subendocardial ischemic areas in LAD versus LCX occlusion (Figure 5.5). Overall, more reentries are induced in LAD versus LCX occlusion (54 versus 33 reentries for CIs=225-300ms), considering both transmural and subendocardial ischemia, for the conditions tested. Furthermore, more reentries are established in transmural versus subendocardial ischemia: 27 versus 6 reentries, respectively, in LCX occlusion, and 35 versus 19 reentries, respectively, in LAD occlusion (Figure 5.5).

Macro-reentry around the ischemic region, as described in Figure 5.4 and in previous studies (Dutta et al., 2016; Janse et al., 1980), was established in transmural ischemia, for both LCX and LAD occlusions and most S2 locations (Figure 5.5, light grey boxes).



Figure 5.5. Vulnerability windows for reentry for the most pro-arrhythmic conditions, in LAD versus LCX occlusion and transmural versus subendocardial ischemic region for 6 equally-spaced premature stimulus locations around the ischemic region. Macro-reentry (light grey boxes), transmural micro-reentry (dark grey boxes) and no reentry (white boxes) are indicated for CI=235 to 300ms.

As reported by (Janse et al., 1980), an additional mechanism consisting of transmural micro-reentry was identified (Figure 5.5, dark grey boxes), for both LAD and LCX occlusion. Even though transmural micro-reentries occurred both in transmural and subendocardial ischemia, they were the key mechanism explaining vulnerability to reentry in subendocardial ischemia (Figure 5.5).

Figure 5.6 demonstrates the differences in reentrant patterns in transmural versus subendocardial ischemia. As in Figure 5.4A and Figure 5.4C, Figure 5.6A illustrates the different stages of macro-reentry, with unidirectional conduction block in the ICZ, followed by propagation around the BZ (400ms), proceeding retrogradely into the ICZ (480ms) and finally reentering into the NZ (620ms). The reentrant wave continues (710ms), sustaining the macro-reentry around the ICZ. However, in subendocardial ischemia (Figure 5.6B), the epicardial view shows that the ectopic stimulus propagates through the ventricles (260 to 480ms), with subsequent recovery (620ms) until a breakthrough occurs (710ms).

In contrast, intramural dynamics are very different as shown in the transmural view through the septum in Figure 5.6C. Following the ectopic stimulus (260ms), propagation is blocked unidirectionally in the subendocardial ischemic region (400ms) but proceeds towards the base and also surrounds the ischemic region through the LV wall towards the apex (white arrows). Propagation continues to surround the BZ (480ms, 550ms), blocked in the ischemic region due to refractoriness (red cross), but reentering through normal tissue towards the apex (white arrows, 620ms). It is then that a spiral wave is established, anchored in the BZ in the septo-apical region (Figure 5.6 C, 620ms-802ms). Figure 5.6D demonstrates the existence of a stable I-type filament in the septo-apical region. Simulated electrocardiographic signal in lead V3 of the two reentries analysed in Figure 5.6A and Figure 5.6 B/C/D are shown in Panel E, associating macro reentries with larger wave amplitude than transmural micro-reentries (~1.3 versus ~0.5mV).

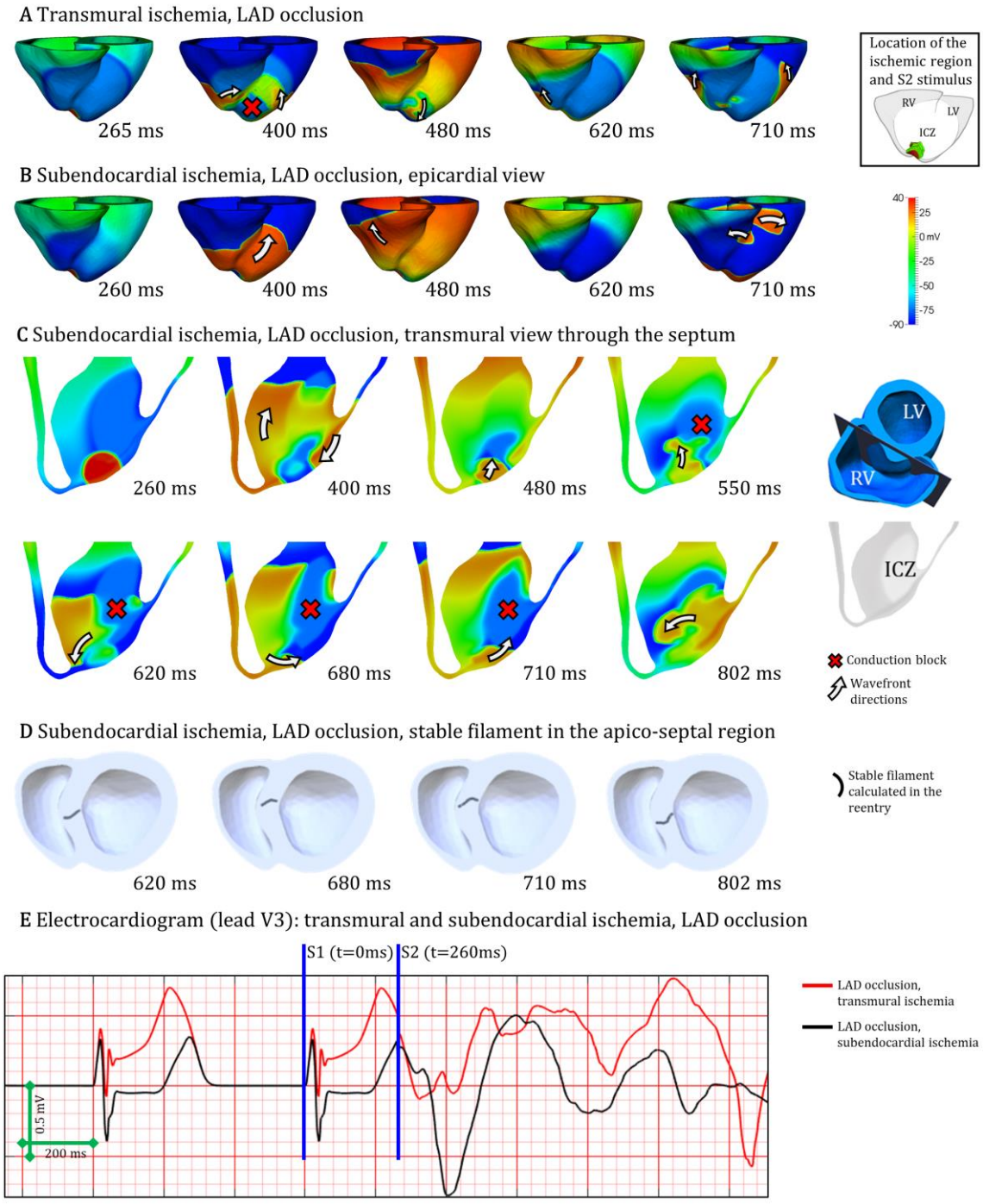


Figure 5.6. Two distinct mechanisms of reentry in acute regional ischemia. A: Macro-reentry in transmural ischemia by LAD occlusion. B: Transmural micro-reentry in subendocardial ischemia following LAD occlusion, epicardial view. C: Same case as B, transmural view through the septum displaying the reentrant circuit. D: Same case as B and C, visualization of the stable I-type filament located in the septo-apical region. E: ECG computed for both cases A and B/C/D. CI= 265 ms in A, CI = 260 ms in B/C/D.

The mechanisms underlying the smaller number of reentries in subendocardial versus transmural ischemia post-LCX occlusion are illustrated in Figure 5.7, panels A and B. Macro-reentry around the transmural ischemic region is established in Figure 5.7A, similarly to the patterns shown in Figure 5.6A. However, the subendocardial ischemic region is not able to sustain the conditions for reentry establishment, as shown in Figure 5.7B. Figure 5.7 C shows the ECG signal simulated in lead V6 for the cases displayed in Figure 5.7A and Figure 5.7B.

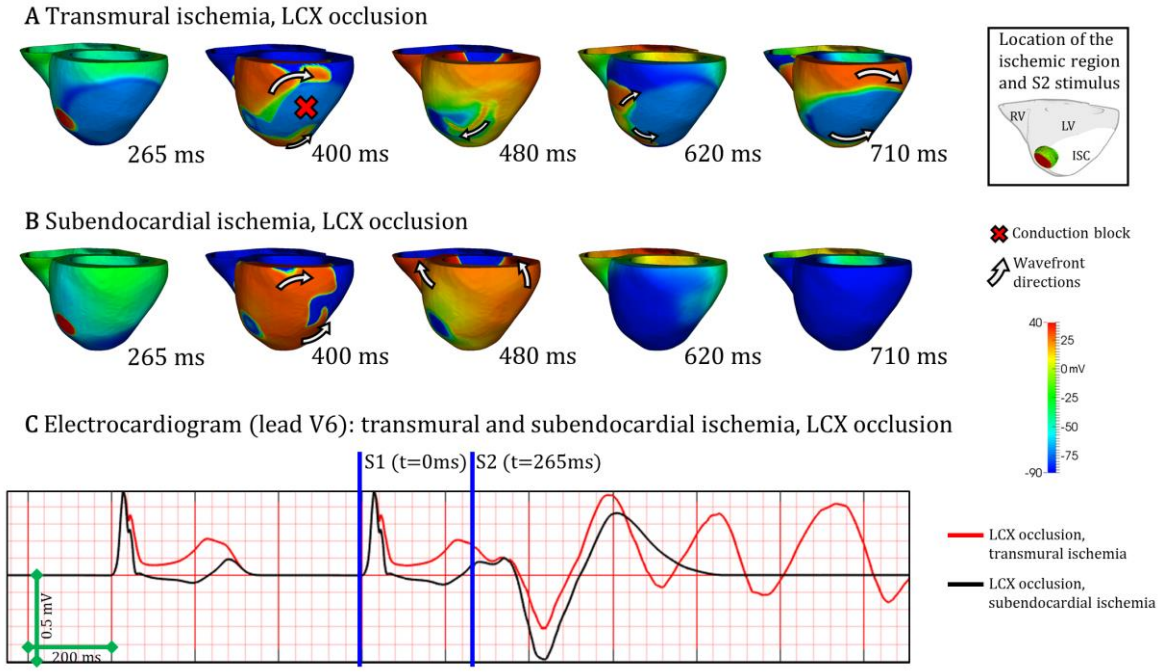


Figure 5.7. Reentrant mechanisms in LCX occlusion. A: Macro-reentry in transmural ischemia by LCX occlusion. B: No reentry in subendocardial ischemia by LCX occlusion. C: ECG computed for both cases A and B. CI= 265 ms in A and B.

5.4 Discussion

In this simulation study, the human ventricles affected by acute regional ischemia are shown to sustain two key types of reentrant patterns that determine differences in arrhythmic risk with varying ischemic region location, transmurality and size, using biophysical simulations on high-performance computing. Macro-reentry around the ischemic region occurs primarily for large fully-transmural ischemic regions leading to ST elevation, for both LAD and LCX occlusion. Large ischemic regions and slow myocardial propagation favoured the establishment of macro-reentries. Furthermore, transmural micro-reentry at the ischemic BZ was identified as critical to explain

arrhythmic risk, particularly for subendocardial ischemic regions, associated with mild ST depression.

The results also show a higher arrhythmic risk in LAD versus LCX post-occlusion for the conditions tested. The simulations reveal that this is due to a higher propensity for the establishment of transmural reentrant circuits at the intersection between the ischemic area and the septo-apical region in LAD occlusion, rather than in the LV free wall for LCX occlusion. Furthermore, simulations show that QRS downslopes may provide useful information on ischemic extent for subendocardial ischemia, whereas ST elevation serves as an indicator of size for fully-transmural ischemic region (Pueyo et al., 2008; Ringborn et al., 2011).

The credibility of the findings is supported by the consistency of the simulation results with experimental and clinical recordings at the different scales involved, as proposed by (Carusi et al., 2012). Firstly, ischemic tissue displays key electrophysiological alterations known to determine ECG biomarkers and reentrant patterns post-occlusion, and specifically prolonged post-repolarisation refractoriness and slow conduction velocity (Carmeliet, 1999; Coronel et al., 1988; Sutton et al., 2000; Taggart et al., 2000; Wilensky et al., 1986). This also includes electrophysiological gradients in the ischemic BZ, as in previous studies (Dutta et al., 2016; Tice et al., 2007; Trénor et al., 2005). Furthermore, the activation sequence used to simulate sinus rhythm has also been shown to be consistent with experimental recordings (Durrer et al., 1970). Finally, ECG patterns in control and in acute ischemia are in agreement with clinical 12-lead ECGs recordings (Bousseljot et al., 2009; Jager et al., 2003; Pettersson et al., 2000). This is both in terms of QRS complex progression between precordial leads (Figure 5.2) and ischemia-induced alterations in QRS slopes and ST elevation (Figure 5.1), shown to be in the range with values reported in clinical studies (Rijnbeek et al., 2014; Ringborn et al., 2011).

The simulations with the human ventricular acutely-ischemic model also reproduce the figure-of-eight reentrant patterns around the ischemic region, as reported experimentally by (Janse et al., 1980). These macro-reentries are favoured by large transmural ischemic regions, and their likelihood is explained by the wavelength for reentry. Simulations further reveal micro-reentries, also reported experimentally (Janse et al., 1980), which

are facilitated by slow intramural conduction close to the BZ. Whereas they can also coexist in transmural ischemia, micro-reentries are the only observed mechanism of reentry in subendocardial ischemia. Following LAD occlusion, the intersection of the BZ and the septo-apical region favours the establishment of micro-reentry by providing larger intramural pathways than in the LV free wall. The existence of two pro-arrhythmic mechanisms of reentry in acute ischemia determined by the transmurality and location of the ischemic region may offer opportunities for targeted anti-arrhythmic treatments.

Slow propagation in the remote myocardium had a substantial effect on arrhythmic risk in the simulations, even though with negligible ECG effects (Figure 5.1). Fibrosis (Coronel et al., 2005), diabetes (Nygren et al., 2007), or hypertrophy (McIntyre and Fry, 1997) are main risk factors potentially affecting cell coupling and consequently decreasing myocardial conduction, albeit with unclear ECG signature (Fronza et al., 2016). In the simulations, slow conduction promoted reentry in acute regional ischemia. This is in close correspondence with ex-vivo studies linking the occurrence of transmural reentries to conduction delays produced by fibrotic tissue (Nair et al., 2011). It could also explain that patients suffering from fibrosis as a consequence of pathologies like hypertrophic cardiomyopathy (Raphael et al., 2016) or diabetes mellitus (Becker et al., 2003) are at higher risk under ischemic conditions.

Moreover, subendocardial ischemia was associated with slight ST depression in the simulations, as in (Wilhelms et al., 2011), but also with high arrhythmia vulnerability, for LAD occlusion. The significance of potential risk predictors in silent myocardial ischemia remains an open discussion (Kléber, 2000; Park and Richard Conti, 2016). Significant ST elevation as the main clinical marker of acute ischemia severity (Kléber, 2000) was only correlated in the results with fully-transmural scenarios supporting macro-reentry (Figure 5.1). Conversely, changes in QRS downslope (Pueyo et al., 2008) accurately represented the proportion of affected tissue and arrhythmic risk for LAD occlusion.

5.5 Limitations of the study

The consequences of acute myocardial ischemia are complex and dynamic. In this study, I focus on simulating the electrophysiological consequences of the first 10

minutes post-occlusion on AP, refractoriness and conduction velocity to investigate ECG alterations and reentry vulnerability in one human ventricular anatomical model of phase 1A ischemia.

Variability in the shape of the ischemic region was excluded from the study for enabling comparisons between the different scenarios simulated, all of them presenting ischemic regions with identical circular shape. Furthermore, LAD occlusion was modelled by placing the ischemic region in the anterior myocardial wall, whilst in most LAD occlusion patients, the apex would be very often involved in addition to the anterior myocardial wall (Kobayashi and Maehara, 2019). RCA occlusions produce ischemia in the inferior myocardial wall, typically associated with a better prognosis than other coronary occlusions. This case was excluded from the study due to the additional complications associated, such as complete heart block and right ventricular infarction (Warner and Tivakaran, 2019).

The model was not intended to spontaneously generate triggering mechanisms of ectopic beats in the ischemic BZ. Instead, these were programmed arbitrarily as an additional stimulus region in the BZ with 1cm in diameter. This allowed the controlled calculation of the VW for each ischemia scenario by applying the ectopics at varying CIs. It is important to consider that simulations are undertaken in a static (non-contracting) ventricular model, and anatomical features such as endocardial trabeculations, papillary muscles and autonomic balance could play a role in reentrant pathways during ischemia (Bishop et al., 2010; Kalla et al., 2016; Kim Young-Hoon et al., 1999; Tomek et al., 2017). The study did not consider the role the Purkinje system may have during reentrant activity in acute ischemia. In addition to these factors, variability in cardiac anatomy, perfusion areas, ischemia severity, and baseline electrophysiological properties could also modulate arrhythmic risk (Boyne et al., 1997; Gemmell et al., 2016; Kral et al., 2012; Kujime et al., 2017). Building on the new insights provided by the study, further studies can investigate those additional factors.

5.6 Conclusion

In this study, I present a human torso/biventricular modelling and simulation study of the mechanisms of variability on arrhythmic risk and ECG biomarkers in acute regional

ischemia (phase 1A). The credibility of the simulation findings is supported by the consistency of simulated electrophysiological properties obtained with the human multiscale model with experimental and clinical recordings for ionic, cellular, tissue, and ECG properties. I identified transmural micro-reentries, in addition to the established macro-reentry around the ischemic region, as key pro-arrhythmic mechanisms in acute regional ischemia. Transmural acute ischemia (causing ST elevation) led to both macro- and micro-reentries, whereas arrhythmic risk in subendocardial ischemia (associated with mild ST depression) was predominantly explained by transmural micro-reentry. The modelling and simulation technology and results presented can inform the safety and efficacy evaluation of anti-arrhythmic therapy in acute myocardial ischemia. In the next chapter, I investigate the high arrhythmic risk derived from the interplay between acute myocardial ischemia and reduced sodium current availability in cardiomyocytes.

6 PRO-ARRHYTHMIC MECHANISMS INDUCED BY ACUTE MYOCARDIAL ISCHEMIA CO-EXISTING WITH SODIUM BLOCK ANALYSED THROUGH IN SILICO EXPERIMENTS

Although reducing sodium (Na^+) current availability is an effective therapy for atrial fibrillation by means of prolonging refractoriness in cardiac cells, clinical trials (such as CAST), have proven a high mortality associated with these drugs in ischemic patients (Echt et al., 1991). The aim of this chapter is to investigate the effects of reduced Na^+ channel availability on ischemia-induced arrhythmic risk and its underlying mechanisms.

6.1 Introduction

Myocardial ischemia is an important factor to consider in assessing arrhythmic risk in patients with additional pre-existing conditions such as channelopathies and in the evaluation of safety and efficacy of pharmacological therapy. As previously discussed in Section 2.9 and reported in the famous clinical trial CAST (Cardiac Arrhythmia Suppression Trial), Na^+ channel blockers have been shown to increase arrhythmic risk in patients with CAD. Understanding the functional interplay between Na^+ channel availability and myocardial ischemia is also fundamental to elucidate the pro-arrhythmic implications of CAD in patients suffering from channelopathies such as Brugada syndrome. These patients are often linked with SCN5A mutations (Deschênes et al.,

2000; Dumaine Robert et al., 1999; Frustaci et al., 2005; Veldkamp et al., 2000) and a decrease of the inward Na^+ current.

Huge advances in technologies and credibility of multiscale biophysical modelling and simulation have opened new avenues for the *in silico* evaluation of therapies and clinical conditions. *In silico* clinical trials are now proposed as a new paradigm shift, supported by industry and regulators, aiming at optimising and evaluating clinical therapies with computational approaches. As an example, a recent study has shown the higher accuracy of *in silico* trials compared to animal models in predicting drug-induced pro-arrhythmic risk (Passini et al., 2017). Furthermore, multiscale modelling and simulation have been used to investigate the electrophysiological consequences of ischemic regions on the ECG and arrhythmic risk, demonstrating excellent agreement with experimental and clinical recordings, as shown in Chapters 4 and 5, and other studies (Cardone-Noott et al., 2016; Dutta et al., 2016).

The aim of this study is to investigate the mechanisms of modulation of arrhythmic risk caused by reduced Na^+ current availability in the human ventricles affected by acute regional ischemia. I hypothesise that reduced Na^+ current availability increases arrhythmic risk by promoting conduction block and reentry formation due to increased dispersion of refractoriness across the ischemic BZ. The higher occurrence of ischemia-induced reentries under low Na^+ current availability could explain the high mortality observed in clinical studies of Na^+ channel blockers in ischemic patients (Anderson et al., 1994; Echt et al., 1991). Additionally, I aim to unravel how the location of ectopies could affect the formation of arrhythmogenic mechanisms under these conditions.

6.2 Methods

6.2.1 Calculation of electrophysiological biomarkers in 1D fibres under baseline and ischemic conditions

A set of one-dimensional (1D) monodomain fibres was designed with the purpose of measuring the electrophysiological biomarkers under varying ionic conditions under control and ischemic conditions. 1D fibres were based on 100 elements and 2cm long, featuring transmural heterogeneity of 80% endocardium and 20% epicardium. Stimulus current was applied to the first 3% of the fibre, and conductivity was set to 0.663mS/cm to yield a realistic conduction velocity in humans. Ischemic conditions (described in

Section 4.3) were introduced to the transmural fibres. Transitions between the central ischemic and normal zones were defined as gradients: increase in extracellular potassium level was faster in endocardium than in epicardium, while activation of $I_{K(ATP)}$ was linear in the ischaemic region from endocardium to epicardium (Tice et al., 2007). The 1D fibres were paced under an S1-S2 protocol: regular stimulus was applied with a cycle length of 1000ms for 20 beats, and then an ectopic stimulus at progressively shorter CIs was set after the S1, with 10ms precision. APD, ERP and CV were measured for each case.

6.2.2 Alterations in Na^+ current availability for simulating channelopathies and drug-induced Na^+ channel block

In this study I analyse the effects of Na^+ current alterations in the formation of ischemia-induced arrhythmias. I consider two main scenarios. The first one is a severe reduction of the Na^+ current conductance with respect to baseline, which has been shown to occur in patients presenting SCN5A mutations (Meregalli et al., 2005; Remme, 2013) and I characterised in the model with a 50% reduction of I_{Na}. The second scenario is a 25% reduction of the Na^+ current conductance with respect to baseline, which would represent drug-induced block. This degree of current block is estimated from a single pore-block model (Brennan et al., 2009), using the IC_{50} and N_H values for each drug-channel interaction extracted from (Crumb et al., 2016), as described in Section 3.7.

Drug	IC_{50} (nM)	N_H	EFTPCmax (nM)	Ionic block at $EFTPC_{max}$	Ionic block at 3x $EFTPC_{max}$	Ionic block at 5x $EFTPC_{max}$
Flecainide	6677	1.9	752.9	1.6%	11.4%	25.2%
Propafenone	3886	0.9	131.0	4.1%	10.6%	16.8%
Quinine	24151	1.1	3956.7	11.8%	31.2%	44.5%

Table 6.1. Ionic channel block values computed for selected channel blockers at different doses: 1, 3 and 5 times the maximum effective free therapeutic plasma concentration EFTPCmax. IC50 and NH values for the different pharmacological compounds are extracted from (Crumb et al., 2016).

Table 6.1 shows the effects of the selected drugs on the Na^+ channel at different doses: 1, 3 and 5 times the maximum effective free therapeutic plasma concentration $EFTPC_{max}$. Based on the values shown in Table 6.1, and especially flecainide, as related

to the CAST trials, 25% Na^+ block was chosen to evaluate arrhythmic risk derived from a drug-induced moderate sodium blockage.

Thus, 25% and 50% Na^+ block were established as representative ionic alterations for investigating the pro-arrhythmic effects of Na^+ blockers and channelopathies derived from SCN5A mutations, respectively. Additionally, a 25% Na^+ channel increase was considered in the experiments to represent gene therapies, as seen in (Lau et al., 2009). In total, 3 scenarios were simulated with varying ionic alterations, as shown in Table 6.2.

Scenario	Ischemia	Implementation	Simulated effects
BASELINE	LAD occlusion	ORd model (baseline)	Acute myocardial ischemia
50% Na^+ block	LAD occlusion	ORd model with 50% reduction of the I_{Na} conductance	Acute myocardial ischemia + SCN5A mutations, such as BrS or Lenègre's disease
25% Na^+ block	LAD occlusion	ORd model with 25% reduction of the I_{Na} conductance	Acute myocardial ischemia + Na^+ channel blockers, such as flecanide or encanide
25% Na^+ increase	LAD occlusion	ORd model with 25% increase of the I_{Na} conductance	Acute myocardial ischemia + Gene therapy, such as SkM1 overexpression

Table 6.2. Scenarios designed for evaluation of the electrophysiological consequences of ionic alterations (3rd column) in acute myocardial ischemia caused by pharmacological and gene therapy.

6.2.3 Simulation of Na^+ current block using the computational framework

The computational framework described in Chapter 4 was exploited to simulate electrophysiological activity from ionic dynamics to body surface potentials in human acute myocardial ischemia under diverse Na^+ current availability conditions. The 12-lead ECG signal was computed at clinical electrode positions on the torso (see Section 4.6). The validation of the model has been previously described in Section 4.8.

Based on the results of Chapter 5, transmural ischemia following LAD occlusion was the chosen scenario to conduct the simulations included in this chapter, based on the high propensity to the formation of reentries. Electrophysiological changes in the ischemic region were modelled as described in Section 4.3, defining an ischemic core zone, a lateral BZ and an endocardial BZ. Membrane dynamics were represented by the modified O'Hara-Rudy model, presented in Sections 3.4 and 3.5. Electrophysiological

effects of phase 1A acute ischemia, caused by hyperkalemia, hypoxia and acidosis were introduced to reproduce the heterogeneous changes in refractoriness and conduction velocity in human ischemic tissue (see Sections 2.5 and 4.3). As previously mentioned, regular pacing was simulated using a realistic activation sequence by applying endocardial stimulation (Cardone-Noott et al., 2016) for three regular stimuli with a cycle length of 1000ms. VWs for reentry were evaluated on each scenario (Table 6.2) by applying transmurally ectopic stimulation at the BZ of the ischemic region at varying coupling intervals (CI). For each CI, the simulated electrical activation was analysed to study the formation of reentrant circuits. Six different S2 locations were considered for each scenario, equally spaced around the ischemic BZ. In total, more than 400 simulations of 5-15 hours each on 720 CPUs were conducted.

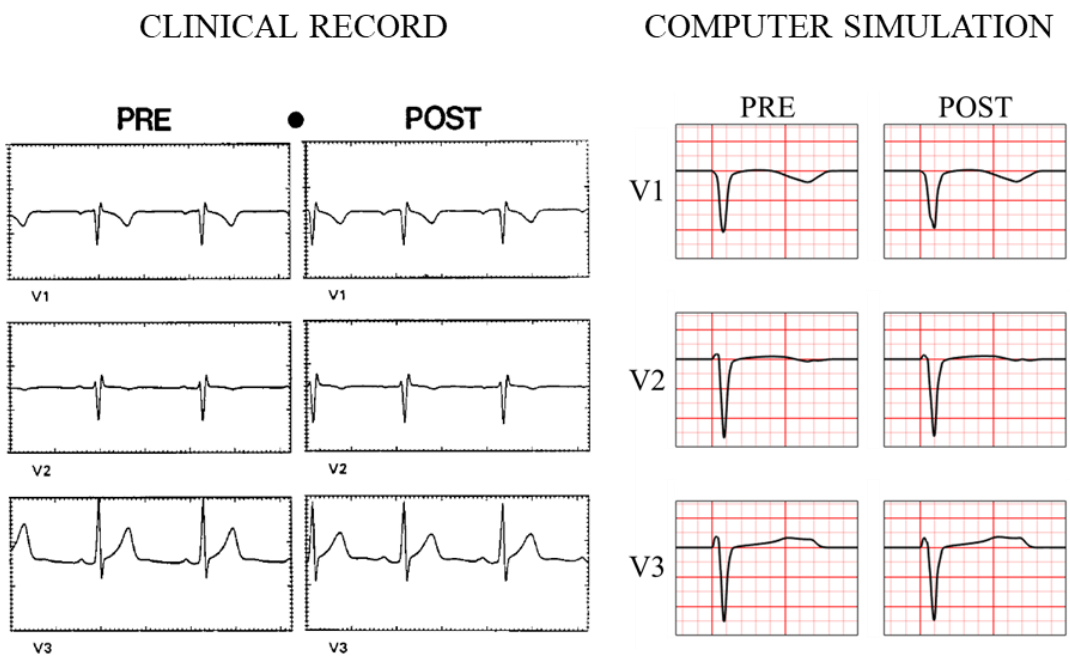


Figure 6.1. Comparison of simulated ECG under Na^+ block conditions with ECG recordings from healthy patients administrated of ajmaline (Na^+ blocker). Left: electrocardiographic leads V1, V2, and V3 from a control healthy patient before (PRE) and after (POST) administration of single intravenous dose of 1mg/kg ajmaline, a Na^+ blocker used for identifying Brugada syndrome. Reproduced from (Brugada et al., 2000). Right: Simulated electrocardiographic signal from leads V1, V2 and V3 under healthy (non-ischemic) baseline ionic conditions (PRE) and with 25% block in the Na^+ current (POST) simulating the effects of Na^+ blockers on the ECG. Note that both in the ECG recording and the simulation, ECG changes caused by Na^+ block are minor.

Changes in the Na^+ current were applied globally, affecting the whole myocardium. Figure 6.1 compares the effects of Na^+ block on the ECG under normal healthy circumstances, which are negligible. The left panel shows ECG leads V1 to V3 from a healthy patient before (*PRE*) and after (*POST*) administration of ajmaline, a Na^+ blocker used to identify Brugada syndrome patients. The right panel displays the simulated ECG signals produced for this thesis under healthy non-ischemic conditions. In the *PRE* column, baseline ionic conditions were simulated, whereas in the *POST* column 25% block was implemented in the Na^+ current. Both in the clinical record and the simulation, ECG changes derived by Na^+ block are minor under normal circumstances.

6.3 Results

6.3.1 Na^+ current block reduces moderately myocardial conduction velocity but increases significantly refractoriness dispersion

Table 6.3 shows how electrophysiological parameters vary in healthy non-ischemic tissue with changes in Na^+ current availability. Na^+ channel block reduced myocardial propagation ($CV_{Baseline}$ = 75cm/s, $CV_{50\%Na+Block}$ = 60cm/s) and increased refractoriness dispersion between healthy and ischemic tissue ($\Delta ERP_{50\%Na+Block}$ = 330ms), which is associated with a higher likelihood in the development of arrhythmias. Increased sodium current reduced refractoriness dispersion between healthy and ischemic tissue ($\Delta ERP_{Baseline}$ = 50ms, $\Delta ERP_{25\%Na+Increase}$ = 20ms).

Scenario	APD (ms)	CV (cm/s)	ΔERP (ms)
Baseline	240 (169)	75 (42.9)	50
50% Na^+ block	239 (178)	60 (30.8)	330
25% Na^+ block	241 (170)	66.7 (37.5)	140
25% Na^+ increase	239 (167)	75 (48)	20

Table 6.3. Measurement of electrophysiological biomarkers under varying Na^+ current conditions, measured in 1D fibres based on the O'Hara-Rudy model. APD and CV are measured under control and ischemic conditions, the latter presented in brackets. Refractoriness dispersion (ΔERP) is measured as the difference between refractory periods in ischemic and healthy cells. 1D fibres were stimulated with a frequency of 1Hz. The 1D fibre simulations and measurements were conducted by Dr Xin Zhou.

Changes in Na^+ channel availability altered mildly APD both under healthy and ischemic conditions (Table 6.3, left column). The CV reduction caused by ischemia is particularly severe in case of Na^+ block, leading to reduced CV values between 30 and 40cm/s, values 50% lower than measured in non-ischemic tissue.

6.3.2 The asymmetric biventricular anatomy explains differences in ischemia-induced reentrant mechanisms

Varying the location of the ectopic stimulus around the ischemic region leads to differences in VW width and type of reentry established, as shown in Figure 6.2. The most pro-arrhythmic ectopic locations is septum/apex (case C), followed by LV (cases A and B), RV mid-wall (case D) and septum/base (case F). The different ectopic locations also lead to different types of reentry, as summarised in Figure 6.2 (bottom panel) and illustrated in Figure 6.3.

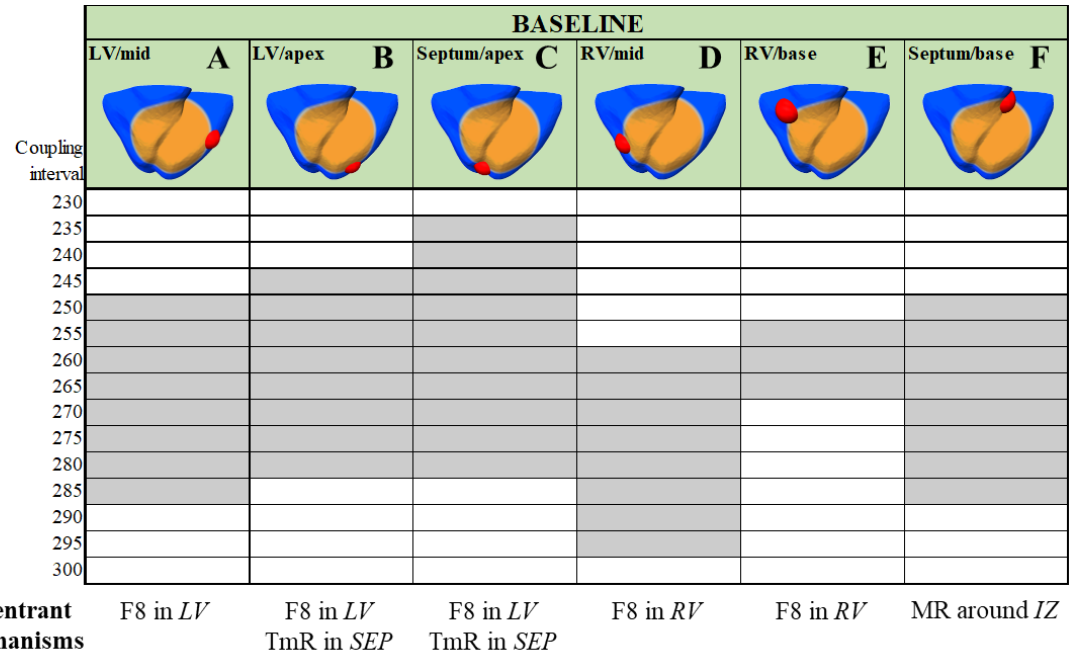


Figure 6.2. Vulnerability windows for reentry (grey boxes) for different locations of ectopic stimuli in acute regional transmural ischemia for LAD occlusion in baseline conditions. Ectopic stimulation applied at CI=230 to 300 ms at varying locations in the ischemic BZ (cases A to F). Reentrant mechanisms observed in the vulnerability windows are annotated below. The reentry location (italic font) refers to the pathway for retrograde propagation. F8: figure-of-eight reentry. TmR: transmural micro reentry. MR: macro-reentry. LV: left ventricle. SEP: septum. RV: right ventricle. IZ: ischemic zone.

Ectopic stimulus in the LV (Figure 6.2 A-C) and RV (Figure 6.2 D-E) lead to the establishment of figure-of-eight reentry, which is illustrated in Figure 6.3A. Following the ectopic stimulus, unidirectional conduction block occurs in the ICZ, and propagation proceeds around the BZ (400ms), then retrogradely into the ICZ (450-500ms) and reenters into the NZ of the LV (570ms), as reported in Chapter 5 and Janse's experiments (Janse et al., 1980).

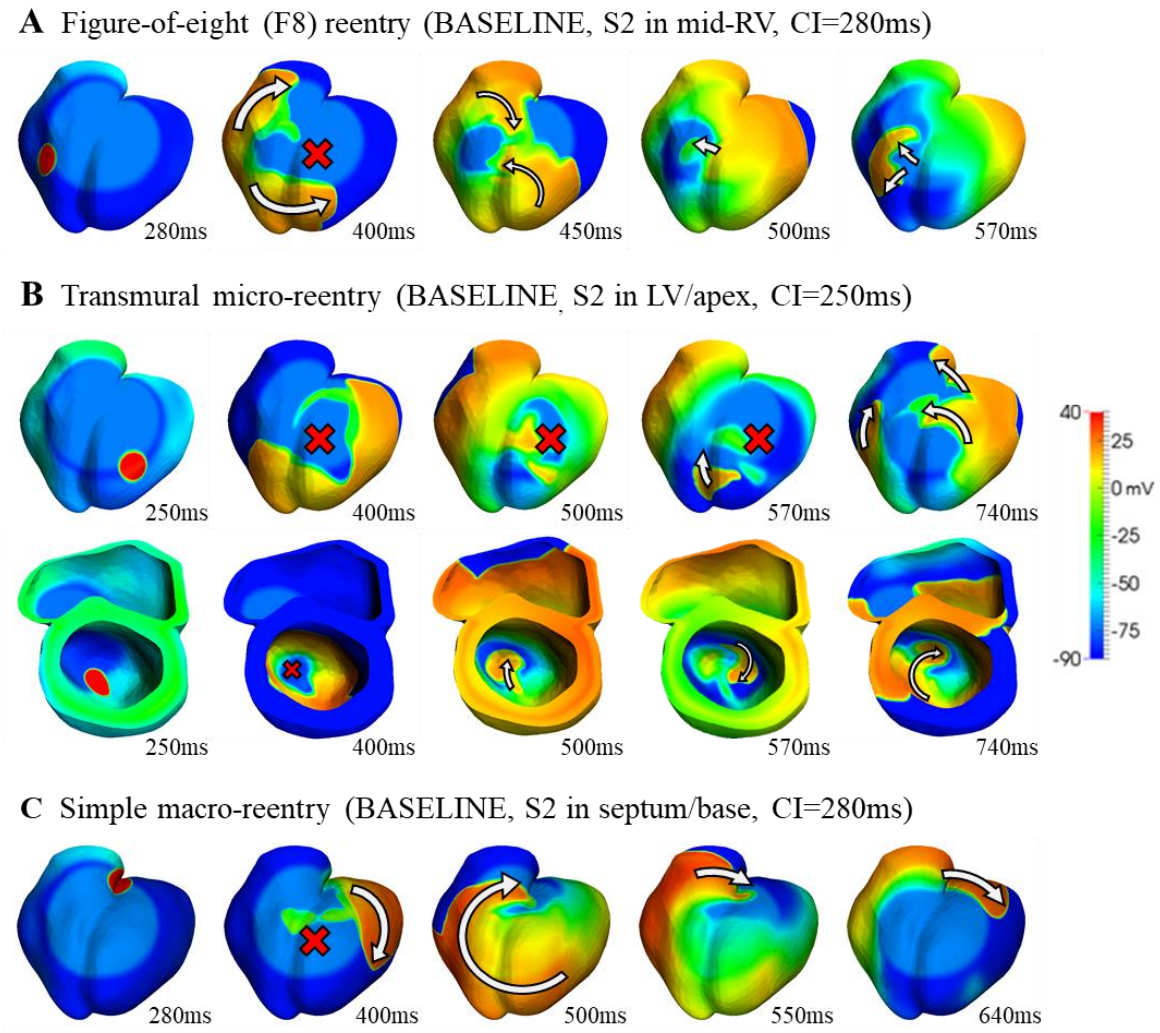


Figure 6.3. Main reentrant mechanisms observed in the ischemia-induced reentry simulations. A: Figure-of-eight macro-reentry in baseline ionic conditions, S2 triggered in the mid-LV at CI=270ms. B: Transmural micro-reentry in baseline ionic conditions, S2 triggered in the LV/apex at CI=250ms. Septal (top) and epicardial view (bottom). C: Simple macro-reentry, baseline ionic conditions, S2 triggered in the septum/base at CI=280ms.

In addition to figure-of-eight reentry, ectopic stimulus close to the apex (Cases B and C) also lead to establishment of transmural microreentries (Figure 6.3B). As shown in

Section 5.3.3, the transmural reentry gets established around the ischemic BZ in the septo-apical region.

Figure 6.3B shows that the ectopic stimulus causes a bidirectional conduction block (400-570ms) and no reentry (740ms) on the epicardium. Nevertheless, the ectopic stimulus propagates transmurally surrounding the BZ and reentering afterwards in the healthy tissue. This establishes a spiral wave, anchored in the BZ in the septo-apical region (Figure 6.3B, bottom, 500-740ms), as described in the previous chapter of this thesis. Finally, ectopic stimulus close to the base are also pro-arrhythmic as shown by the wide VW (case F), due to the establishment of macro-reentry circling around the IZ (Figure 6.3C). This type of reentry occurs following unidirectional block at the RV base, due to refractoriness caused by the previous S1 beat.

In summary, besides the electrophysiological heterogeneities induced by acute myocardial ischemia, the location of an ectopic stimulus has a crucial role in arrhythmogenesis. Particularly under Na^+ current block conditions, significant differences in vulnerability to reentry and VW width were observed, based on the anatomical asymmetry of the human ventricles.

6.3.3 Reduced Na^+ current availability promotes reentry inducibility particularly following ectopy in RV and septum/base

Figure 6.4 shows the effect of 50% block of the Na^+ current in the VWs for the 6 ectopic locations considered. Results show a large increase in vulnerability for reentry for ectopic stimuli in the RV (Figure 6.4 D-E) and the base of the septum (Figure 6.4 F), whereas for ectopic stimulations in LV the number of induced reentries is reduced (Figure 6.4 A-C). The most likely type of reentry is figure-of-eight with retrograde conduction through the LV towards the RV in cases D and E, and macro-reentry around the IZ in case F. Ectopics in the LV and septum also led to some cases of transmural reentry (Figure 6.4 B-C).

Figure 6.5 illustrates the mechanisms underlying the larger vulnerability to reentry under Na^+ block for ectopic stimuli located in the RV versus the LV, respectively (at similar distances in the long-axis plane, same coupling interval of 320ms, 50% Na^+ block). In Panels A and B, the top panel shows an epicardial view and the bottom one

presents a slice view of the short-axis plane, with changes in the orientation to illustrate optimally the different phases of reentry.

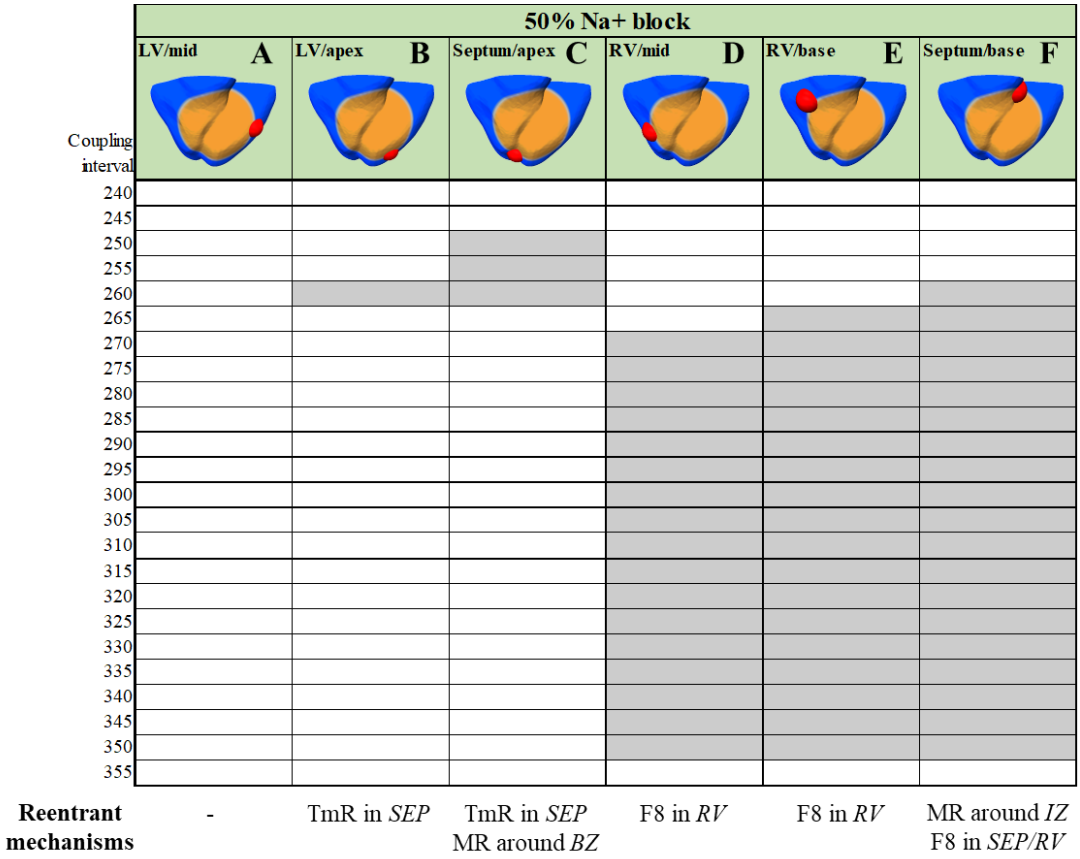


Figure 6.4. Vulnerability windows for reentry (grey boxes) for different locations of ectopic stimuli in acute regional transmural ischemia for LAD occlusion under 50% Na^+ channel block conditions. Ectopic stimulation applied at CI=240 to 355ms at varying locations in the ischemic BZ (cases A to F). Reentrant mechanisms observed in the vulnerability windows are annotated below. The reentry location (italic font) refers to the pathway for retrograde propagation. F8: figure-of-eight reentry. TmR: transmural micro-reentry. MR: macro-reentry. LV: left ventricle. SEP: septum. RV: right ventricle. IZ: ischemic zone.

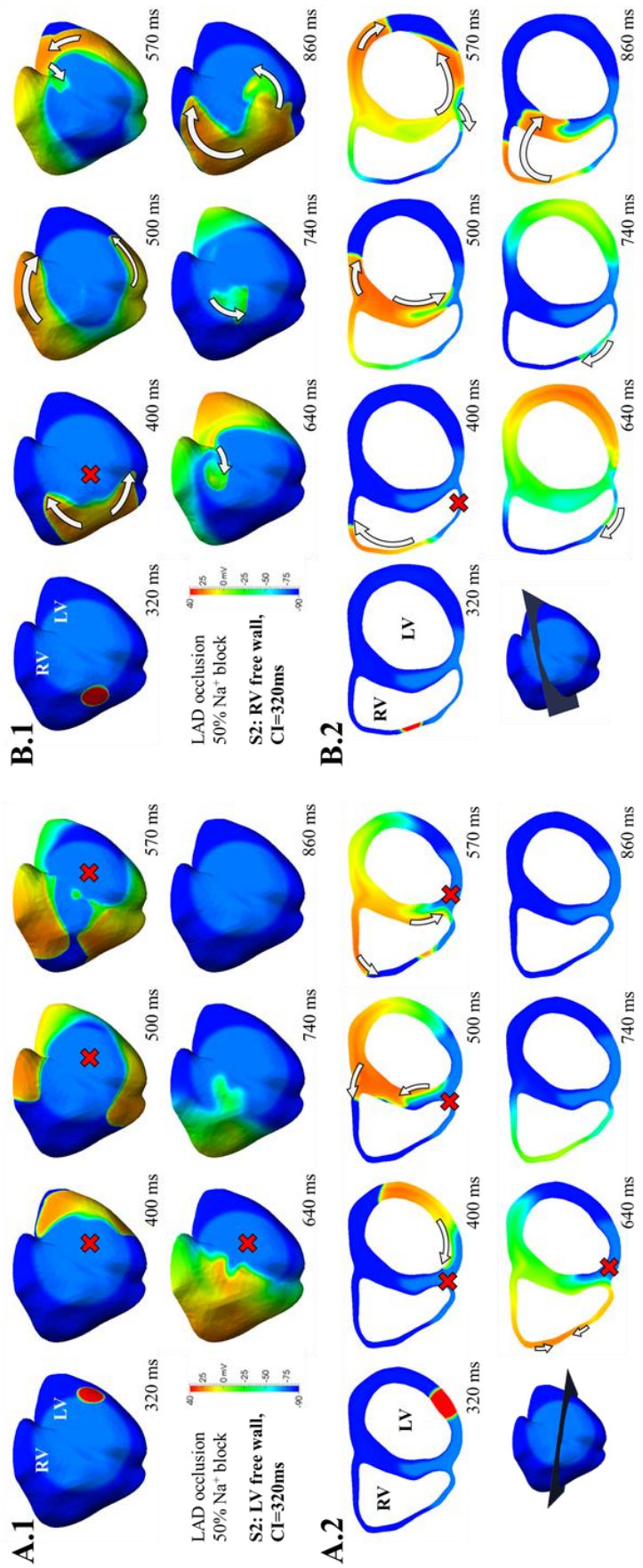

A.1
A.2
B.1
B.2
RV
LV
320 ms
400 ms
500 ms
570 ms
640 ms
740 ms
860 ms
LAD occlusion
50% Na+ block
S2: LV free wall,
CI=320ms
S2: RV free wall,
CI=320ms
40
25
0 mV
-25
-50
-75
-90

Figure 6.5. Comparison of activation sequences produced by ectopics set in LV and RV under 50% Na^+ block conditions. Panel A: Activation sequence triggered by an ectopic stimulus in the LV in simulated acute myocardial ischemia for LAD occlusion with 50% sodium channel block. A.1: Epicardial view. A.2: Slice visualization. Note that no reentry is produced due to bidirectional conduction block (represented with a red cross). B: Activation sequence triggered by an ectopic stimulus in the RV in simulated acute myocardial ischemia for LAD occlusion with 50% Na^+ channel block. B.1: Epicardial view. B.2: Slice visualization. Differently to A, the ectopic stimulus in the RV causes reentry based on unidirectional conduction block (400-500ms, red cross), posterior reentry (570-740ms) and finally retrograde propagation (860ms).

In Figure 6.5, Panel A.1 shows that the ectopic stimulus in the LV free wall propagates around the BZ, finding a conduction block in the ICZ (400-500ms). When the wavefront has surrounded the ischemic region (570ms), retrograde propagation (640-740ms) towards the LV dies out, and reentry fails to be established (860ms). Panel A.2 provides a transmural view, showing how following ectopic stimulation, propagation surrounds the LV cavity via the LV free wall and also through the subendocardial BZ (pink arrows, 400-450ms). Then, it progresses through the RV free wall (570-640ms) but eventually dies out as both normal and ischemic tissue are refractory (740-860ms).

Differently, Panel B.1 of Figure 6.5 displays a complete macro-reentry, starting with the stimulus propagating across the BZ (400-500ms). Afterwards, a slow-propagating wavefront enters the ICZ through the septum, causing retrograde propagation towards the RV (570-740ms). Finally, the reentry is completed and sustained (860ms). Further details to illustrate the differences between ectopics in the LV and RV are provided in Panels A.2 and B.2. In Panel B.2, the ectopic stimulus propagates exclusively across the RV free wall due to the conduction block found in the ischemic region, located in the anterior myocardial wall (400ms). Contrary to Panels A.1 (S2 in the LV), there is a conduction block towards the IZ (red cross), then the wavefront propagates through the septum and LV (500ms). Depolarised tissue in the junction between the septum and LV wall allows eventually a slow propagating wavefront towards the thinner and excitable RV myocardial wall (570-740ms). Once this wavefront propagates back into the healthy myocardium, the reentry is completed (860ms).

The comparison between Panels A and B in Figure 6.5 proves the determining role of ventricular anatomy in modulating reentry establishment for different ectopic locations. Both cases lead to divergent outcomes in scenarios with identical ionic settings. At early

stages, the activation sequence in both cases shows certain similarity (propagation across the ventricle hosting the ectopic stimulus, conduction block towards the septum, and propagation across septum). The final stages are however very different: retrograde propagation is only possible from LV/septum to RV and not conversely. This is explained by differences in source-sink mismatch associated to wall thickness, quantified in Figure 6.6. Myocardial wall widths were measured close to the junction, reporting 7 and 5mm in the septum and the LV, respectively. The RV wall is substantially thinner, about 2.4mm, thus establishing a substantial change in the propagation media that affects electrical conduction, promoting retrograde propagation only in the thick-to-thin direction blocking conduction from RV to LV and facilitating retrograde propagation.

The LV/RV differences in wall thickness are particularly important under Na^+ block conditions. Due to the remarkable increase of ΔERP by Na^+ block, a major part of the ICZ remains refractory when the wavefront surrounds it. Propagation can proceed from the thick LV to the thin RV, but fails from RV to LV, due to the differences in source-sink mismatch. This is illustrated in Figure 6.5B, 570-640ms, and Figure 6.5A, respectively.

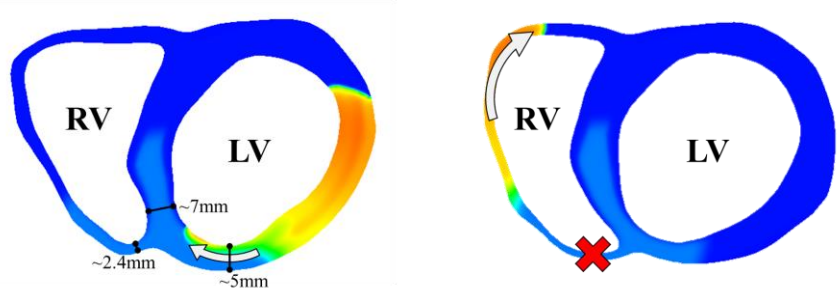


Figure 6.6. Measurement of myocardial width at the time of the reentry observed in Figure 6.5, A (left) and B (right) (timestamp 400ms).

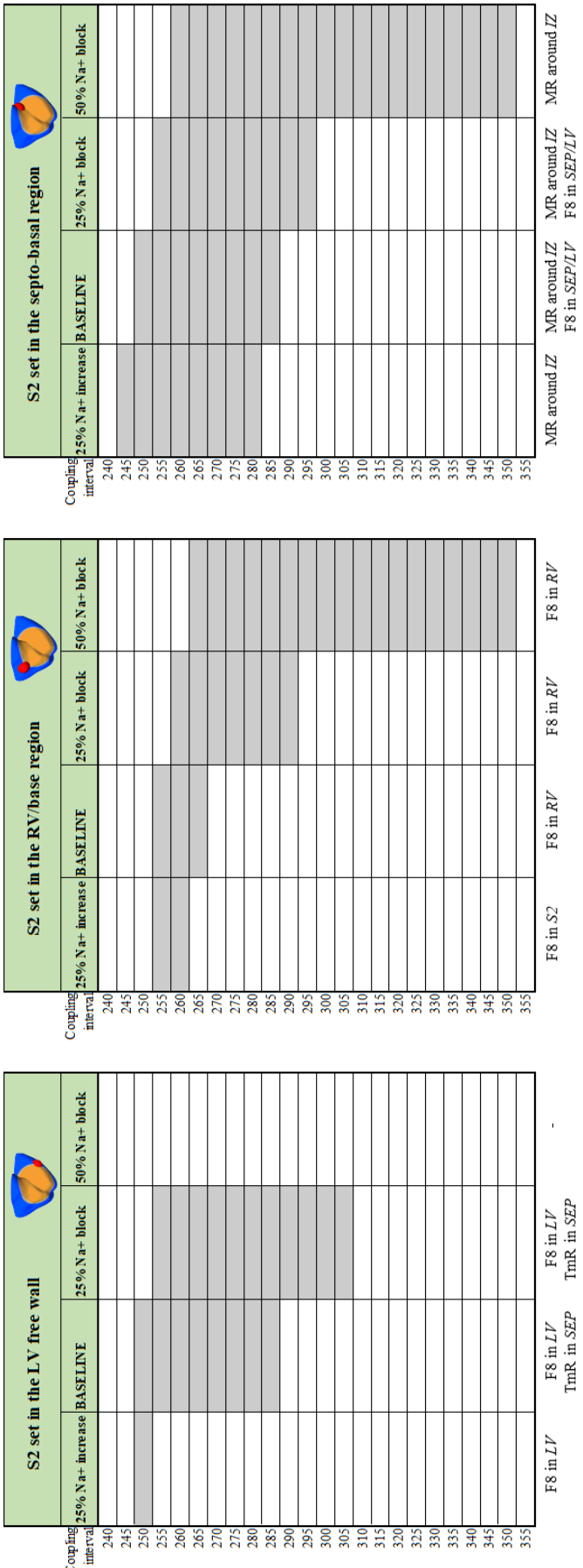

S2 set in the LV free wall
S2 set in the RV/base region
S2 set in the septo-basal region
Coupling interval
25% Na+ increase
BASELINE
25% Na+ block
50% Na+ block
240
245
250
255
260
265
270
275
280
285
290
295
300
305
310
315
320
325
330
335
340
345
350
355
F8 in LV
F8 in LV TmR in SEP
F8 in LV TmR in SEP
-
F8 in S2
F8 in RV
F8 in RV
F8 in RV
MR around IZ
MR around IZ F8 in SEP/LV
MR around IZ F8 in SEP/LV
MR around IZ

Figure 6.7. Vulnerability windows for reentry (grey boxes) for different locations of ectopic stimulus in acute regional transmural ischemia for LAD occlusion with diverse Na^+ channel alterations. Ectopic stimulus applied at CI=240 to 355ms at three S2 locations: LV free wall (left), RV base (mid) and septo-basal region (right). Reentrant mechanisms observed in the vulnerability windows calculated are annotated (bottom). The reentry location (italic font) refers to the pathway for retrograde propagation. Note that each S2 location triggers certain types of reentry and varying Na^+ availability affects the occurrence of them differently. F8: figure-of-eight reentry. TmR: transmural micro reentry. MR: macro-reentry. LV: left ventricle. SEP: septum. RV: right ventricle. IZ: ischemic zone.

6.3.4 Reentry induced by ectopic stimuli at the ventricular base are insensitive to moderate reductions in Na^+ current availability

This section investigates how arrhythmic risk and the mechanisms unravelled above may change with rather moderate changes in Na^+ current availability (25% rather than 50% reduction). As mentioned in Chapter 2, Section 2.9, flecainide, encainide or propafenone are considered class I anti-arrhythmic drugs since their main action mechanism is Na^+ channel blockage. As seen in Table 6.1, the effect of Na^+ channel blockers is highly dependent on the dose, but the level of reduction for clinical doses is significantly lower than the reported sodium channel decrease in patients with SCN5A mutations, such as Brugada patients. Thereby, drug action of class I anti-arrhythmic drugs was simulated by implementing a 25% Na^+ current block.

Figure 6.7 shows VWs obtained with simulations with S2 located in the LV (left panel), in the RV (mid panel) and in the septo-basal region (right panel) with -decreasingly-varying Na^+ current availability: 25% Na^+ increase, baseline ionic conditions, 25% Na^+ block and 50% Na^+ block.

The scenarios featuring 50% Na^+ block (Figure 6.7, right column in the tables) cause very large VWs (85-95ms), unless the S2 stimulus is located in the LV (VW = 0ms). In those cases, the bidirectional conduction block avoids the formation of reentries, based on the anatomical asymmetry of the ventricles, as discussed in the previous section.

Moderate (25%) Na^+ block promotes the formation of figure-of-eight macro-reentries caused by stimuli triggered in the LV or RV (Figure 6.7, left and mid panel, third column), reporting 20-25ms larger VWs in comparison to normal ionic conditions.

However, if the ectopic stimulus is set in the base (Figure 6.7, right panel, third column), the VW is similar to baseline conditions (40-45ms).

Alternative treatments increasing Na^+ current availability (Lau et al., 2009) could represent effective anti-arrhythmic therapies whose mechanism of action is based on reducing electrophysiological heterogeneities caused by ischemia and enhancing electrical propagation in the myocardial tissue. For 25% increase in Na^+ channel availability, VWs were substantially shorter than in control, both for LV and RV S2 locations (LV: 5ms, RV: 10ms), in comparison to baseline conditions (LV: 40ms, RV: 15ms) (Figure 6.7, left and mid table, first column). However, ectopics at the base lead to VW as large as in baseline conditions (40ms), as illustrated in Figure 6.7, right table, first column.

6.4 Discussion

With this study, the modelling and simulation pipeline presented in previous chapters has been extended to simulate acute myocardial ischemia under varying Na^+ current availability. The results show that Na^+ channel block significantly increases arrhythmic risk by enlarging VWs for reentry. My findings suggest that anatomical differences between RV and LV wall thickness are shown to play a crucial role in ischemia-induced arrhythmogenesis, particularly under severe Na^+ current block. Thereby, ectopics originating from the RV and the basal region are very prone to cause reentry also with low Na^+ current availability (see Figure 6.4). Stimuli propagating from the basal region are highly arrhythmogenic, regardless of whether the Na^+ current is blocked or enhanced. Conversely, ectopic stimuli originating from the LV often fail to propagate from the thin RV towards the thick LV hindering the establishment of reentry. Thus, the obtained results highlight the importance of ventricular anatomy and the location of the ectopic stimulus in the formation of arrhythmias and the safety of anti-arrhythmic treatments.

Na^+ channel blockers reduce cardiac tissue excitability and prolong the refractory period in ventricular cardiomyocytes, as previously reported by other authors (Roden, 1996; Starmer et al., 1984, 1991; Tice et al., 2007). Although, Na^+ blockers are commonly used to treat well extended cardiac pathologies, such as atrial fibrillation (Aliot et al., 2011), their use is not recommended for patients suffering from patients

under ischemic risk, as evidenced by the CAST trials (Cardiac Arrhythmia Suppression Trial II Investigators, 1992; Echt et al., 1991). The results in this chapter provide evidence of the increased arrhythmic risk resulting from Na^+ channel block when co-existing with acute myocardial ischemia. These findings are in agreement with the increased rate of cardiac events and mortality observed in those patients recruited in the CAST trials with recurrent ischemia episodes produced by a reduced and uninterrupted coronary blood irrigation (Anderson et al., 1994; Greenberg et al., 1995). Furthermore, studies have extensively linked alterations in the SCN5A gen with low Na^+ current availability and high arrhythmic risk, especially under ischemic conditions (Hu et al., 2007; Kujime et al., 2017). Together with the electrophysiological abnormalities in the myocardial tissue, arrhythmogenesis in the low Na^+ current availability setting was drastically influenced by the available anatomical pathways that give rise to reentry, which are shaped by the location of the ectopic stimuli.

In simulations considering Na^+ block, ectopies in the RV were more prone to induce reentries than those in the LV due to differences in ventricular thickness and hence sink-source mismatch. This is consistent with studies stating that conduction blocks are produced in the surface area with the steepest thin-to-thick transition (Ciaccio et al., 2007, 2015). Furthermore, a simulation study on non-ischemic ventricles by (Boyle et al., 2014) identified source-sink mismatch caused by low Na^+ current availability as a potent substrate for sustained arrhythmia caused by ectopics triggered close to regions of wall expansion. The authors determined the septal insertion region as the most prone to cause conduction block due to source-sink mismatch, potentially leading to sustained reentries. Subsequently, Boyle et al. identified the right ventricular outflow tract (RVOT) and posteroinferior septal region of the RV as the most pro-arrhythmic ectopic locations. These results are fully compatible with my findings: 1) the simulations of low Na^+ current availability presented in this thesis identified a higher occurrence of reentries explained by the presence of acute myocardial ischemia in the anterior myocardial wall; 2) my results also identified the septal insertion region as crucial in the establishment of reentries caused by RV ectopics; and 3) although the ectopic locations in this chapter are not identical to those in Boyle's work, in both studies ectopics

triggered in the basal and septal regions of the RV are the most prone to induced reentries.

In these results, stimuli originating from the septo-basal region caused the largest VWs, characterising them not only as highly pro-arrhythmic, but also as a robust reentrant mechanism regardless of Na^+ channel availability. These observations can be compared carefully with the literature: the free-wall region of the RVOT is identified in the literature as the most common origin of premature stimuli potentially leading to ventricular arrhythmias among Brugada patients (Letsas et al., 2014; Morita et al., 2003). This would be consistent with the widest VWs computed, based on ectopies originating from the RV/basal region of the heart, due to the reentrant mechanisms promoted by the interventricular differences in that myocardial region. At this point, it is possible to question if premature stimuli in the RVOT are simply the most common or otherwise the most prone to propagate across the myocardium and potentially trigger arrhythmias.

The findings presented in this chapter suggest that enhancing Na^+ channel conductance does not guarantee an effective anti-arrhythmic strategy for patients with unifocal ectopies originating in the basal region of the myocardium or its adjacent areas. This reentrant mechanism proliferates under any level of dispersion of refractoriness caused by ischemia, including increased Na^+ current conditions. Furthermore, certain simulations with increased Na^+ current availability showed macro-reentries formed around the ectopic location due to an excessively low refractoriness in the tissue. This allows a fast electrical recovery that provides instability to the activation sequence in the myocardium, as seen previously (Ellinor et al., 2008; Li et al., 2009; Makiyama et al., 2008). Increasing Na^+ current is shown to be only partially effective as an anti-arrhythmic strategy for patients under ischemic risk. The results suggest the urge to consider complementary strategies.

6.5 Limitations

The effects of Na^+ channel blockers and SCN5A mutations are not limited to reducing the Na^+ current conductance. For instance, Brugada syndrome is also associated with additional heterogeneities in the RVOT (either in depolarisation, repolarisation, or a combination of both) (Bueno-Orovio et al., 2015; Meregalli et al., 2005; Zhang et al.,

2015), or abnormal recovery from inactivation in specific SCN5A variants (Deschênes et al., 2000; Shirai et al., 2002; Tan et al., 2006), to cite some, which were not considered in this chapter. However, decreased Na^+ current functionality is an important factor of the disease, and here we focused on isolating its modulation of arrhythmic risk under concurring acute regional ischemia.

Whereas in the CAST trials Na^+ blockers were administrated following myocardial infarction, in the simulations presented in this chapter acute myocardial ischemia was simulated under Na^+ block conditions. Therefore, CAST patients with recurrent acute ischemia episodes instead of chronic infarction represents the most similar conditions to the scenarios simulated.

6.6 Conclusion

In this chapter, the effects of varying Na^+ current availability on ischemia-induced arrhythmogenesis were investigated in order to identify mechanistic evidence of the high arrhythmic risk observed in ischemic patients.

According to the simulations conducted within this study, the occurrence of ischemia-induced reentry proliferates under low Na^+ current availability. Under severely reduced Na^+ current availability, anatomical differences in ventricular wall thickness became crucial. Ectopies originating from the RV and the basal region were highly pro-arrhythmic due to a higher rate of successful retrograde propagation, whereas LV stimuli were prone to cause a bidirectional conduction block and hence no reentry.

The obtained results suggest that enhancing Na^+ channel availability could be an effective anti-arrhythmic strategy for reducing ischemia-induced refractoriness dispersion, which is the main precursor of ischemia-induced arrhythmic risk. However, its effectiveness depended strongly on the anatomical pathways for reentry, influenced by the location of the ectopic stimuli.

In the next chapter, and last one in this thesis, I highlight the main findings and conclusions presented, and propose venues for future research.

7 CONCLUSIONS AND FUTURE WORK

The primary goal of this thesis was the identification of mechanisms in human acute ischemia explaining variability in arrhythmic risk and ECG abnormalities. For this, I constructed a computational pipeline for modelling and simulating human acute myocardial ischemia, posteriorly validated using experimental and clinical data. Then, I evaluated the role of size, location and transmural extent of the ischemic region within the myocardial tissue. In addition to this, I analysed the effects of slow myocardial propagation in the remote myocardium, typically induced by comorbidities, such as diabetes or fibrosis. The third aim of this thesis was to provide mechanistic evidence behind the high arrhythmic risk triggered by low Na^+ availability among ischemic patients, associated to both the high mortality observed in the CAST study and the high occurrence of cardiac events in patients with SCN5A mutations under ischemic conditions. Investigating the role of Na^+ availability in ischemia-induced reentries could help to propose new effective anti-arrhythmic therapies by targeting the arrhythmogenic mechanism responsible for the increased risk.

7.1 Summary

CAD is the most common cause of death in the world. Narrowing of coronary arteries can lead to ischemia in the myocardial tissue, which is a major precursor of cardiac arrhythmias. The most pro-arrhythmic phase in ischemia is known to happen 10-15 minutes post occlusion, promoting a high occurrence of cardiac events. Certain life habits promote the formation of ischemia-induced arrhythmogenesis, such as smoking,

a sedentary lifestyle or poor dietary habits (Ignarro et al., 2007). Moreover, certain drugs are known to increase arrhythmic risk among ischemic patients due to their potential side-effects (Anderson et al., 1994; Kloth et al., 2015; Pratt et al., 1998).

Although acute myocardial ischemia is associated with high risk of arrhythmia, the resulting abnormalities on the ECG are not always specific and may vary substantially among patients. ECG has been studied extensively, aiming to link certain ECG abnormalities with the arrhythmic risk induced by myocardial ischemia. The most common ECG biomarker considered for diagnosis of ischemia is the deviation of the ST segment (Andersen et al., 2010; Zellweger et al., 2003). ST elevation in myocardial ischemia has been associated with severe coronary occlusions producing fully transmural ischemic regions, whereas ST depression is linked to incomplete coronary occlusions, promoting subendocardial ischemic regions (Birnbaum and Drew, 2003; Potse et al., 2006; Wilhelms et al., 2011). Differences in ischemic symptoms between sexes, including ECG abnormalities, have been proven to represent a major challenge in diagnosis and treatment of patients, especially in women (British Heart Foundation, 2019b; Regitz-Zagrosek, 2011; Wake and Yoshiyama, 2009).

ST elevation myocardial ischemia is generally linked to higher mortality among ischemic patients (Zellweger et al., 2003), but silent or transient ischemia episodes are yet associated with a great occurrence of adverse cardiac events (Ahmed et al., 2007; Gottlieb et al., 1986, 1988). In this thesis, I have aimed to undercover the mechanisms underlying variability in arrhythmic risk and ECG abnormalities in ischemic patients, in order to investigate whether the arrhythmogenic mechanisms in silent ischemia differ from those in ST elevation ischemia. For this, I have constructed an extensively validated modelling and simulation framework of human acute myocardial ischemia. The use of *in silico* techniques for exploring the arrhythmic mechanisms linked to acute myocardial ischemia is justified by the high difficulty in conducting experiments due to the complex spatiotemporal dynamics of ischemia, continuously changing the substrate.

In addition to the intrinsic arrhythmic risk linked to ischemia, the patient's conditions play a major role in the establishment of cardiac events and their outcome. Myocardial ischemia is associated with increased risk in patients with Na^+ channel mutations (Benito et al., 2008; Royer et al., 2005), or following administration of Na^+ blockers, as

reported in the famous CAST trials (Anderson et al., 1994; Cardiac Arrhythmia Suppression Trial II Investigators, 1992; Echt et al., 1991). In this thesis, I conducted *in silico* trials using the computational framework for modelling and simulating acute myocardial ischemia to provide the mechanistic evidence explaining the increased risk in ischemic patients with alterations in the Na^+ availability. I have identified ischemia-induced arrhythmogenic mechanisms facilitated by Na^+ block, which could potentially lead to refined effective anti-arrhythmic strategies. These advances would be of great relevance for treating increased arrhythmic risk associated with patients suffering from SCN5A mutations, whilst providing a detailed investigation of the pro-arrhythmic consequences of low Na^+ availability among ischemic patients.

In Chapter 2, I first introduced the bases of cardiac function and anatomy related to this work. The electrophysiology of cardiomyocytes was described, which is governed by the influx and efflux of ions in the cell. After describing the quantification of electrophysiological properties in cardiac tissue, I offered a literature review on acute myocardial ischemia and induced arrhythmic risk, providing the reader with the context supporting the research presented in this thesis. I also described the mechanisms explaining ischemia-induced ECG changes. To conclude, I discussed briefly anti-arrhythmic therapies and their multiple and serious side-effects, some of them pro-arrhythmic.

In Chapter 3, I described the computational methods on which I based the computational framework for simulating human cardiac electrophysiology. I started by introducing the Hodgkin-Huxley model of the AP in the squid giant axon, which is the precursor of cardiac cell models. I then showed the evolution of cardiac cell models during the last decades and their main differences. I provided extensive information about the O'Hara-Rudy model, the model of choice in this thesis, in addition to the modifications incorporated to enable propagation under ischemic conditions. The techniques used for integrating the cell model into a multi-scale torso/ventricular model were presented. Then, I introduced the bidomain equations for simulating electrical propagation, and the methods used to discretise these equations in numerical approximations. These methods are integrated into the software used for the simulations, CHASTE, briefly described in this chapter. I conducted a convergence analysis, comparing different time and mesh discretisation resolutions. Finally, I

introduced the method implemented for simulated drug effects in the cardiac electrophysiology simulations.

In Chapter 4, I presented the computational framework to model and simulate the electrophysiological consequences of acute myocardial ischemia built for the research in this thesis. Firstly, I described the implementation in the model of diverse physiological features observed clinically and experimentally. Detailed descriptions of the meshes, electrophysiological heterogeneities, stimulation protocols, modelling of the ischemic region and incorporation of drug effects were provided. Furthermore, I presented the methods used to simulate the ECG and to quantify arrhythmic risk in the considered configurations of ischemia. A section in this chapter described the pre- and post-processing methods used in the computational pipeline. To conclude, I evaluated the model at tissue and organ levels by comparing its results under control and ischemic conditions against both clinical and experimental data from the literature.

In Chapter 5, I investigated the effects of variability in ischemia on the formation of arrhythmias and the ECG signature. I quantified differences in arrhythmogenesis based on the transmural extent, size and location of the ischemic region. Additionally, I identified a higher arrhythmic risk in ischemia scenarios featuring slower propagation conditions in the remote myocardium, favouring the formation of reentries. I identified two mechanisms of reentry: the well-known figure-of-eight macro-reentries, but also a high occurrence of transmural micro-reentries, especially common in the septo-apical region for LAD occlusion. Transmural ischemia was prone to produce macro-reentries and pronounced ECG changes, whereas subendocardial ischemia yielded the occurrence of transmural micro-reentries while exhibiting very mild or even negligible derived ECG abnormalities.

In Chapter 6, I analysed the role of low Na^+ availability in arrhythmogenesis. I used the same computational framework as in Chapter 5, extended to incorporate variability in Na^+ current availability as a consequence of drug action or genetic mutations. The results of the study provide mechanistic evidence on the pro-arrhythmic effects of low Na^+ availability when co-existing with ischemia, as observed in ischemic patients with SCN5A mutations or administered Na^+ blockers. Reduced Na^+ current availability leads to increased arrhythmic risk caused by RV ectopies in comparison to LV ectopies,

based on the asymmetrical anatomy of the ventricles. In fact, ectopies triggered in the RV/base region were shown to be particularly prone to cause reentries in scenarios under any circumstances.

7.2 Main findings

I built a computational framework to simulate healthy and ischemic human cardiac electrophysiology, constructed and validated using extensive clinical and experimental data (Carmeliet, 1999; Coronel et al., 1988; Durrer et al., 1970; Sutton et al., 2000; Taggart et al., 2000; Wilensky et al., 1986). After its validation, the simulation platform was able to realistically reproduce both the arrhythmogenic mechanisms observed experimentally in human acute ischemia, and their characteristic ECG signatures. Most importantly, the model provides mechanistic evidence to unravel the relationship between ionic and tissue changes caused by ischemia and the derived arrhythmic risk. While electrophysiological changes caused by myocardial ischemia have been extensively studied (Carmeliet, 1999; Coronel et al., 1988, 1991; Kodama et al., 1984; Moréna et al., 1980; Sutton et al., 2000; Taggart et al., 2000), variability in arrhythmic risk and ECG abnormalities among ischemic patients remains not completely understood due to associated technological or ethical limitations.

I investigated differences in size, transmural extent and location of the ischemic region, and their effects on arrhythmogenesis and ECG changes. A higher propensity of reentries in LAD occlusion than in LCX occlusion was observed, due to the anatomical pathways for reentry provided by the septal wall. Larger ischemic regions were more pro-arrhythmic due to the increased rate of successful retrograde propagation, whereas smaller ischemic regions were prone to induce bidirectional block, therefore reducing arrhythmic risk. Transmural ischemia was shown to be more pro-arrhythmic than subendocardial ischemia. However, ECG abnormalities were prominent only in scenarios of transmural ischemia involving large volumes of ischemic tissue. Conversely, subendocardial ischemia produced mild or negligible ECG abnormalities, although it was still highly pro-arrhythmic. Previous clinical studies support my findings (Gottlieb et al., 1986; Kawano et al., 2016; Shea et al., 1985; Zellweger et al., 2003), as silent ischemia is associated with partial and reversible coronary occlusions and the absence of ECG changes despite the arrhythmic risk induced.

I observed two main types of reentry: typical macro-reentries formed around the ischemic region and transmural micro-reentries, very common in LAD occlusion, and established by a spiral wave anchored to the apico-septal region. Slow propagation in the remote myocardium promoted the occurrence of reentries, which explains the increased arrhythmic risk observed in patients suffering from co-existing conditions affecting the myocardial tissue, such as diabetes or fibrosis (Coronel et al., 2005; Nygren et al., 2007).

The CAST trials were conducted under the hypothesis that class I anti-arrhythmic drugs would be protective against the occurrence of ectopic stimuli triggering arrhythmias (Echt et al., 1991). The lower excitability caused by Na^+ block supports *a priori* this hypothesis. However, the concomitant electrophysiological changes of Na^+ block and acute myocardial ischemia significantly increased arrhythmic risk and mortality among patients, especially in those with recurrent ischemia episodes caused by reduced coronary flow, instead of complete coronary occlusion (Anderson et al., 1994; Greenberg et al., 1995). I used the modelling and simulation framework to mechanistically investigate the effects of Na^+ channel availability in the setting of acute ischemia. Indeed, Na^+ channel block affects substantially the formation of reentries based on a pronounced increase of dispersion of refractoriness between the healthy and ischemic tissues and slowed conduction velocity.

Moreover, I simulated LAD occlusion and analysed the effects of the location of the ectopic stimulus, which I proved to be a key factor determining the reentrant mechanism triggered. Ectopies located close to the septum are prone to cause transmural micro-reentries in the septal wall, whereas those originating in the base or the mid-ventricular region cause macro-reentries. Low Na^+ availability causes reduced excitability that promotes changes in conduction velocity in the myocardium: electrical wavefronts propagating from the thin RV to the thicker LV are often blocked, whereas retrograde propagation from the thick LV to the thinner RV is highly likely. Due to the asymmetric ventricular anatomy, ectopic stimuli triggered in the RV and base are more prone to induce retrograde propagation, and hence arrhythmias.

Although increasing Na^+ availability had an anti-arrhythmic effect, its effectiveness varied depending on the S2 location. For instance, ectopics originating from the basal

region were the most pro-arrhythmic, independently of the co-existence of any Na^+ channel alteration, including the increase of the Na^+ current conductance. Thus, the findings support the critical role of the RV base and outflow tract in arrhythmic risk induced by unifocal ectopic stimuli (Boyle et al., 2014; Letsas et al., 2014; Morita et al., 2003). The results obtained could contribute to the conception of anti-arrhythmic treatments in patients with SCN5A mutations.

7.3 Future work

Although the presented computational framework is well aligned with the purposes of this thesis, as in any other case of modelling and simulation studies, the system could be extended for additional investigations. An extended simulation pipeline would allow to investigate further aspects in the pathophysiology of myocardial ischemia.

7.3.1 Ectopic stimuli

Steep gradients in the ischemic BZ have been shown to produce electrotonically-triggered depolarisations that could result on ectopic depolarisations, potentially triggering arrhythmias (Coronel et al., 1991; Janse et al., 1980). In Chapters 5 and 6, ectopic stimuli were imposed in the ischemic BZ to quantify arrhythmic risk at varying ectopic locations. Therefore, I propose to expand the model to reproduce spontaneous depolarisations induced by ischemia.

Firstly, modelling the occurrence of this phenomena would throw light on the specific circumstances leading to the generation of ectopic stimuli. Secondly, and potentially more importantly, this study would allow to investigate under which ischemic conditions is the occurrence of premature depolarisations most likely, providing usable knowledge in the management of ischemic patients.

7.3.2 Purkinje system

The modelling and simulation pipeline used in this thesis implements an abstraction of the trifascicular conduction system, as presented in Section 4.4. This provided a realistic stimulation sequence that reproduces experimental findings. However, the simulation framework could be expanded to incorporate a detailed anatomical representation of the Purkinje network, its differing electrophysiological properties, and its coupling with the ventricular myocardium.

This is of great relevance to investigate the dispersion in APD prolongation between ventricular and Purkinje cardiomyocytes under drug action, potentially providing mechanistic evidence in the formation of Torsade de Pointes. Additionally, this work could be used to unravel whether reentries in the fast conduction system plays a role in sustaining ventricular arrhythmias.

7.3.3 Electromechanical model of the ventricles

This work covers the modelling and simulation of human cardiac electrophysiology, and therefore mechanics are not within the scope of the thesis. Nevertheless, the implementation of a coupled model of cardiac electrophysiology and electromechanics would open up new possibilities, allowing other diseases or drugs affecting cardiac contractility to be investigated.

7.4 Conclusions

Acute myocardial ischemia has been extensively studied in experimental studies, providing information about the tissue abnormalities induced by ischemia at the ionic, cellular and tissue levels. However, it is not completely understood how these ionic changes underlie the high arrhythmic risk in ischemic patients. Variability in ECG signatures and in arrhythmic risk among ischemic patients remain a challenge, complicating the diagnosis and treatment of those patients with minor signs of this lethal condition.

This thesis provides mechanistic knowledge on variability in ECG abnormalities and arrhythmic risk induced by acute ischemia. I developed a computational framework to model and simulate human cardiac electrophysiology under conditions of acute regional myocardial ischemia. The simulation studies were designed to represent variability in ischemic conditions, including slower electrical propagation in the remote myocardium, and different locations, transmural extents and sizes of the ischemic region. One of the main findings is the identification of stable transmural micro-reentries in the apicoseptal region as an important mechanism inducing arrhythmic risk in LAD occlusion. Subendocardial ischemia induced mild or negligible abnormalities in the simulated ECG, despite yielding sustained reentries, confirming the lethal nature of silent ischemia.

Finally, I investigated the interplay between acute myocardial ischemia and low Na^+ availability. The high occurrence of cardiac events observed in patients with SCN5A mutations, such as Brugada syndrome, and the high mortality among ischemic patients using Na^+ blockers is a well-known basis to hypothesise the increased arrhythmic risk in ischemic patients under low Na^+ availability. The results obtained from the simulations support this hypothesis, but importantly they highlight the importance of ventricular anatomy in the formation and sustainability of arrhythmias. Under reduced Na^+ availability, ectopic stimuli triggered in the RV and basal region of the heart were particularly pro-arrhythmic compared to other ectopic locations, due to an enlarged source-sink mismatch promoted by the low tissue excitability and the asymmetrical anatomy of the ventricles.

Advances in healthcare have significantly increased the lifespan of patients living with myocardial ischemia. Still, patients suffering from comorbidities derived from modern lifestyles, such as obesity or type 2 diabetes, represent a growing risk population of myocardial ischemia. New effective and affordable healthcare strategies are required to overcome a challenge playing a crucial role during the next decades. In this thesis, I present a valid example of how *in silico* experimenting can provide insights in cardiovascular disease, difficult or impossible to achieve otherwise.

8 REFERENCES

Ahmed, A.H., Shankar, K., Eftekhari, H., Munir, M., Robertson, J., Brewer, A., Stupin, I.V., and Casscells, S.W. (2007). Silent myocardial ischemia: Current perspectives and future directions. Exp. Clin. Cardiol. *12*, 189–196.

Aliot, E., Capucci, A., Crijns, H.J., Goette, A., and Tamargo, J. (2011). Twenty-five years in the making: flecainide is safe and effective for the management of atrial fibrillation. Europace *13*, 161–173.

Andersen, M.P., Terkelsen, C.J., Sørensen, J.T., Kaltoft, A.K., Nielsen, S.S., Struijk, J.J., and Bøtker, H.E. (2010). The ST injury vector: electrocardiogram-based estimation of location and extent of myocardial ischemia. J. Electrocardiol. *43*, 121–131.

Anderson, J.L., Platia, E.V., Hallstrom, A., Henthorn, R.W., Buckingham, T.A., Carlson, M.D., and Carson, P.E. (1994). Interaction of baseline characteristics with the hazard of encainide, flecainide, and moricizine therapy in patients with myocardial infarction. A possible explanation for increased mortality in the Cardiac Arrhythmia Suppression Trial (CAST). Circulation *90*, 2843–2852.

Arevalo, H., Plank, G., Helm, P., Halperin, H., and Trayanova, N. (2013). Tachycardia in Post-Infarction Hearts: Insights from 3D Image-Based Ventricular Models. PLOS ONE *8*, e68872.

Arevalo, H.J., Vadakkumpadan, F., Guallar, E., Jebb, A., Malamas, P., Wu, K.C., and Trayanova, N.A. (2016). Arrhythmia risk stratification of patients after myocardial infarction using personalized heart models. Nat. Commun. *7*, ncomms11437.

Becker, A., Bos, G., de Vegt, F., Kostense, P.J., Dekker, J.M., Nijpels, G., Heine, R.J., Bouter, L.M., and Stehouwer, C.D.A. (2003). Cardiovascular events in type 2 diabetes: comparison with nondiabetic individuals without and with prior cardiovascular disease. 10-year follow-up of the Hoorn Study. Eur. Heart J. *24*, 1406–1413.

Benito, B., Brugada, R., Brugada, J., and Brugada, P. (2008). Brugada Syndrome. Prog. Cardiovasc. Dis. *51*, 1–22.

Berecki, G., Wilders, R., de Jonge, B., van Ginneken, A.C.G., and Verkerk, A.O. (2010). Re-Evaluation of the Action Potential Upstroke Velocity as a Measure of the Na+ Current in Cardiac Myocytes at Physiological Conditions. PLoS ONE *5*.

Bernabeu, M.O., Wallman, M., and Rodriguez, B. (2010). Shock-induced arrhythmogenesis in the human heart: A computational modelling study. Conf. Proc. Annu. Int. Conf. IEEE Eng. Med. Biol. Soc. IEEE Eng. Med. Biol. Soc. Annu. Conf. *2010*, 760–763.

Bernabeu, M.O., Southern, J., Wilson, N., Strazdins, P., Cooper, J., and Pitt-Francis, J. (2014). Chaste: A case study of parallelisation of an open source finite-element solver with applications to computational cardiac electrophysiology simulation. Int. J. High Perform. Comput. Appl. *28*, 13–32.

Birnbaum, Y., and Drew, B.J. (2003). The electrocardiogram in ST elevation acute myocardial infarction: correlation with coronary anatomy and prognosis. Postgrad. Med. J. *79*, 490–504.

Birse, R.M. (2004). Muirhead, Alexander (1848–1920), electrical engineer (Oxford University Press).

Bishop, M.J., Plank, G., Burton, R.A.B., Schneider, J.E., Gavaghan, D.J., Grau, V., and Kohl, P. (2010). Development of an anatomically detailed MRI-derived rabbit ventricular model and assessment of its impact on simulations of electrophysiological function. Am. J. Physiol. - Heart Circ. Physiol. *298*, H699–H718.

Blackburn, H.W., and Simonson, E. (1957). The total QRS duration. Am. Heart J. *53*, 699–710.

Bousseljot, R., Kreiseler, D., and Schnabel, A. (2009). Nutzung der EKG-Signaldatenbank CARDIODAT der PTB über das Internet. Biomed. Tech. Eng. *40*, 317–318.

Boyle, P.M., Park, C.J., Arevalo, H.J., Vigmond, E.J., and Trayanova, N.A. (2014). Sodium Current Reduction Unmasks a Structure-Dependent Substrate for Arrhythmogenesis in the Normal Ventricles. PLOS ONE *9*, e86947.

Boyne, T.S., Koplan, B.A., Parsons, W.J., Smith, W.H., Watson, D.D., and Beller, G.A. (1997). Predicting adverse outcome with exercise SPECT technetium-99m sestamibi imaging in patients with suspected or known coronary artery disease. Am. J. Cardiol. *79*, 270–274.

Brahmajothi, M.V., Morales, M.J., Reimer, K.A., and Strauss, H.C. (1997). Regional localization of ERG, the channel protein responsible for the rapid component of the delayed rectifier, K+ current in the ferret heart. Circ. Res. *81*, 128–135.

Brennan, T., Fink, M., and Rodriguez, B. (2009). Multiscale modelling of drug-induced effects on cardiac electrophysiological activity. Eur. J. Pharm. Sci. Off. J. Eur. Fed. Pharm. Sci. *36*, 62–77.

British Heart Foundation (2019a). Potential new treatment for heart attack.

British Heart Foundation (2019b). Bias and Biology.

Brugada, R., Brugada, J., Antzelevitch, C., Kirsch, G.E., Potenza, D., Towbin, J.A., and Brugada, P. (2000). Sodium channel blockers identify risk for sudden death in patients with ST-segment elevation and right bundle branch block but structurally normal hearts. Circulation *101*, 510–515.

Bueno-Orovio, A., Cherry, E.M., Evans, S.J., and Fenton, F.H. (2015). Basis for the Induction of Tissue-Level Phase-2 Reentry as a Repolarization Disorder in the Brugada Syndrome. BioMed Res. Int. *2015*, 197586.

Burton, F.L., and Cobbe, S.M. (2001). Dispersion of ventricular repolarization and refractory period. Cardiovasc. Res. *50*, 10–23.

Buza, V., Rajagopalan, B., and Curtis, A.B. (2017). Cancer Treatment–Induced Arrhythmias: Focus on Chemotherapy and Targeted Therapies. Circ. Arrhythm. Electrophysiol. *10*, e005443.

Caldwell, B.J., Trew, M.L., Sands, G.B., Hooks, D.A., LeGrice, I.J., and Smaill, B.H. (2009). Three distinct directions of intramural activation reveal nonuniform side-to-side electrical coupling of ventricular myocytes. Circ. Arrhythm. Electrophysiol. *2*, 433–440.

Campbell, N.A., Mitchell, L.G., and Reece, J.B. (2003). Biology : concepts & connections.

Carbonell-Pascual, B., Godoy, E., Ferrer, A., Romero, L., and Ferrero, J.M. (2016). Comparison between Hodgkin–Huxley and Markov formulations of cardiac ion channels. J. Theor. Biol. *399*, 92–102.

Cardiac Arrhythmia Suppression Trial II Investigators (1992). Effect of the antiarrhythmic agent moricizine on survival after myocardial infarction. N. Engl. J. Med. *327*, 227–233.

Cardone-Noott, L., Bueno-Orovio, A., Mincholé, A., Zemzemi, N., and Rodriguez, B. (2016). Human ventricular activation sequence and the simulation of the electrocardiographic QRS complex and its variability in healthy and intraventricular block conditions. Europace *18*, iv4–iv15.

Carmeliet, E. (1999). Cardiac ionic currents and acute ischemia: from channels to arrhythmias. Physiol. Rev. *79*, 917–1017.

Carusi, A., Burrage, K., and Rodríguez, B. (2012). Bridging experiments, models and simulations: an integrative approach to validation in computational cardiac electrophysiology. Am. J. Physiol. Heart Circ. Physiol. *303*, H144-155.

Chan, M.Y., Sun, J.L., Newby, L.K., Shaw, L.K., Lin, M., Peterson, E.D., Califf, R.M., Kong, D.F., and Roe, M.T. (2009). Long-Term Mortality of Patients Undergoing Cardiac Catheterization for ST-Elevation and Non-ST-Elevation Myocardial Infarction. Circulation *119*, 3110–3117.

Chen, Y.-L., Hang, C.-L., Fang, H.-Y., Tsai, T.-H., Sun, C.-K., Chen, C.-J., Chen, S.-M., Yang, C.-H., Hsieh, Y.-K., Wu, C.-J., et al. (2011). Comparison of prognostic outcome between left circumflex artery-related and right coronary artery-related acute inferior wall myocardial infarction undergoing primary percutaneous coronary intervention. Clin. Cardiol. *34*, 249–253.

Cheng, J., Kamiya, K., Liu, W., Tsuji, Y., Toyama, J., and Kodama, I. (1999). Heterogeneous distribution of the two components of delayed rectifier K+ current: a potential mechanism of the proarrhythmic effects of methanesulfonanilideclass III agents. Cardiovasc. Res. *43*, 135–147.

Chorro, F.J., Such-Belenguer, L., and López-Merino, V. (2009). Modelos animales de enfermedad cardiovascular. Rev. Esp. Cardiol. Engl. Ed. *62*, 69–84.

Ciaccio, E.J., Ashikaga, H., Kaba, R.A., Cervantes, D., Hopenfeld, B., Wit, A.L., Peters, N.S., McVeigh, E.R., Garan, H., and Coromilas, J. (2007). Model of reentrant ventricular tachycardia based on infarct border zone geometry predicts reentrant circuit features as determined by activation mapping. Heart Rhythm *4*, 1034–1045.

Ciaccio, E.J., Coromilas, J., Ashikaga, H., Cervantes, D.O., Wit, A.L., Peters, N.S., McVeigh, E.R., and Garan, H. (2015). Model of unidirectional block formation leading to reentrant ventricular tachycardia in the infarct border zone of postinfarction canine hearts. Comput. Biol. Med. *62*, 254–263.

Clauss, S., Bleyer, C., Schüttler, D., Tomsits, P., Renner, S., Klymiuk, N., Wakili, R., Massberg, S., Wolf, E., and Kääb, S. (2019). Animal models of arrhythmia: classic electrophysiology to genetically modified large animals. Nat. Rev. Cardiol. *16*, 457–475.

Colonna, P., Cadeddu, C., Montisci, R., Chen, L., Meloni, L., and Iliceto, S. (2000). Transmural heterogeneity of myocardial contraction and ischemia. Diagnosis and clinical implications. Ital. Heart J. Off. J. Ital. Fed. Cardiol. *1*, 174–183.

Cooper, J.K. (1986). Electrocardiography 100 years ago. Origins, pioneers, and contributors. N. Engl. J. Med. *315*, 461–464.

Cooper, J., Corrias, A., Gavaghan, D., and Noble, D. (2011). Considerations for the use of cellular electrophysiology models within cardiac tissue simulations. Prog. Biophys. Mol. Biol. *107*, 74–80.

Coronel, R., Fiolet, J.W., Wilms-Schopman, F.J., Schaapherder, A.F., Johnson, T.A., Gettes, L.S., and Janse, M.J. (1988). Distribution of extracellular potassium and its relation to electrophysiologic changes during acute myocardial ischemia in the isolated perfused porcine heart. Circulation *77*, 1125–1138.

Coronel, R., Wilms-Schopman, F.J., Opthof, T., van Capelle, F.J., and Janse, M.J. (1991). Injury current and gradients of diastolic stimulation threshold, TQ potential, and extracellular potassium concentration during acute regional ischemia in the isolated perfused pig heart. Circ. Res. *68*, 1241–1249.

Coronel, R., Wilms-Schopman, F.J., Dekker, L.R., and Janse, M.J. (1995). Heterogeneities in [K+]o and TQ potential and the inducibility of ventricular fibrillation during acute regional ischemia in the isolated perfused porcine heart. Circulation *92*, 120–129.

Coronel, R., Casini, S., Koopmann, T.T., Wilms-Schopman, F.J.G., Verkerk, A.O., de Groot, J.R., Bhuiyan, Z., Bezzina, C.R., Veldkamp, M.W., Linnenbank, A.C., et al. (2005). Right ventricular fibrosis and conduction delay in a patient with clinical signs of Brugada syndrome: a combined electrophysiological, genetic, histopathologic, and computational study. Circulation *112*, 2769–2777.

Crumb, W.J., Vicente, J., Johannesen, L., and Strauss, D.G. (2016). An evaluation of 30 clinical drugs against the comprehensive in vitro proarrhythmia assay (CiPA) proposed ion channel panel. J. Pharmacol. Toxicol. Methods *81*, 251–262.

Dagres, N., and Hindricks, G. (2017). Sudden Cardiac Death in Acute Coronary Syndromes. Card. Electrophysiol. Clin. *9*, 725–730.

Decker, K.F., Heijman, J., Silva, J.R., Hund, T.J., and Rudy, Y. (2009). Properties and ionic mechanisms of action potential adaptation, restitution, and accommodation in canine epicardium. Am. J. Physiol. Heart Circ. Physiol. *296*, H1017-1026.

Deschênes, I., Baroudi, G., Berthet, M., Barde, I., Chalvidan, T., Denjoy, I., Guicheney, P., and Chahine, M. (2000). Electrophysiological characterization of SCN5A mutations causing long QT (E1784K) and Brugada (R1512W and R1432G) syndromes. Cardiovasc. Res. *46*, 55–65.

Dijkstra, E.W. (1959). A note on two problems in connexion with graphs. Numer. Math. *1*, 269–271.

Downar, E., Janse, M.J., and Durrer, D. (1977). The effect of acute coronary artery occlusion on subepicardial transmembrane potentials in the intact porcine heart. Circulation *56*, 217–224.

Dumaine Robert, Towbin Jeffrey A., Brugada Pedro, Vatta Matteo, Nesterenko Dmitri V., Nesterenko Vladislav V., Brugada Josep, Brugada Ramon, and Antzelevitch Charles (1999). Ionic Mechanisms Responsible for the Electrocardiographic Phenotype of the Brugada Syndrome Are Temperature Dependent. Circ. Res. *85*, 803–809.

Durrer, D., Dam, R.T.V., Freud, G.E., Janse, M.J., Meijler, F.L., and Arzbaecher, R.C. (1970). Total Excitation of the Isolated Human Heart. Circulation *41*, 899–912.

Dutta, S., Mincholé, A., Zacur, E., Quinn, T.A., Taggart, P., and Rodriguez, B. (2016). Early afterdepolarizations promote transmural reentry in ischemic human ventricles with reduced repolarization reserve. Prog. Biophys. Mol. Biol. *120*, 236–248.

Dutta, S., Mincholé, A., Quinn, T.A., and Rodriguez, B. (2017). Electrophysiological properties of computational human ventricular cell action potential models under acute ischemic conditions. Prog. Biophys. Mol. Biol. *129*, 40–52.

Echt, D.S., Liebson, P.R., Mitchell, L.B., Peters, R.W., Obias-Manno, D., Barker, A.H., Arensberg, D., Baker, A., Friedman, L., and Greene, H.L. (1991). Mortality and morbidity in patients receiving encainide, flecainide, or placebo. The Cardiac Arrhythmia Suppression Trial. N. Engl. J. Med. *324*, 781–788.

Ellinor, P.T., Nam, E.G., Shea, M.A., Milan, D.J., Ruskin, J.N., and MacRae, C.A. (2008). Cardiac sodium channel mutation in atrial fibrillation. Heart Rhythm *5*, 99–105.

European Heart Network (2017). CVD Statistics 2017.

Ferrero, J.M., Sáiz, J., Ferrero, J.M., and Thakor, N.V. (1996). Simulation of action potentials from metabolically impaired cardiac myocytes. Role of ATP-sensitive K+ current. Circ. Res. *79*, 208–221.

Ferrero, J.M., Trénor, B., Rodríguez, B., and Sáiz, J. (2003). Electrical activity and reentry during acute regional myocardial ischemia: insights from simulations. Int. J. Bifurc. Chaos *13*, 3703–3715.

Fronza, M., Raineri, C., Valentini, A., Bassi, E.M., Scelsi, L., Buscemi, M.L., Turco, A., Castelli, G., Ghio, S., and Visconti, L.O. (2016). Relationship between electrocardiographic findings and Cardiac Magnetic Resonance phenotypes in patients with Hypertrophic Cardiomyopathy. IJC Heart Vasc. *11*, 7–11.

Frustaci, A., Priori, S.G., Pieroni, M., Chimenti, C., Napolitano, C., Rivolta, I., Sanna, T., Bellocci, F., and Russo, M.A. (2005). Cardiac histological substrate in patients with clinical phenotype of Brugada syndrome. Circulation *112*, 3680–3687.

Gaborit, N., Le Bouter, S., Szuts, V., Varro, A., Escande, D., Nattel, S., and Demolombe, S. (2007). Regional and tissue specific transcript signatures of ion channel genes in the non-diseased human heart. J. Physiol. *582*, 675–693.

Gemmell, P., Burrage, K., Rodríguez, B., and Quinn, T.A. (2016). Rabbit-specific computational modelling of ventricular cell electrophysiology: Using populations of models to explore variability in the response to ischemia. Prog. Biophys. Mol. Biol. *121*, 169–184.

Ghuran, A.V., and Camm, A.J. (2001). Ischaemic heart disease presenting as arrhythmias. Br. Med. Bull. *59*, 193–210.

Gilbert, S.H., Benson, A.P., Li, P., and Holden, A.V. (2007). Regional localisation of left ventricular sheet structure: integration with current models of cardiac fibre, sheet and band structure. Eur. J. Cardiothorac. Surg. *32*, 231–249.

Goldberger, A.L., Amaral, L.A.N., Glass, L., Hausdorff, J.M., Ivanov, P.C., Mark, R.G., Mietus, J.E., Moody, G.B., Peng, C.-K., and Stanley, H.E. (2000). PhysioBank, PhysioToolkit, and PhysioNet. Circulation *101*, e215–e220.

Gottlieb, S.O., Weisfeldt, M.L., Ouyang, P., Mellits, E.D., and Gerstenblith, G. (1986). Silent Ischemia as a Marker for Early Unfavorable Outcomes in Patients with Unstable Angina. N. Engl. J. Med. *314*, 1214–1219.

Gottlieb, S.O., Gottlieb, S.H., Achuff, S.C., Baumgardner, R., Mellits, E.D., Weisfeldt, M.L., and Gerstenblith, G. (1988). Silent ischemia on Holter monitoring predicts mortality in high-risk postinfarction patients. JAMA *259*, 1030–1035.

Grandi, E., Pandit, S.V., Voigt, N., Workman, A.J., Dobrev, D., Jalife, J., and Bers, D.M. (2011). Human atrial action potential and Ca2+ model: sinus rhythm and chronic atrial fibrillation. Circ. Res. *109*, 1055–1066.

Greenberg, H.M., Dwyer, E.M., Hochman, J.S., Steinberg, J.S., Echt, D.S., and Peters, R.W. (1995). Interaction of ischaemia and encainide/flecainide treatment: a proposed mechanism for the increased mortality in CAST I. Br. Heart J. *74*, 631–635.

Guo, D., Liu, Q., Liu, T., Elliott, G., Gingras, M., Kowey, P.R., and Yan, G.-X. (2011). Electrophysiological properties of HBI-3000: a new antiarrhythmic agent with multiple-channel blocking properties in human ventricular myocytes. J. Cardiovasc. Pharmacol. *57*, 79–85.

Hasche, E.T., Fernandes, C., Freedman, S.B., and Jeremy, R.W. (1995). Relation Between Ischemia Time, Infarct Size, and Left Ventricular Function in Humans. Circulation *92*, 710–719.

Herring, N., and Paterson, D.J. (2006). ECG diagnosis of acute ischaemia and infarction: past, present and future. QJM Int. J. Med. *99*, 219–230.

Hodgkin, A.L., and Huxley, A.F. (1952a). A quantitative description of membrane current and its application to conduction and excitation in nerve. J. Physiol. *117*, 500–544.

Hodgkin, A.L., and Huxley, A.F. (1952b). Currents carried by sodium and potassium ions through the membrane of the giant axon of Loligo. J. Physiol. *116*, 449–472.

Hodgkin, A.L., and Huxley, A.F. (1952c). The components of membrane conductance in the giant axon of Loligo. J. Physiol. *116*, 473–496.

Hodgkin, A.L., and Huxley, A.F. (1952d). The dual effect of membrane potential on sodium conductance in the giant axon of Loligo. J. Physiol. *116*, 497.

Hodgkin, A.L., Huxley, A.F., and Katz, B. (1952). Measurement of current-voltage relations in the membrane of the giant axon of Loligo. J. Physiol. *116*, 424–448.

Hondeghem, L.M., and Katzung, B.G. (1984). Antiarrhythmic agents: the modulated receptor mechanism of action of sodium and calcium channel-blocking drugs. Annu. Rev. Pharmacol. Toxicol. *24*, 387–423.

Hu, D., Viskin, S., Oliva, A., Carrier, T., Cordeiro, J.M., Barajas-Martinez, H., Wu, Y., Burashnikov, E., Sicouri, S., Brugada, R., et al. (2007). Novel mutation in the SCN5A gene associated with arrhythmic storm developing during acute myocardial infarction. Heart Rhythm Off. J. Heart Rhythm Soc. *4*, 1072–1080.

Hund, T.J., and Rudy, Y. (2004). Rate dependence and regulation of action potential and calcium transient in a canine cardiac ventricular cell model. Circulation *110*, 3168–3174.

Hundley, W.G., Rerkpattanapipat, P., Little, W.C., Link, K.M., and Morgan, T.M. (2003). Relation of cardiac prognosis to segment location with apical left ventricular ischemia. Am. J. Cardiol. *92*, 1206–1208.

Ignarro, L.J., Balestrieri, M.L., and Napoli, C. (2007). Nutrition, physical activity, and cardiovascular disease: An update. Cardiovasc. Res. *73*, 326–340.

Irisawa, H., and Sato, R. (1986). Intra- and extracellular actions of proton on the calcium current of isolated guinea pig ventricular cells. Circ. Res. *59*, 348–355.

Jager, F., Taddei, A., Moody, G.B., Emdin, M., Antolič, G., Dorn, R., Smrdel, A., Marchesi, C., and Mark, R.G. (2003). Long-term ST database: A reference for the development and evaluation of automated ischaemia detectors and for the study of the dynamics of myocardial ischaemia. Med. Biol. Eng. Comput. *41*, 172–182.

Janse, M.J., and Kléber, A.G. (1981). Electrophysiological changes and ventricular arrhythmias in the early phase of regional myocardial ischemia. Circ. Res. *49*, 1069–1081.

Janse, M.J., and Wit, A.L. (1989). Electrophysiological mechanisms of ventricular arrhythmias resulting from myocardial ischemia and infarction. Physiol. Rev. *69*, 1049–1169.

Janse, M.J., van Capelle, F.J., Morsink, H., Kléber, A.G., Wilms-Schopman, F., Cardinal, R., d'Alnoncourt, C.N., and Durrer, D. (1980). Flow of "injury" current and patterns of excitation during early ventricular arrhythmias in acute regional myocardial ischemia in isolated porcine and canine hearts. Evidence for two different arrhythmogenic mechanisms. Circ. Res. *47*, 151–165.

Jie, X., and Trayanova, N.A. (2010). Mechanisms for initiation of reentry in acute regional ischemia phase 1B. Heart Rhythm *7*, 379–386.

John, R.M., Tedrow, U.B., Koplan, B.A., Albert, C.M., Epstein, L.M., Sweeney, M.O., Miller, A.L., Michaud, G.F., and Stevenson, W.G. (2012). Ventricular arrhythmias and sudden cardiac death. The Lancet *380*, 1520–1529.

Kagiyama, Y., Hill, J.L., and Gettes, L.S. (1982). Interaction of acidosis and increased extracellular potassium on action potential characteristics and conduction in guinea pig ventricular muscle. Circ. Res. *51*, 614–623.

Kalarus, Z., Svendsen, J.H., Capodanno, D., Dan, G.-A., De Maria, E., Gorenek, B., Jędrzejczyk-Patej, E., Mazurek, M., Podolecki, T., Sticherling, C., et al. (2019). Cardiac arrhythmias in the emergency settings of acute coronary syndrome and revascularization: an European Heart Rhythm Association (EHRA) consensus document, endorsed by the European Association of Percutaneous Cardiovascular Interventions (EAPCI), and European Acute Cardiovascular Care Association (ACCA). EP Eur. *21*, 1603–1604.

Kalla, M., Herring, N., and Paterson, D.J. (2016). Cardiac sympatho-vagal balance and ventricular arrhythmia. Auton. Neurosci. *199*, 29–37.

Kannel, W.B., Cupples, L.A., and D'Agostino, R.B. (1987). Sudden death risk in overt coronary heart disease: The Framingham Study. Am. Heart J. *113*, 799–804.

Kawano, Y., Takemoto, M., Mito, T., Morisaki, H., Tanaka, A., Sakaki, Y., Matsuo, A., Abe, K., Hida, S., Mukae, K., et al. (2016). Silent myocardial ischemia in asymptomatic patients with type 2 diabetes mellitus without previous histories of cardiovascular disease. Int. J. Cardiol. *216*, 151–155.

Kim, T.D., le Coutre, P., Schwarz, M., Grille, P., Levitin, M., Fateh-Moghadam, S., Giles, F.J., Dörken, B., Haverkamp, W., and Köhncke, C. (2012). Clinical cardiac safety profile of nilotinib. Haematologica *97*, 883–889.

Kim Young-Hoon, Xie Fagen, Yashima Masaaki, Wu Tsu-Juey, Valderrábano Miguel, Lee Moon-Hyoung, Ohara Toshihiko, Voroshilovsky Olga, Doshi Rahul N., Fishbein Michael C., et al. (1999). Role of Papillary Muscle in the Generation and Maintenance of Reentry During Ventricular Tachycardia and Fibrillation in Isolated Swine Right Ventricle. Circulation *100*, 1450–1459.

Klabunde, R.E. (2011). Cardiovascular Physiology Concepts.

Kléber, A.G. (2000). ST-segment elevation in the electrocardiogram: a sign of myocardial ischemia. Cardiovasc. Res. *45*, 111–118.

Kloth, J.S.L., Pagani, A., Verboom, M.C., Malovini, A., Napolitano, C., Kruit, W.H.J., Sleijfer, S., Steeghs, N., Zambelli, A., and Mathijssen, R.H.J. (2015). Incidence and relevance of QTc-interval prolongation caused by tyrosine kinase inhibitors. Br. J. Cancer *112*, 1011–1016.

Kobayashi, N., and Maehara, A. (2019). Left anterior descending artery wrapping around the left ventricular apex predicts additional risk of future events after anterior myocardial infarction. Anatol. J. Cardiol. *21*, 259–260.

Kodama, I., Wilde, A., Janse, M.J., Durrer, D., and Yamada, K. (1984). Combined effects of hypoxia, hyperkalemia and acidosis on membrane action potential and excitability of guinea-pig ventricular muscle. J. Mol. Cell. Cardiol. *16*, 247–259.

Kral, B.G., Becker, D.M., Vaidya, D., Yanek, L.R., and Becker, L.C. (2012). Severity of inducible myocardial ischemia predicts incident acute coronary syndromes in asymptomatic individuals with a family history of premature coronary artery disease. J. Nucl. Cardiol. *19*, 28–36.

Kramer, J., Obejero-Paz, C.A., Myatt, G., Kuryshev, Y.A., Bruening-Wright, A., Verducci, J.S., and Brown, A.M. (2013). MICE models: superior to the HERG model in predicting Torsade de Pointes. Sci. Rep. *3*, 2100.

Kühl, J.T., Linde, J.J., Køber, L., Kelbæk, H., and Kofoed, K.F. (2015). The Transmural Extent and Severity of Myocardial Hypoperfusion Predicts Long-Term Outcome in NSTEMI: An MDCT Study. JACC Cardiovasc. Imaging *8*, 684–694.

Kujime, S., Sakurada, H., Saito, N., Enomoto, Y., Ito, N., Nakamura, K., Fukamizu, S., Tejima, T., Yambe, Y., Nishizaki, M., et al. (2017). Outcomes of Brugada Syndrome Patients with Coronary Artery Vasospasm. Intern. Med. *56*, 129–135.

Laguna, P., and Sörnmo, L. (2014). The STAFF III ECG database and its significance for methodological development and evaluation. J. Electrocardiol. *47*, 408–417.

Lau, D.H., Clausen, C., Sosunov, E.A., Shlapakova, I.N., Anyukhovsky, E.P., Danilo, P., Rosen, T.S., Kelly, C., Duffy, H.S., Szabolcs, M.J., et al. (2009). Epicardial border zone overexpression of skeletal muscle sodium channel SkM1 normalizes activation, preserves conduction, and suppresses ventricular arrhythmia: an in silico, in vivo, in vitro study. Circulation *119*, 19–27.

Lee, C.O., and Fozzard, H.A. (1975). Activities of potassium and sodium ions in rabbit heart muscle. J. Gen. Physiol. *65*, 695–708.

Lee, J.T., Ideker, R.E., and Reimer, K.A. (1981). Myocardial infarct size and location in relation to the coronary vascular bed at risk in man. Circulation *64*, 526–534.

Lei Ming, Wu Lin, Terrar Derek A., and Huang Christopher L.-H. (2018). Modernized Classification of Cardiac Antiarrhythmic Drugs. Circulation *138*, 1879–1896.

Letsas, K.P., Asvestas, D., Vlachos, K., Karlis, D., Korantzopoulos, P., Efremidis, M., and Sideris, A. (2014). Electrocardiographic characteristics of premature ventricular contractions in subjects with type 1 pattern of Brugada syndrome. J. Electrocardiol. *47*, 351–355.

Li, Q., Huang, H., Liu, G., Lam, K., Rutberg, J., Green, M.S., Birnie, D.H., Lemery, R., Chahine, M., and Gollob, M.H. (2009). Gain-of-function mutation of Nav1.5 in atrial fibrillation enhances cellular excitability and lowers the threshold for action potential firing. Biochem. Biophys. Res. Commun. *380*, 132–137.

Livshitz, L.M., and Rudy, Y. (2007). Regulation of Ca2+ and electrical alternans in cardiac myocytes: role of CAMKII and repolarizing currents. Am. J. Physiol. Heart Circ. Physiol. *292*, H2854-2866.

Lloyd, C.M., Halstead, M.D.B., and Nielsen, P.F. (2004). CellML: its future, present and past. Prog. Biophys. Mol. Biol. *85*, 433–450.

Luo, C.H., and Rudy, Y. (1991). A model of the ventricular cardiac action potential. Depolarization, repolarization, and their interaction. Circ. Res. *68*, 1501–1526.

Luo, C.H., and Rudy, Y. (1994). A dynamic model of the cardiac ventricular action potential. I. Simulations of ionic currents and concentration changes. Circ. Res. *74*, 1071–1096.

Luqman, N., Sung, R.J., Wang, C.-L., and Kuo, C.-T. (2007). Myocardial ischemia and ventricular fibrillation: pathophysiology and clinical implications. Int. J. Cardiol. *119*, 283–290.

Madsen, J.K. (1985). Ischaemic heart disease and prodromes of sudden cardiac death. Is it possible to identify high risk groups for sudden cardiac death? Heart *54*, 27–32.

Mahajan, A., Shiferaw, Y., Sato, D., Baher, A., Olcese, R., Xie, L.-H., Yang, M.-J., Chen, P.-S., Restrepo, J.G., Karma, A., et al. (2008). A rabbit ventricular action potential model replicating cardiac dynamics at rapid heart rates. Biophys. J. *94*, 392–410.

Makiyama, T., Akao, M., Shizuta, S., Doi, T., Nishiyama, K., Oka, Y., Ohno, S., Nishio, Y., Tsuji, K., Itoh, H., et al. (2008). A Novel SCN5A Gain-of-Function Mutation M1875T Associated With Familial Atrial Fibrillation. J. Am. Coll. Cardiol. *52*, 1326–1334.

Maleckar, M.M., Greenstein, J.L., Giles, W.R., and Trayanova, N.A. (2009). Electrotonic coupling between human atrial myocytes and fibroblasts alters myocyte excitability and repolarization. Biophys. J. *97*, 2179–2190.

Maltsev, V.A., Sabbah, H.N., Higgins, R.S., Silverman, N., Lesch, M., and Undrovinas, A.I. (1998). Novel, ultraslow inactivating sodium current in human ventricular cardiomyocytes. Circulation *98*, 2545–2552.

Martinez, M.E., Walton, R.D., Bayer, J.D., Haïssaguerre, M., Vigmond, E.J., Hocini, M., and Bernus, O. (2018). Role of the Purkinje-Muscle Junction on the Ventricular Repolarization Heterogeneity in the Healthy and Ischemic Ovine Ventricular Myocardium. Front. Physiol. *9*.

Masci, P.G., Ganame, J., Francone, M., Desmet, W., Lorenzoni, V., Iacucci, I., Barison, A., Carbone, I., Lombardi, M., Agati, L., et al. (2011). Relationship between location and size of myocardial infarction and their reciprocal influences on post-infarction left ventricular remodelling. Eur. Heart J. *32*, 1640–1648.

Mather (Editor), P.J. (2010). Jefferson Heart Institute Handbook Of Cardiology (Jones & Bartlett Publishers).

McIntyre, H., and Fry, C.H. (1997). Abnormal action potential conduction in isolated human hypertrophied left ventricular myocardium. J. Cardiovasc. Electrophysiol. *8*, 887–894.

Meier, P., Schirmer, S.H., Lansky, A.J., Timmis, A., Pitt, B., and Seiler, C. (2013). The collateral circulation of the heart. BMC Med. *11*, 143.

Menting, M.E., and van Mechelen, R. (2012). Sinus rhythm with an isolated ST-segment elevation in V2. Neth. Heart J. *20*, 478–479.

Meregalli, P.G., Wilde, A.A.M., and Tan, H.L. (2005). Pathophysiological mechanisms of Brugada syndrome: depolarization disorder, repolarization disorder, or more? Cardiovasc. Res. *67*, 367–378.

Michailova, A., Saucerman, J., Belik, M.E., and McCulloch, A.D. (2005). Modeling Regulation of Cardiac KATP and L-type Ca2+ Currents by ATP, ADP, and Mg2+. Biophys. J. *88*, 2234–2249.

Moréna, H., Janse, M.J., Fiolet, J.W., Krieger, W.J., Crijns, H., and Durrer, D. (1980). Comparison of the effects of regional ischemia, hypoxia, hyperkalemia, and acidosis on intracellular and extracellular potentials and metabolism in the isolated porcine heart. Circ. Res. *46*, 634–646.

Moreno, J.D., Zhu, Z.I., Yang, P.-C., Bankston, J.R., Jeng, M.-T., Kang, C., Wang, L., Bayer, J.D., Christini, D.J., Trayanova, N.A., et al. (2011). A computational model to predict the effects of class I anti-arrhythmic drugs on ventricular rhythms. Sci. Transl. Med. *3*, 98ra83.

Morita, H., Fukushima-Kusano, K., Nagase, S., Takenaka-Morita, S., Nishii, N., Kakishita, M., Nakamura, K., Emori, T., Matsubara, H., and Ohe, T. (2003). Site-specific arrhythmogenesis in patients with Brugada syndrome. J. Cardiovasc. Electrophysiol. *14*, 373–379.

Näbauer, M., Beuckelmann, D.J., Überfuhr, P., and Steinbeck, G. (1996). Regional Differences in Current Density and Rate-Dependent Properties of the Transient Outward Current in Subepicardial and Subendocardial Myocytes of Human Left Ventricle. Circulation.

Nagatomo, T., Fan, Z., Ye, B., Tonkovich, G.S., January, C.T., Kyle, J.W., and Makielski, J.C. (1998). Temperature dependence of early and late currents in human cardiac wild-type and long Q-T DeltaKPQ Na+ channels. Am. J. Physiol. *275*, H2016-2024.

Nair, K., Umapathy, K., Farid, T., Masse, S., Mueller, E., Sivanandan, R.V., Poku, K., Rao, V., Nair, V., Butany, J., et al. (2011). Intramural activation during early human ventricular fibrillation. Circ. Arrhythm. Electrophysiol. *4*, 692–703.

Niederer, S.A., and Smith, N.P. (2007). A mathematical model of the slow force response to stretch in rat ventricular myocytes. Biophys. J. *92*, 4030–4044.

Niederer, S.A., Kerfoot, E., Benson, A.P., Bernabeu, M.O., Bernus, O., Bradley, C., Cherry, E.M., Clayton, R., Fenton, F.H., Garny, A., et al. (2011). Verification of cardiac tissue electrophysiology simulators using an N-version benchmark. Philos. Transact. A Math. Phys. Eng. Sci. *369*, 4331–4351.

Noble, D. (1962). A modification of the Hodgkin—Huxley equations applicable to Purkinje fibre action and pacemaker potentials. J. Physiol. *160*, 317–352.

Noble, D. (2011). Successes and failures in modeling heart cell electrophysiology. Heart Rhythm *8*, 1798–1803.

Noble, D., and Rudy, Y. (2001). Models of cardiac ventricular action potentials: iterative interaction between experiment and simulation. Philos. Trans. R. Soc. Lond. Math. Phys. Eng. Sci. *359*, 1127–1142.

Noma, A. (1983). ATP-regulated K+ channels in cardiac muscle. Nature *305*, 147–148.

Nygren, A., Olson, M.L., Chen, K.Y., Emmett, T., Kargacin, G., and Shimoni, Y. (2007). Propagation of the cardiac impulse in the diabetic rat heart: reduced conduction reserve. J. Physiol. *580*, 543–560.

Odutayo, A., Wong, C.X., Hsiao, A.J., Hopewell, S., Altman, D.G., and Emdin, C.A. (2016). Atrial fibrillation and risks of cardiovascular disease, renal disease, and death: systematic review and meta-analysis. BMJ *354*, i4482.

O'Hara, T., Virág, L., Varró, A., and Rudy, Y. (2011). Simulation of the undiseased human cardiac ventricular action potential: model formulation and experimental validation. PLoS Comput. Biol. *7*, e1002061.

Osadchii, O.E. (2017). Effects of Na+ channel blockers on the restitution of refractory period, conduction time, and excitation wavelength in perfused guinea-pig heart. PloS One *12*, e0172683.

Parikh Nisha I., Honeycutt Emily F., Roe Matthew T., Neely Megan, Rosenthal Eric J., Mittleman Murray A., Carrozza Joseph P., and Ho Kalon K.L. (2012). Left and Codominant Coronary Artery Circulations Are Associated With Higher In-Hospital Mortality Among Patients Undergoing Percutaneous Coronary Intervention for Acute Coronary Syndromes. Circ. Cardiovasc. Qual. Outcomes *5*, 775–782.

Park, K.E., and Richard Conti, C. (2016). Prognostic Significance of Asymptomatic Myocardial Ischemia in Women vs. Men. Curr. Pharm. Des. *22*, 3871–3876.

Passini, E., Mincholé, A., Coppini, R., Cerbai, E., Rodriguez, B., Severi, S., and Bueno-Orovio, A. (2016). Mechanisms of pro-arrhythmic abnormalities in ventricular repolarisation and anti-arrhythmic therapies in human hypertrophic cardiomyopathy. J. Mol. Cell. Cardiol. *96*, 72–81.

Passini, E., Britton, O.J., Lu, H.R., Rohrbacher, J., Hermans, A.N., Gallacher, D.J., Greig, R.J.H., Bueno-Orovio, A., and Rodriguez, B. (2017). Human In Silico Drug Trials Demonstrate Higher Accuracy than Animal Models in Predicting Clinical Pro-Arrhythmic Cardiotoxicity. Front. Physiol. *8*, 668.

Pasvolsky, O., Leader, A., Iakobishvili, Z., Wasserstrum, Y., Kornowski, R., and Raanani, P. (2015). Tyrosine kinase inhibitor associated vascular toxicity in chronic myeloid leukemia. Cardio-Oncol. *1*, 5.

Pathmanathan, P., Bernabeu, M.O., Bordas, R., Cooper, J., Garny, A., Pitt-Francis, J.M., Whiteley, J.P., and Gavaghan, D.J. (2010). A numerical guide to the solution of the bi-domain equations of cardiac electrophysiology. Prog. Biophys. Mol. Biol. *102*, 136–155.

Penny, W.J., and Sheridan, D.J. (1983). Arrhythmias and cellular electrophysiological changes during myocardial "ischaemia" and reperfusion. Cardiovasc. Res. *17*, 363–372.

Pettersson, J., Carro, E., Edenbrandt, L., Maynard, C., Pahlm, O., Ringborn, M., Sörnmo, L., Warren, S.G., and Wagner, G.S. (2000). Spatial, individual, and temporal variation of the high-frequency QRS amplitudes in the 12 standard electrocardiographic leads. Am. Heart J. *139*, 352–358.

Pionkowski, R.S., Thompson, B.M., Gruchow, H.W., Aprahamian, C., and Darin, J.C. (1983). Resuscitation time in ventricular fibrillation — a prognostic indicator. Ann. Emerg. Med. *12*, 733–738.

Pitt-Francis, J., Bernabeu, M.O., Cooper, J., Garny, A., Momtahan, L., Osborne, J., Pathmanathan, P., Rodriguez, B., Whiteley, J.P., and Gavaghan, D.J. (2008). Chaste: using agile programming techniques to develop computational biology software. Philos. Transact. A Math. Phys. Eng. Sci. *366*, 3111–3136.

Pollard, A.E., Cascio, W.E., Fast, V.G., and Knisley, S.B. (2002). Modulation of triggered activity by uncoupling in the ischemic borderA model study with phase 1b-like conditions. Cardiovasc. Res. *56*, 381–392.

Potse, M., LeBlanc, A.R., Cardinal, R., and Vinet, A. (2006). ST elevation or depression in subendocardial ischemia? In 2006 International Conference of the IEEE Engineering in Medicine and Biology Society, pp. 3899–3902.

Pratt, C.M., Camm, A.J., Cooper, W., Friedman, P.L., MacNeil, D.J., Moulton, K.M., Pitt, B., Schwartz, P.J., Veltri, E.P., and Waldo, A.L. (1998). Mortality in the Survival With ORal D-sotalol (SWORD) trial: why did patients die? Am. J. Cardiol. *81*, 869–876.

Pueyo, E., Sornmo, L., and Laguna, P. (2008). QRS slopes for detection and characterization of myocardial ischemia. IEEE Trans. Biomed. Eng. *55*, 468–477.

Ramanathan, C., Jia, P., Ghanem, R., Ryu, K., and Rudy, Y. (2006). Activation and repolarization of the normal human heart under complete physiological conditions. Proc. Natl. Acad. Sci. U. S. A. *103*, 6309–6314.

Raphael, C.E., Cooper, R., Parker, K.H., Collinson, J., Vassiliou, V., Pennell, D.J., de Silva, R., Hsu, L.Y., Greve, A.M., Nijjer, S., et al. (2016). Mechanisms of Myocardial Ischemia in Hypertrophic Cardiomyopathy. J. Am. Coll. Cardiol. *68*, 1651–1660.

Regitz-Zagrosek, V. (2011). Sex and gender differences in symptoms of myocardial ischaemia. Eur. Heart J. *32*, 3064–3066.

Remme, C.A. (2013). Cardiac sodium channelopathy associated with SCN5A mutations: electrophysiological, molecular and genetic aspects. J. Physiol. *591*, 4099–4116.

Richardson, W., Clarke, S., Quinn, T., and Holmes, J. (2015). Physiological Implications of Myocardial Scar Structure. Compr. Physiol. *5*, 1877–1909.

Rijnbeek, P.R., van Herpen, G., Bots, M.L., Man, S., Verweij, N., Hofman, A., Hillege, H., Numans, M.E., Swenne, C.A., Witteman, J.C.M., et al. (2014). Normal values of the electrocardiogram for ages 16-90 years. J. Electrocardiol. *47*, 914–921.

Ringborn, M., Romero, D., Pueyo, E., Pahlm, O., Wagner, G.S., Laguna, P., and Platonov, P.G. (2011). Evaluation of depolarization changes during acute myocardial ischemia by analysis of QRS slopes. J. Electrocardiol. *44*, 416–424.

Roden, D.M. (1996). Ionic mechanisms for prolongation of refractoriness and their proarrhythmic and antiarrhythmic correlates. Am. J. Cardiol. *78*, 12–16.

Rodríguez, B., Trayanova, N., and Noble, D. (2006). Modeling cardiac ischemia. Ann. N. Y. Acad. Sci. *1080*, 395–414.

Royer, A., van Veen, T.A.B., Le Bouter, S., Marionneau, C., Griol-Charhbili, V., Léoni, A.-L., Steenman, M., van Rijen, H.V.M., Demolombe, S., Goddard, C.A., et al. (2005). Mouse model of SCN5A-linked hereditary Lenègre's disease: age-related conduction slowing and myocardial fibrosis. Circulation *111*, 1738–1746.

Sager, P.T., Gintant, G., Turner, J.R., Pettit, S., and Stockbridge, N. (2014). Rechanneling the cardiac proarrhythmia safety paradigm: A meeting report from the Cardiac Safety Research Consortium. Am. Heart J. *167*, 292–300.

Sakakibara, Y., Furukawa, T., Singer, D.H., Jia, H., Backer, C.L., Arentzen, C.E., and Wasserstrom, J.A. (1993). Sodium current in isolated human ventricular myocytes. Am. J. Physiol. *265*, H1301-1309.

Salama, G., Lombardi, R., and Elson, J. (1987). Maps of optical action potentials and NADH fluorescence in intact working hearts. Am. J. Physiol. *252*, H384-394.

Samie, F.H., and Jalife, J. (2001). Mechanisms underlying ventricular tachycardia and its transition to ventricular fibrillation in the structurally normal heart. Cardiovasc. Res. *50*, 242–250.

Samson, W.E., and Scher, A.M. (1960). Mechanism of S-T segment alteration during acute myocardial injury. Circ. Res. *8*, 780–787.

Sarafoff, N., Schuster, T., Vochem, R., Fichtner, S., Martinoff, S., Schwaiger, M., Schömig, A., and Ibrahim, T. (2013). Association of ST-elevation and non-ST-elevation presentation on ECG with transmurality and size of myocardial infarction as assessed by contrast-enhanced magnetic resonance imaging. J. Electrocardiol. *46*, 100–106.

Shannon, T.R., Wang, F., Puglisi, J., Weber, C., and Bers, D.M. (2004). A mathematical treatment of integrated Ca dynamics within the ventricular myocyte. Biophys. J. *87*, 3351–3371.

Shattock, M.J., Park, K.C., Yang, H.-Y., Lee, A.W.C., Niederer, S., MacLeod, K.T., and Winter, J. (2017). Restitution slope is principally determined by steady-state action potential duration. Cardiovasc. Res. *113*, 817–828.

Shaw, R.M., and Rudy, Y. (1995). The Vulnerable Window for Unidirectional Block in Cardiac Tissue: J. Cardiovasc. Electrophysiol. *6*, 115–131.

Shaw, R.M., and Rudy, Y. (1997). Electrophysiologic effects of acute myocardial ischemia: a theoretical study of altered cell excitability and action potential duration. Cardiovasc. Res. *35*, 256–272.

Shea, M.J., Deanfield, J.E., Wilson, R., DeLandsheere, C., Jones, T., and Selwyn, A.P. (1985). Transient ischemia in angina pectoris: Frequent silent events with everyday activities. Am. J. Cardiol. *56*, E34–E38.

Shirai, N., Makita, N., Sasaki, K., Yokoi, H., Sakuma, I., Sakurada, H., Akai, J., Kimura, A., Hiraoka, M., and Kitabatake, A. (2002). A mutant cardiac sodium channel with multiple biophysical defects associated with overlapping clinical features of Brugada syndrome and cardiac conduction disease. Cardiovasc. Res. *53*, 348–354.

Smith, J.M., and Cohen, R.J. (1984). Simple finite-element model accounts for wide range of cardiac dysrhythmias. Proc. Natl. Acad. Sci. *81*, 233–237.

Soltysinska, E., Olesen, S.-P., Christ, T., Wettwer, E., Varró, A., Grunnet, M., and Jespersen, T. (2009). Transmural expression of ion channels and transporters in human nondiseased and end-stage failing hearts. Pflugers Arch. *459*, 11–23.

Spach, M.S., and Dolber, P.C. (1986). Relating extracellular potentials and their derivatives to anisotropic propagation at a microscopic level in human cardiac muscle. Evidence for electrical uncoupling of side-to-side fiber connections with increasing age. Circ. Res. *58*, 356–371.

Starmer, C.F., Grant, A.O., and Strauss, H.C. (1984). Mechanisms of use-dependent block of sodium channels in excitable membranes by local anesthetics. Biophys. J. *46*, 15–27.

Starmer, C.F., Lastra, A.A., Nesterenko, V.V., and Grant, A.O. (1991). Proarrhythmic response to sodium channel blockade. Theoretical model and numerical experiments. Circulation *84*, 1364–1377.

Sutton, P., Taggart, P., Opthof, T., Coronel, R., Trimlett, R., Pugsley, W., and Kallis, P. (2000). Repolarisation and refractoriness during early ischaemia in humans. Heart *84*, 365–369.

Szabó, G., Szentandrássy, N., Bíró, T., Tóth, B.I., Czifra, G., Magyar, J., Bányász, T., Varró, A., Kovács, L., and Nánási, P.P. (2005). Asymmetrical distribution of ion channels in canine and human left-ventricular wall: epicardium versus midmyocardium. Pflüg. Arch. *450*, 307–316.

Szentadrassy, N., Banyasz, T., Biro, T., Szabo, G., Toth, B.I., Magyar, J., Lazar, J., Varro, A., Kovacs, L., and Nanasi, P.P. (2005). Apico-basal inhomogeneity in distribution of ion channels in canine and human ventricular myocardium. Cardiovasc. Res. *65*, 851–860.

Taccardi, B. (1963). Distribution of heart potentials on the thoracic surface of normal human subjects. Circ. Res. *12*, 341–352.

Taggart, P., Sutton, P.M., Opthof, T., Coronel, R., Trimlett, R., Pugsley, W., and Kallis, P. (2000). Inhomogeneous transmural conduction during early ischaemia in patients with coronary artery disease. J. Mol. Cell. Cardiol. *32*, 621–630.

Tan, B.-H., Valdivia, C.R., Song, C., and Makielski, J.C. (2006). Partial expression defect for the SCN5A missense mutation G1406R depends on splice variant background Q1077 and rescue by mexiletine. Am. J. Physiol. Heart Circ. Physiol. *291*, H1822-1828.

Ten Tusscher, K.H.W.J., and Panfilov, A.V. (2006). Cell model for efficient simulation of wave propagation in human ventricular tissue under normal and pathological conditions. Phys. Med. Biol. *51*, 6141–6156.

Tice, B.M., Rodríguez, B., Eason, J., and Trayanova, N. (2007). Mechanistic investigation into the arrhythmogenic role of transmural heterogeneities in regional ischaemia phase 1A. Eur. Eur. Pacing Arrhythm. Card. Electrophysiol. J. Work. Groups Card. Pacing Arrhythm. Card. Cell. Electrophysiol. Eur. Soc. Cardiol. *9 Suppl 6*, vi46-58.

Tohse, N. (1990). Calcium-sensitive delayed rectifier potassium current in guinea pig ventricular cells. Am. J. Physiol. *258*, H1200-1207.

Tomek, J., Rodriguez, B., Bub, G., and Heijman, J. (2017). β-Adrenergic receptor stimulation inhibits proarrhythmic alternans in postinfarction border zone cardiomyocytes: a computational analysis. Am. J. Physiol.-Heart Circ. Physiol. *313*, H338–H353.

Trayanova, N.A. (2011). Whole Heart Modeling: Applications to Cardiac Electrophysiology and Electromechanics. Circ. Res. *108*, 113–128.

Trénor, B., Ferrero, J.M., Rodríguez, B., and Montilla, F. (2005). Effects of pinacidil on reentrant arrhythmias generated during acute regional ischemia: a simulation study. Ann. Biomed. Eng. *33*, 897–906.

Tsuka, Y., Sugiura, T., Hatada, K., Nakamura, S., Yuasa, F., and Iwasaka, T. (2001). Clinical significance of ST-segment elevation in lead V1 in patients with acute inferior wall Q-wave myocardial infarction. Am. Heart J. *141*, 615–620.

ten Tusscher, K.H.W.J., Noble, D., Noble, P.J., and Panfilov, A.V. (2004). A model for human ventricular tissue. Am. J. Physiol. Heart Circ. Physiol. *286*, H1573-1589.

Valderrábano, M., Lee, M.H., Ohara, T., Lai, A.C., Fishbein, M.C., Lin, S.F., Karagueuzian, H.S., and Chen, P.S. (2001). Dynamics of intramural and transmural reentry during ventricular fibrillation in isolated swine ventricles. Circ. Res. *88*, 839–848.

Veldkamp, M.W., Viswanathan, P.C., Bezzina, C., Baartscheer, A., Wilde, A.A., and Balser, J.R. (2000). Two distinct congenital arrhythmias evoked by a multidysfunctional Na(+) channel. Circ. Res. *86*, E91-97.

Vincent, G.M., Abildskov, J.A., and Burgess, M.J. (1977). Mechanisms of ischemic ST-segment displacement. Evaluation by direct current recordings. Circulation *56*, 559–566.

Virág, L., Iost, N., Opincariu, M., Szolnoky, J., Szécsi, J., Bogáts, G., Szenohradszky, P., Varró, A., and Papp, J.G. (2001). The slow component of the delayed rectifier potassium current in undiseased human ventricular myocytes. Cardiovasc. Res. *49*, 790–797.

Wagner, S., Dybkova, N., Rasenack, E.C.L., Jacobshagen, C., Fabritz, L., Kirchhof, P., Maier, S.K.G., Zhang, T., Hasenfuss, G., Brown, J.H., et al. (2006). Ca2+/calmodulin-dependent protein kinase II regulates cardiac Na+ channels. J. Clin. Invest. *116*, 3127–3138.

Wake, R., and Yoshiyama, M. (2009). Gender differences in ischemic heart disease. Recent Patents Cardiovasc. Drug Discov. *4*, 234–240.

Wang, J.C., Normand, S.-L.T., Mauri, L., and Kuntz, R.E. (2004). Coronary artery spatial distribution of acute myocardial infarction occlusions. Circulation *110*, 278–284.

Warner, M.J., and Tivakaran, V.S. (2019). Myocardial Infarction, Inferior. In StatPearls, (Treasure Island (FL): StatPearls Publishing), p.

Weerd, J.H. van, and Christoffels, V.M. (2016). The formation and function of the cardiac conduction system. Development *143*, 197–210.

Weiss, J., and Shine, K.I. (1982). [K+]o accumulation and electrophysiological alterations during early myocardial ischemia. Am. J. Physiol. *243*, H318-327.

Weiss, J., and Shine, K.I. (1986). Effects of heart rate on extracellular [K+] accumulation during myocardial ischemia. Am. J. Physiol. *250*, H982-991.

Weiss, D.L., Seemann, G., Keller, D.U.J., Farina, D., Sachse, F.B., and Dössel, O. (2007). Modeling of heterogeneous electrophysiology in the human heart with respect to ECG genesis. In Computers in Cardiology, pp. 49–52.

Weiss, J.N., Qu, Z., Chen, P.-S., Lin, S.-F., Karagueuzian, H.S., Hayashi, H., Garfinkel, A., and Karma, A. (2005). The dynamics of cardiac fibrillation. Circulation *112*, 1232–1240.

Wilensky, R.L., Tranum-Jensen, J., Coronel, R., Wilde, A.A., Fiolet, J.W., and Janse, M.J. (1986). The subendocardial border zone during acute ischemia of the rabbit heart: an electrophysiologic, metabolic, and morphologic correlative study. Circulation *74*, 1137–1146.

Wilhelms, M., Dössel, O., and Seemann, G. (2010). Simulating the impact of the transmural extent of acute ischemia on the electrocardiogram. In 2010 Computing in Cardiology, pp. 13–16.

Wilhelms, M., Dossel, O., and Seemann, G. (2011). In Silico Investigation of Electrically Silent Acute Cardiac Ischemia in the Human Ventricles. IEEE Trans. Biomed. Eng. *58*, 2961–2964.

Wu, J., and Zipes, D.P. (2001). Transmural reentry during acute global ischemia and reperfusion in canine ventricular muscle. Am. J. Physiol. Heart Circ. Physiol. *280*, H2717-2725.

Zellweger, M.J., Weinbacher, M., Zutter, A.W., Jeger, R.V., Mueller-Brand, J., Kaiser, C., Buser, P.T., and Pfisterer, M.E. (2003). Long-term outcome of patients with silent versus symptomatic ischemia six months after percutaneous coronary intervention and stenting. J. Am. Coll. Cardiol. *42*, 33–40.

Zhang, J., Sacher, F., Hoffmayer, K., O'Hara, T., Strom, M., Cuculich, P., Silva, J., Cooper, D., Faddis, M., Hocini, M., et al. (2015). Cardiac electrophysiological substrate underlying the ECG phenotype and electrogram abnormalities in Brugada syndrome patients. Circulation *131*, 1950–1959.

9 ANNEX: SOFTWARE CONTRIBUTIONS

Conducting the research presented in this thesis required more than 800 computer simulations of human cardiac electrophysiology at the whole ventricular level, most of which were used for quantifying ischemia-induced arrhythmic risk. I developed a pipeline for running efficiently these computationally expensive torso/heart studies. Submission of the jobs to supercomputing facilities and postprocessing of the results were implemented in a semi-automatic manner in order to reduce complexity and human error. In this annex, the tools produced for developing the simulation pipeline of human acute myocardial ischemia are presented.

9.1 Software application for multiscale simulations of regional acute myocardial ischemia in human

In the Chaste repository, multiple tutorials and test programs are available, including instructions about how to simulate several examples of cardiac electrophysiology. Particularly relevant are Sara Dutta's and Louie Cardone-Noott's contributions, focused on the modelling of acute myocardial ischemia and of the electrographic signal, respectively.

Before I developed the simulation pipeline, a list of prerequisites was established to satisfy the needs of this work:

- Execution of human cardiac electrophysiology simulations in heart and torso.
- Simulation of the ECG.
- Simulation of phase 1A regional myocardial ischemia.

- Implementation of variability in ischemia: size, transmural extent, location, slow/normal propagation conditions in the remote myocardium.
- Simulation of drug effects, using the simple pore block model.
- The application should not be recompiled for each of the ischemia scenarios simulated.
- Simulations must be conducted in high-performance computing facilities.
- The code should be modular, in case certain components required to be exchanged, especially during the development phase of the model.

The repository containing the source code for the ischemia simulations is based on the following files:

- `TestIschemia.hpp` is the main code for simulations running from scratch. Simulation parameters are read and set in runtime. Required tools and functions are invoked from this code. Finally, the problem is solved, and results are generated.
- `TestIschemiaL.hpp` is the main code for simulations running after loading a checkpoint. Fewer simulation parameters are required since they are loaded from the checkpoint data.
- `GenericVarier.hpp` implements apico-basal heterogeneities, by evaluating the relative position of a node within the myocardial mesh.
- `Dijkstra.hpp` contains all functions required for simulating the fast endocardial conduction system. Files containing distances between mesh nodes are processed in this class, and the function `GetMinimumDistanceFromRootsForNode()` is used for calculating the activation time for each of the endocardial nodes depending on their distance to the activation root nodes.
- `GenericCvodeCellFactory.hpp` derives from the abstract class `AbstractCardiacCellFactory`, which assigns their characteristics to each cell in the model. In this case, each cell is defined with the ORd model, including transmural heterogeneities by defining endocardial, midmyocardial and epicardial characteristics, depending on its relative position within the myocardial wall. Local changes in electrophysiology for simulating acute

regional myocardial ischemia and global changes for simulating drug effects are defined here.

- `PostUpstrokeTimeAdaptivityController.hpp` is a tool for modulating the maximum and minimum integration timestep, depending on the electrical activity in the simulation. When a stimulus is triggered, the allowed timestep range is smaller due to steep changes in the electrophysiological model, since a higher accuracy is required. During the repolarisation phase, when such steep gradients do not longer exist, the integration timestep can increase with negligible effects in accuracy.
- `ORd2011endo_fkatp.cellml`, `ORd2011m_fkatp.cellml` and `ORd2011epi_fkatp.cellml` are CellML files containing the ORd model for endocardial, mid-myocardial and epicardial cardiomyocytes. During compilation, models are read and converted into C++ code to be executed within the simulations.

The code repository and the meshes used for this thesis has been made public on https://doi.org/10.5287/bodleian:9rxjpo9po. However, selected code snippets are shown and commented here:

`TestIschemia.hpp`

```
// GenericVarier constructor for establishing electrophysiological gradients in
myocardium
// Arguments: heart_geometric_info, apicobasal_het, transmural_het, interventricular_het
GenericVarier varier(&heart_geom_info, true, false, false);


// CellFactory constructor
GenericCvodeCellfactory cell_factory(
                      stimulusinfo,  //sinus rhythm or ectopy parameters
                      cellcomposition,  //array with epi, mid, endo ratios
                      "OHaraRudy2011_fkatp",  //cell model
                      "/gpfs/projects/pr1efz00/pr1efz11/" + meshname,  //mesh
                      &varier,  //heterogeneity gradients
                      mesh.rGetNodePermutation(),  //permutation of nodes in mesh
                      lv_root_nodes,  //root nodes LV
                      rv_root_nodes,  //root nodes RV
                      purkinjeV,  //purkinje system CV
                      ischaemia,  //ischemia: yes or no
                      k0,  //extracellular K+ in ischemia
                      ikatp,  //conductance factor for IK(ATP) (ischemia)
                      ina,  //conductance factor for INa and ICaL (ischemia)
                      radius,  //radius of ischemic region
                      xx,  //location of ischemic region: X
                      yy,  //location of ischemic region: Y
                      zz,  //location of ischemic region: Z
                      transmural,  //transmural or subendocardial ischemia
                      factordrug_gNa,  //single pore block model for INa (myocardium)
                      factordrug_gKr,  //single pore block model for IKr (myocardium)
                      factordrug_pCa  //single pore block model for ICaL (myocardium)
);

// Reading ischemia settings from the job submission script
```

```
if ( CommandLineArguments::Instance()->OptionExists("-ischaemia"))
{
            ischaemia = true;
            k0 = CommandLineArguments::Instance()->GetDoubleCorrespondingToOption("-
k0");
            ikatp = CommandLineArguments::Instance()->GetDoubleCorrespondingToOption("-
ikatp");
            ina = CommandLineArguments::Instance()->GetDoubleCorrespondingToOption("-
ina");
            radius = CommandLineArguments::Instance()->GetDoubleCorrespondingToOption("-
radius");
            xx = CommandLineArguments::Instance()->GetDoubleCorrespondingToOption("-x");
            yy = CommandLineArguments::Instance()->GetDoubleCorrespondingToOption("-y");
            zz = CommandLineArguments::Instance()->GetDoubleCorrespondingToOption("-
z");
            transmural = CommandLineArguments::Instance()-
>GetUnsignedCorrespondingToOption("-transmural");
}
```

TestIschemiaL.hpp

```
// Loading checkpoint
BidomainProblem<3> * bidomain_problem =
       CardiacSimulationArchiver<BidomainProblem<3>>::Load("savedsimulation_" +
       loadsim);

// Updating time variables after loading the checkpoint data
lasttime = bidomain_problem->GetCurrentTime();
endTime = lasttime + simduration;
HeartConfig::Instance()->SetSimulationDuration(endTime);
```

GenericCvodeCellFactory.hpp

```
// Implementation of the simple pore block model for INa

// 1. INa conductance is obtained from a specific cell
double get_gNa = p_cell->GetParameter("membrane_fast_sodium_current_conductance");

// 2. INa conductance value is updated after being multiplied by (1-channel_block),
calculated from IC50, nH and therapeutic dose
p_cell->SetParameter("membrane_fast_sodium_current_conductance", get_gNa *
_factordrug_gNa);
```

PostUpstrokeTimeAdaptivityController.hpp

```
// Checking if a sinus rhythm stimulus or ectopic has been programmed for the current
simulation time
if ( (CompareDoubles::IsNearZero(fmod(currentTime, mPacingFrequency), mSmallDt/2)) ||
                (CompareDoubles::IsNearZero(currentTime - mEctopicS2, mSmallDt/2)) )
{
     mAllDepolarisedTime = -1.0;
     mHaveSwitchedTimestep = false;

     // Set dt for all cells to small time step
     const std::vector<AbstractCardiacCellInterface*>& r_cells =
                                        mrProblem.GetTissue()->rGetCellsDistributed();

     // If that is the case, setting small integration timestep in cell models
     for (unsigned i=0; i<r_cells.size(); i++)
     {
          r_cells[i]->SetTimestep(mSmallDt);
     }

}
```

9.2 Submissions of jobs in ARCHER

Quantification of the inducibility of reentries required a large amount of computationally costly simulations run in the UK and Spanish national supercomputing facilities. The simultaneous launch of multiple computer simulations was key for the feasibility of the studies presented here. Several scripts were programmed to generate jobs to be submitted to the supercomputer processing queues. Thanks to those scripts, the only requirement to execute simulations was the systematic submission of jobs. For this purpose, the simulation executable must be previously compiled and available in the supercomputer.

I have used the same executable for every ischemia simulation, based on the code described in the previous section. Ischemia variability between scenarios is exclusively defined by different sets of parameters defined in the job file. The job-generating script uses a set of loops to combine different features to recreate variability in ischemia. A representative job generation script is provided in this annex, used for simulating variability in ischemic scenarios regarding:

a) Subendocardial and transmural ischemia for LAD occlusion.
b) Ectopy triggered in the apical or basal region of the ischemic BZ.
c) Ischemic core zone location and size.
d) Location and size of the two ectopic beats mentioned in b).

These simulation parameters are defined in the code shown below and posteriorly used for generating several ischemia scenarios. In this case, the script generates two ischemia scenarios, each of them with two ectopic stimulus locations at varying coupling intervals. For each of the ischemia scenarios, a basic initial job is created for simulating three sinus rhythm beats to stabilise the model, and to generate a checkpoint then. Later, this checkpoint can be loaded for several dozens of simulation jobs, used to calculate the vulnerability window. In each of those simulations, an ectopic stimulus would be set at varying coupling intervals and locations. Afterwards, it would be possible to analyse which cases led to reentry and the underlying mechanism.

JobGenerator.py

```
#!/usr/bin/python

# Launch script: python JobGenerator.py
# Launch a job: qsub test.job
import os

ISCHEMIA =      ['LADs', 'LADt'];          #a)
S2_MODE =       ['NORTH', 'SOUTH'];        #b)

ICZ_XYZ =       [7.4, 6.1, 4.0];     #LAD  #c)
ICZ_RAD =       [3.0];                #cm  #c)
S2_XYZ =        [[8.0, 3.1, 6.0],[5.2, 4.8, 1.7]];          #d)
S2_RAD =        [1.0];                                      #d)

INDEX = 0;

for i in range(0, len(ISCHEMIA)):
    for j in range(0, len(S2_MODE)):

            directory = 'test_' + ISCHEMIA[i] + '_' + S2_MODE[j];

            if not os.path.exists(directory):
                os.makedirs(directory)

            # Generating jobs with sinus rhythm stimuli
            f = open(directory + '/base' + str(INDEX) + '.job', 'w')
            f.write('#!/bin/bash --login\n')
            f.write('#!# Parallel script produced by bolt\n')
            f.write('# Resource: ARCHER (Cray XC30 (24-core per node))\n')
            f.write('# Batch system: PBSPro_select\n')
            f.write('\n')
            f.write('# bolt is written by EPCC (http://www.epcc.ed.ac.uk)\n')
            f.write('\n')
            f.write('#PBS -l select=30\n')
            f.write('#PBS -A e462\n')
            f.write('#PBS -l walltime=12:0:0\n')
            f.write('#PBS -M hector.martinez-navarro@cs.ox.ac.uk\n')
            f.write('#PBS -m abe\n')
            f.write('\n')
            f.write('# Join output and error files\n')
            f.write('#PBS -j oe\n')
            f.write('\n')
            f.write('#PBS -N base' + str(INDEX) + '\n'    )
            f.write('\n')
            f.write('# Switch to current working directory\n')
            f.write('cd $PBS_O_WORKDIR\n')
            f.write('export OMP_NUM_THREADS=1\n')
            f.write('\n')
            f.write('# Set Chaste output folder\n')
            f.write('export CHASTE_TEST_OUTPUT=\"../' + directory + '\"\n')
            f.write('\n')
            f.write('# Run the parallel program\n')
            f.write('\n')


            f.write(    'aprun -N 24 -n 720 ../TestGenericRunner    -save    -
name base' + str(INDEX) + '    -ischaemia    -purkinjeV 0.140'
                        + '    -radius ' + str(ICZ_RAD[0]) + '    -x ' +
str(ICZ_XYZ[0]) + '    -y ' + str(ICZ_XYZ[1]) + "    -z " + str(ICZ_XYZ[2]) +
'    -transmural ' + str(i)
                        + '    -k0 9.5    -ikatp 0.07    -ina 0.75    -domain
torso    -equation bidomain    -integration adaptative    -cellmodel
OHaraRudy2011_fkatp    -mesh nejib_20131010    '
```

```
                        + '    -odet 0.02    -pdet 0.02    -preconditioner
blockdiagonal    -simduration 1900    -period 600        -cellcomposition1 30
-cellcomposition2 25    -cellcomposition3 45    -reducedPropagation')

            f.close();

            # Generating jobs with ectopy (S1S2 = {120,270}) to be run from
the checkpoint saved after sinus rhythm stimuli
            for t in range(120, 270, 5):
                f = open(directory + '/vw' + str(INDEX) + '_t' + str(t) +
'.job', 'w')
                f.write('#!/bin/bash --login\n')
                f.write('#!# Parallel script produced by bolt\n')
                f.write('# Resource: ARCHER (Cray XC30 (24-core per node))\n')
                f.write('# Batch system: PBSPro_select\n')
                f.write('\n')
                f.write('# bolt is written by EPCC
(http://www.epcc.ed.ac.uk)\n')
                f.write('\n')
                f.write('#PBS -l select=30\n')
                f.write('#PBS -A e462\n')
                f.write('#PBS -l walltime=10:30:0\n')
                f.write('#PBS -M hector.martinez-navarro@cs.ox.ac.uk\n')
                f.write('#PBS -m abe\n')
                f.write('\n')
                f.write('# Join output and error files\n')
                f.write('#PBS -j oe\n')
                f.write('\n')
                f.write('#PBS -N vw' + str(INDEX) + '_t' + str(t) + '\n'    )
                f.write('\n')
                f.write('# Switch to current working directory\n')
                f.write('cd $PBS_O_WORKDIR\n')
                f.write('export OMP_NUM_THREADS=1\n')
                f.write('\n')
                f.write('# Set Chaste output folder\n')
                f.write('export CHASTE_TEST_OUTPUT=\"../' + directory +
'\"\n')
                f.write('\n')
                f.write('# Run the parallel program\n')
                f.write('\n')


                f.write(    'aprun -N 24 -n 720 ../TestGenericRunner    -load
base' + str(INDEX) +    '    -name vw' + str(INDEX) + '_t' + str(t) + '    -
ischaemia    -purkinjeV 0.140'
                            + '    -radius ' + str(ICZ_RAD[0]) + '    -x ' +
str(ICZ_XYZ[0]) + '    -y ' + str(ICZ_XYZ[1]) + "    -z " + str(ICZ_XYZ[2]) +
'    -transmural ' + str(i)
                            + '    -ectopicS2 ' + str(t) + '    -s2radius ' +
str(S2_RAD[0]) + '    -s2x ' +  str(S2_XYZ[j][0]) + '    -s2y ' +
str(S2_XYZ[j][1]) + '    -s2z ' + str(S2_XYZ[j][2])
                            + '    -k0 9.5    -ikatp 0.07    -ina 0.75    -
domain torso    -equation bidomain    -integration adaptative    -cellmodel
OHaraRudy2011_fkatp    -mesh nejib_20131010    '
                            + '    -odet 0.02    -pdet 0.02    -preconditioner
blockdiagonal    -simduration 900    -cellcomposition1 30    -cellcomposition2
25    -cellcomposition3 45')

                f.close();

            INDEX = INDEX + 1;
```

9.3 Post-processing of simulation results

Each of the simulations produces around 70GB of high-resolution data as results. Mainly, the data contain the electrical potential in the ventricular and torso mesh along with the time series defined in the simulation. Files are written in parallel VTK format, making simpler their data management. However, data transfer is limited by the enormous volume of data and the use of supercomputing facilities. An efficient post-processing strategy would benefit from conducting data visualisation remotely to minimise data transfer and data post-processing in local machines.

Data post-processing was based on the next strategies:

- Inducibility for reentry is evaluated from the simulations by rendering one frame every 5-10 ms from 4 different cameras. For this, Paraview scripts are run as a batch to process the conducted simulations. For evaluating the simulated electrical activity in the myocardium, rendered frames are downloaded and compressed into video files.
- In case the visualised simulation is representative, distinct or requires further analysis, a Paraview script was used to extract selected frames to visualise and post-process data locally using Paraview's graphic interface. The execution of this script requires less than 5 minutes.
- A large set of results was stored in external hard drives. In some cases, as the raw data obtained from the simulations. In other cases, as a subset of frames containing the most relevant features for posterior post-processing and analysis.

FrameExtractor.py

```
# Launch script: pvbatch FrameExtractor.py -path IschemiaLAD -s2 250
from paraview.simple import *
import os
import argparse
import vtk
import shutil

# Parsing arguments: simulation name and coupling interval
parser = argparse.ArgumentParser()
parser.add_argument('-path', help='write the simulation results folder')
parser.add_argument('-s2', help='write the simulation results folder')


args = parser.parse_args()
paraview.simple._DisableFirstRenderCameraReset()
addon = "_" + args.s2

# Frames to extract
frame =
[int(args.s2)+2,250,300,350,400,425,450,470,500,520,540,580,640,700,760,820,88
0]

user=args.user;
extra = '';

# Read file
results_pvtu = XMLPartitionedUnstructuredGridReader(
FileName=['/gpfs/scratch/pr1efz00/pr1efz11/marenostrum/' + args.path + '/OUT'
+ addon +  '/vtk_output/results' + addon + '.pvtu'] )

# Load selected frames
results_pvtu.PointArrayStatus = ['V_000000', 'V_000'+str(frame[0]),
'V_000'+str(frame[1]),'V_000'+str(frame[2]),'V_000'+str(frame[3]),'V_000'+str(
frame[4]), 'V_000'+str(frame[5]),
'V_000'+str(frame[6]),'V_000'+str(frame[7]),'V_000'+str(frame[8]),'V_000'+str(
frame[9]), 'V_000'+str(frame[10]),
'V_000'+str(frame[11]),'V_000'+str(frame[12]),
'V_000'+str(frame[13]),'V_000'+str(frame[14])]

# Extracting only the myocardium, not the torso (only elements with higher
potential than 2mV during depolarization
Threshold1 = Threshold()
Threshold1.Scalars = ['POINTS', results_pvtu.PointArrayStatus[0]]
Threshold1.ThresholdRange = [2, 50] # Just get rid of V=0 bath nodes

DataRepresentation = Show()
DataRepresentation.SelectionPointFieldDataArrayName =
results_pvtu.PointArrayStatus[0]
DataRepresentation.ColorArrayName = ('POINT_DATA',
results_pvtu.PointArrayStatus[0])

proxy = GetActiveSource()

# Saving selected frames
out = paraview.simple.XMLPVDWriter(proxy,
FileName='/gpfs/scratch/pr1efz00/pr1efz11/postprocess/' + args.path + addon  +
'_frame.pvd')
out.UpdatePipeline()
```

FrameRenderer.py

```
# Launch script: pvbatch FrameExtractor.py -path IschemiaLAD -s2 250 -user XX
from paraview.simple import *
import os
import argparse
```

```
import shutil

# Parsing arguments: selecting simulation, coupling interval (and user
account)
parser = argparse.ArgumentParser()
parser.add_argument('-path', help='write the simulation results folder')
parser.add_argument('-user', help='write the simulation results folder')
parser.add_argument('-s2', help='write the simulation results folder')

args = parser.parse_args()

paraview.simple._DisableFirstRenderCameraReset()

# Rendering one frame every five
step = 5;
frames = 900;
adding = 3100;

user=args.user;

addon = "_" + args.s2

# Reading maximum and minimum values of X, Y and Z in the myocardium to locate
the image centre
inputfile = open('/work/e462/e462/' + user +
'/Chaste/projects/meshdata/nejib_20131010/extremes.dat')

for line in inputfile:
        elements = line.split('\t')
        minX = float(elements[0])
        maxX = float(elements[1])
        minY = float(elements[2])
        maxY = float(elements[3])
        minZ = float(elements[4])
        maxZ = float(elements[5])

i = 0

# Create new folder or substitute existing one
if  os.path.exists('/work/e462/e462/' + user + '/Postprocessing/' + args.path
+ addon + '/'):
        shutil.rmtree('/work/e462/e462/' + user + '/Postprocessing/' +
args.path + addon + '/')

os.makedirs('/work/e462/e462/' + user + '/Postprocessing/' + args.path + addon
+'/')

# Rendering loop
while i < frames+1:

        results_pvtu = XMLPartitionedUnstructuredGridReader(
FileName=['/work/e462/e462/' + user + '/' + args.path + '/OUT' + addon +
'/vtk_output/results' + addon + '.pvtu'] )

        # Load 1 frame
        if i < 10:
         results_pvtu.PointArrayStatus = ['V_00000' + str(i), 'V_000000']
        elif i < 100:
         results_pvtu.PointArrayStatus = ['V_0000' + str(i), 'V_000000']
        elif i < 1000:
         results_pvtu.PointArrayStatus = ['V_000' + str(i), 'V_000000']
        elif i < 10000:
         results_pvtu.PointArrayStatus = ['V_00' + str(i), 'V_000000']

        results_pvtu.CellArrayStatus = []
```

```
        # Initial camera parameters
        RenderView1 = GetRenderView()
        RenderView1.CenterOfRotation = [(minX+maxX)/2.0, (minY+maxY)/2.0,
(minZ+maxZ)/2.0]
        RenderView1.Background = [1.0,1.0,1.0]
        RenderView1.ViewSize = [1280, 720]

        RenderView1.CenterAxesVisibility = 0
        RenderView1.CameraViewUp = [0.0, 0.0, 1.0]
        RenderView1.CameraPosition = [(minX+maxX)/2.0 - 24, (minY+maxY)/2.0,
(minZ+maxZ)/2.0]
        RenderView1.CameraFocalPoint = [(minX+maxX)/2.0, (minY+maxY)/2.0,
(minZ+maxZ)/2.0]
        RenderView1.CameraParallelScale = 1

        DataRepresentation1 = Show()
        DataRepresentation1.ScaleFactor = 6.0
        DataRepresentation1.ScalarOpacityUnitDistance = 0.3
        DataRepresentation1.SelectionPointFieldDataArrayName =
results_pvtu.PointArrayStatus[0]
        DataRepresentation1.EdgeColor = [0.0, 0.0, 0.5]

        # Look-up table for visualization
        a1_V_000000_PVLookupTable = GetLookupTableForArray(
results_pvtu.PointArrayStatus[0], 1, RGBPoints=[-90, 0.0, 0.0, 1.0, 40.0, 1.0,
0.0, 0.0], NanColor=[0.0, 0.0, 0.0], NumberOfTableValues=446,
ColorSpace='HSV', ScalarRangeInitialized=1.0, AllowDuplicateScalars=1 )
        a1_V_000000_PiecewiseFunction = CreatePiecewiseFunction( Points=[2.0,
0.0, 0.5, 0.0, 80.0, 1.0, 0.5, 0.0, 0.0, 0.0, 0.5, 0.0, 1.0, 1.0, 0.5, 0.0] )

        ScalarBarWidgetRepresentation1 = CreateScalarBar( Title='t =  '+
str(int(i+adding)) + 'ms', Enabled=1, LabelFontSize=9, LabelColor=[0.0, 0.0,
0.0], LookupTable=a1_V_000000_PVLookupTable, TitleFontSize=9, TitleColor=[0.0,
0.0, 0.0], Position=[0.05, 0.5] )
        GetRenderView().Representations.append(ScalarBarWidgetRepresentation1)

        DataRepresentation1.ScalarOpacityFunction =
a1_V_000000_PiecewiseFunction
        DataRepresentation1.ColorArrayName = ('POINT_DATA',
results_pvtu.PointArrayStatus[0])
        DataRepresentation1.LookupTable = a1_V_000000_PVLookupTable

        a1_V_000000_PVLookupTable.ScalarOpacityFunction =
a1_V_000000_PiecewiseFunction

        # Selecting only the myocardial mesh for rendering
        Threshold1 = Threshold()
        Threshold1.Scalars = ['POINTS', results_pvtu.PointArrayStatus[1]]
        Threshold1.ThresholdRange = [3, 100] # Just get rid of V=0 bath nodes

        DataRepresentation2 = Show()
        DataRepresentation2.EdgeColor = [0.0, 0.0, 0.5]
        DataRepresentation2.SelectionPointFieldDataArrayName =
results_pvtu.PointArrayStatus[0]
        DataRepresentation2.ScalarOpacityFunction =
a1_V_000000_PiecewiseFunction
        DataRepresentation2.ColorArrayName = ('POINT_DATA',
results_pvtu.PointArrayStatus[0])
        DataRepresentation2.ScalarOpacityUnitDistance = 0.07
        DataRepresentation2.LookupTable = a1_V_000000_PVLookupTable
        DataRepresentation2.ScaleFactor = 1.1621110000000001

        DataRepresentation1.Opacity = 0.05
        DataRepresentation1.Visibility = 0
```

```
        Delete(DataRepresentation1)

        # Adding zeroes to keep the same character length for names of
rendered images
        if (i+adding < 10):
         extra = "0000"

        elif (i+adding < 100):
         extra = "000"

        elif (i+adding < 1000):
         extra = "00"

        elif (i+adding < 10000):
         extra = "0"

        else:
         extra = ""

        # Best camera setups for LCX occlusion plus rendering
        ##LCX
        RenderView1.CameraViewUp = [0.0, 0.0, 1.0]
        RenderView1.CameraPosition = [(minX+maxX)/2.0, (minY+maxY)/2.0 + 20,
(minZ+maxZ)/2.0 + 6]
        WriteImage('/work/e462/e462/' + user + '/Postprocessing/' + args.path
+ addon + '/videoL' + extra + str(int(i+adding)) + '.png')

        RenderView1.CameraViewUp = [0.0, -1.0, 0.0]
        RenderView1.CameraPosition = [(minX+maxX)/2.0, (minY+maxY)/2.0,
(minZ+maxZ)/2.0 + 26]
        WriteImage('/work/e462/e462/' + user + '/Postprocessing/' + args.path
+ addon + '/videoX' + extra + str(int(i+adding)) + '.png')

        # Best camera setups for LAD occlusion plus rendering
        ##LAD
        RenderView1.CameraViewUp = [0.0, 0.0, 1.0]
        RenderView1.CameraPosition = [(minX+maxX)/2.0 + 20, (minY+maxY)/2.0,
(minZ+maxZ)/2.0 + 6]
        WriteImage('/work/e462/e462/' + user + '/Postprocessing/' + args.path
+ addon + '/videoF' + extra + str(int(i+adding)) + '.png')

        RenderView1.CameraViewUp = [-1.0, 0.0, 0.0]
        RenderView1.CameraPosition = [(minX+maxX)/2.0, (minY+maxY)/2.0,
(minZ+maxZ)/2.0 + 26]
        WriteImage('/work/e462/e462/' + user + '/Postprocessing/' + args.path
+ addon + '/videoU' + extra + str(int(i+adding)) + '.png')

        i = i+step

        # Deleting data to prevent memory leak
        Delete(ScalarBarWidgetRepresentation1)
        Delete(DataRepresentation2)
        Delete(results_pvtu)
        Delete(Threshold1)
        Delete(RenderView1)
```

9.4 Electrocardiogram simulation

Electrocardiographic signal was simulated using the extracellular potential measured at mesh nodes located in the typical 12-lead ECG electrode positions. Afterwards, ECG is computed in Matlab as follows:

```
% Limb leads
I=LA-RA;
II=LL-RA;
III=LL-LA;
% Wilson's central terminal
Vw=1/3*(RA+LA+LL);
% Augmented leads
aVR=3/2*(RA-Vw);
aVL=3/2*(LA-Vw);
aVF=3/2*(LL-Vw);
% Precordial leads
V1=V1-Vw;
V2=V2b-Vw;
V3=V3a-Vw;
V4=V4-Vw;
V5=V5-Vw;
V6=V6-Vw;
%%%%%%%%%%
```